PARTIALLY CORRELATED PERSISTENT SCATTERER THEORY AND TECHNIQUES FOR RADAR INTERFEROMETRY

A DISSERTATION
SUBMITTED TO THE DEPARTMENT OF ELECTRICAL ENGINEERING
AND THE COMMITTEE ON GRADUATE STUDIES
OF STANFORD UNIVERSITY
IN PARTIAL FULFILLMENT OF THE REQUIREMENTS
FOR THE DEGREE OF
DOCTOR OF PHILOSOPHY

Jaime Lien
November 2016

I certify that I have read this dissertation and that, in my opinion, it is fully adequate in scope and quality as a dissertation for the degree of Doctor of Philosophy.

(Howard Zebker) Principal Adviser

I certify that I have read this dissertation and that, in my opinion, it is fully adequate in scope and quality as a dissertation for the degree of Doctor of Philosophy.

(Paul Segall)

I certify that I have read this dissertation and that, in my opinion, it is fully adequate in scope and quality as a dissertation for the degree of Doctor of Philosophy.

(Andrea Montanari)

Approved for the Stanford University Committee on Graduate Studies

Abstract

Interferometric synthetic aperture radar (InSAR) is an effective technology for measuring temporal changes of the Earth's surface. By combining SAR echoes collected at varying times and orbit geometries, we can produce wide coverage images of crustal deformation fields with centimeter-level accuracy. However, conventional InSAR techniques often fail to recover a coherent deformation signal when the radar imaging geometry or surface scattering properties change significantly between radar passes. This phenomenon, known as decorrelation, produces a random phase term that obscures the deformation signal and reduces the amount of InSAR data suitable for time series analysis.

We can overcome these limitations by exploiting a subset of intrinsically phase-stable pixels, the so-called persistent scatterers (PS). Identifying such pixels is a crucial component of this analysis, since phase unwrapping and subsequent deformation estimation on the spatially sparse PS network depends on both pixel selection accuracy and the network density. PS techniques have been shown to work well in urban areas with many strong, stable reflectors, but identifying an appropriate network of pixels in natural or vegetated terrain remains a challenge due to other spatiotemporally varying phase terms.

In this dissertation, we present new theory and techniques for generalized PS analysis based on partially correlated persistent scatterers (PCPS): those that are non-ideal but stable enough for deformation time series measurement in largely decorrelated areas. We develop a new physically-based method for modeling spatiotemporal decorrelation, as well as a comprehensive statistical characterization of the resulting interferometric pixels. We show that these analytical results lay a theoretical foundation for PCPS algorithm development. Next, we introduce a more reliable PS selection technique that combines the full set of interferometric observations as a function of their acquisition intervals. The PCPS technique achieves a better trade-off between pixel selection accuracy and network density compared to other PS identification methods. Finally, we present examples of deformation measurements obtained using PCPS analysis. These results demonstrate that through improved statistical characterization, the PCPS technique attains reliable deformation measurements for a variety of wavelengths, terrain, and geophysical processes.

Acknowledgements

This thesis would not have been possible without the support of several colleagues, friends, and family.

First and foremost, I wish to thank my advisor, Professor Howard Zebker, for his mentorship and encouragement throughout my Ph.D. Professor Zebker provided guidance whenever I needed, while also allowing me the independence to follow my interests and shape my own research path. He has been a role model as a teacher, advisor, and technical expert. I hold his advice in the highest regard and deeply appreciate all the support he has given me.

I was extremely fortunate to also have on my thesis committee some of my favorite teachers and preeminent scholars in their fields: Professors Paul Segall, Andrea Montanari, Antony Fraser-Smith, and John Pauly. I am grateful for their thoughtful input on this work. I particularly thank Professor Fraser-Smith for the many times he stopped to chat and encourage me during long hours in the lab.

The Stanford Radar Remote Sensing group have been invaluable colleagues throughout my Ph.D. Albert Chen, Ann Chen, Eileen Lin, Will Woods, Cody Wortham, Clara Yoon, Lin Liu, Jessica Reeves, Lauren Wye, Piyush Shanker Agram, and Sang-Ho Yun all provided a great deal of assistance and insight that shaped my own work, as well as moral support and encouragement.

Several members of the Stanford Electrical Engineering department played a huge role in making my Ph.D. a memorable and fulfilling experience. In particular, Michael Marx, Georges Goetz, John Mu, Frank Chen, Derek Pang, Chinyere Nwabugwu, and the executive team of GSEE have been great friends and an invaluable support system during my time at Stanford.

I am grateful to the Touchstone team at Google ATAP for the inspiration and motivation they provided as I finished my thesis. I especially wish to thank Ivan Poupyrev, Roberto Aiello, Emre Karagozler, and Patrick Amihood for their empathy, encouragement, and colorful humor.

I am forever grateful to my parents, sister, and brother for supporting and encouraging me throughout my academic career.

Finally, I owe my deepest thanks to Chris for his unwavering partnership in every step of this journey.

This work was generously funded by the National Defense Science and Engineering Graduate (NDSEG) Fellowship, the William Terman Stanford Graduate Fellowship (SGF), and research grants from NASA.

Contents

List of Tables

List of Figures

Acronyms

ALOS Advanced Land Observing Satellite

COSMO-SkyMed Constellation of Small Satellites for Mediterranean basin Observation-SkyMed

DEM Digital elevation map

ERS European Remote Sensing

InSAR Interferometric synthetic aperture radar

JAXA Japan Aerospace Exploration Agency

ML Maximum likelihood

PALSAR Phased Array L-band Synthetic Aperture Radar

PCPS Partially correlated persistent scatterer

PDF Probability distribution function

PS Persistent scatterer

PS-InSAR Permanent Scatterer InSAR

RF Radio frequency

RMSE Root mean square error

SAR Synthetic aperture radar

SBAS Small baseline subset

SCR Signal-to-clutter ratio

SNR Signal-to-noise ratio

StaMPS Stanford Method for Persistent Scatterers

Nomenclature

$\mathcal{S}$	Set
α	Angle between baseline and normal
$\delta(.,.)$	Dirac delta function (2-dimensional)
δ_r	Range resolution
δ_{az}	Azimuth resolution
λ	Wavelength
$\mathbf{1}_{n\times m}$	Matrix of size $n \times m$ with all entries equal to 1
$\mathbf{\Gamma}$	Generalized covariance matrix
$\mathbf{f}^\dagger$	Complex conjugate of transpose of vector $\mathbf{f}$
$\mathbf{H}^\dagger$	Hermitian transpose of matrix $\mathbf{H}$
$\mathbf{I}_n$	Identify matrix of size $n \times n$
$\mathcal{CN}(\mu, \Sigma)$	Distribution of proper complex Gaussian random vector with mean μ, covariance matrix Σ, and pseudo-variance matrix $\mathbf{0}$
$\mathcal{CN}(\mu, \sigma^2)$	Distribution of proper complex Gaussian random variable with mean μ, variance σ^2, and pseudo-variance 0
$\mathcal{I}\{.\}$	Indicator function
erf(.)	Error function
E[.]	Expectation
SCR	Signal-to-clutter ratio
SNR	Signal-to-noise ratio

ϕ	Phase
ϕ_{atm}	Atmospheric phase term
ϕ_{decorr}	Decorrelation phase term
ϕ_{def}	Deformation phase term
ϕ_{err}	Orbital error phase term
ϕ_{ifg}	Interferometric phase
ϕ_{noise}	Noise phase term
ϕ_{topo}	Topographic phase term
ϕ_i	SAR pixel phase in image i
ϕ_{0i}	Interferometric pixel phase from master image 0 and slave image i
ρ	Path length
ρ_{spatial}	Spatial decorrelation
ρ_{temp}	Temporal decorrelation
σ^2	Average total backscatter power
σ_c	Radar cross section of clutter
σ_s	Radar cross section of dominant scatterer
σ_T	Rate of temporal decorrelation decay
σ_y	Root mean square displacement in range
σ_z	Root mean square displacement in height
θ	Incidence angle
θ_{az}	Azimuth angular resolution
B	Spatial baseline
B_{crit}	Critical spatial baseline
B_{ij}	Perpendicular baseline between acquisitions i and j
BW	Bandwidth

c	Speed of light
c_i	Clutter component for SAR pixel PS model in image i
$f(x, y)$	Surface backscatter function
$f(x; \mathbf{p})$	Function f of variable x that is parameterized by $\mathbf{p}$
f_D	Doppler frequency
$f_s(x, y)$	Dominant scatterer surface backscatter function
$I_0(.)$	Modified Bessel function
l	Antenna aperture length
m_y	Average rate of movement in range
N	Number of interferograms
N_{ifg}	Number of interferograms
N_{sar}	Number of SAR images
r	Range
r_0	Range at radar's closest approach
r_i	SAR pixel amplitude in image i
R_x	Azimuth resolution
R_y	Ground range resolution
r_{0i}	Interferometric pixel amplitude from master image 0 and slave image i
s	Complex SAR pixel value
s	Signal component for SAR pixel PS model
T_{crit}	Critical temporal baseline
t_d	Time delay
T_{ij}	Temporal baseline between acquisitions i and j
u	Line of sight vector
u_i	SAR pixel value in image i

v	Radar platform velocity
$W(x, y)$	Radar imaging impulse response
x	Azimuth
x^*	Complex conjugate of x
x_{ML}	Maximum likelihood estimate of x
y	Ground range
z	Interferometric pixel value
z_i	Interferometric pixel value in interferogram i

Chapter 1

Introduction

The Earth's surface is constantly changing due to both manmade and natural phenomena. Recent natural disasters have highlighted the need to monitor and understand geophysical processes such as earthquakes, volcanoes, landslides, and ground subsidence. Crustal deformation measurements play a crucial role in these studies. The models, data, and analysis enabled by these measurements are essential in identifying areas prone to natural disasters; optimizing of disaster response policies and resources; and regulating activity for sustainable development.

Spacebourne interferometric synthetic aperture radar (InSAR) is an effective technology for remotely imaging changes in the Earth's surface. Satellite radar is a cost-effective method to obtain large coverage, spatially dense deformation measurements over very long time spans. As an active sensor, radar is not dependent on external lighting conditions, and radar wavelengths easily penetrate clouds and atmosphere. By combining synthetic aperture radar (SAR) phase data collected at varying times and orbit geometries, we can produce wide coverage images of crustal deformation fields with sub-centimeter-level accuracy.

However, conventional InSAR techniques are limited in their ability to recover a coherent deformation signal when the radar imaging geometry or surface scattering properties change significantly between radar passes. This phenomenon, known as decorrelation, produces a random phase term that obscures the deformation signal and reduces the amount of InSAR data suitable for time series analysis. Decorrelation leads to a loss in image spatial coherence and can render large areas of the image unsuitable for deformation measurements.

We can overcome these limitations by exploiting a subset of intrinsically phase-stable pixels, the so-called persistent scatterers (PSs). Identifying such pixels is a crucial component of this analysis, since phase unwrapping and subsequent deformation estimation on the spatially sparse PS network depends on both pixel selection accuracy and the network density. PS techniques have been shown to work well in urban areas with many strong, stable reflectors, but identifying an appropriate network of pixels in natural or vegetated terrain remains a challenge due to other spatiotemporally varying

phase terms.

In this thesis, we discuss new theory and techniques for generalized PS analysis based on partially correlated persistent scatterers (PCPSs): those that are non-ideal but stable enough for deformation time series measurement in largely decorrelated areas. We present a new physically-based method for modeling spatiotemporal decorrelation, as well as a comprehensive statistical characterization of the resulting interferometric pixels. We show that these analytical results lay a theoretical foundation for PCPS algorithm development. Next, we introduce a more reliable PS selection technique that combines the full set of interferometric observations as a function of their acquisition intervals. The PCPS technique achieves a better trade-off between pixel selection accuracy and network density compared to other PS identification methods. Finally, we present examples of deformation measurements obtained using PCPS analysis. These results demonstrate that through improved statistical characterization, the PCPS technique attains reliable deformation measurements for a variety of wavelengths, terrain, and geophysical processes.

1.1 Contributions

There are three main foci of this thesis. First, we develop the theory of partially correlated persistent scatterers, including parameterized scattering models and derived statistical characterizations. Second, we apply this theoretical analysis in order to develop an improved technique to identify and select PS pixels. Finally, we utilize the PCPS selection technique with the Stanford Method for Persistent Scatterers (StaMPS) framework in order to measure crustal deformation from a variety of InSAR data sets.

The main contributions of this thesis are summarized below.

1. We present a new parameterized PCPS statistical scattering model.
2. From the scattering model, we derive a new analytical expression for the spatiotemporal decorrelation of PCPS pixels as a function of their scattering characteristics.
3. We verify the analytical PCPS decorrelation model by comparison to observed C-band InSAR data.
4. We derive the probability distribution function (PDF) for a full interferometric stack of PCPS pixels as a function of the scattering parameters and radar imaging baselines.
5. We explain how the PCPS theoretical foundation leads to practical improvements in PS algorithm development.
6. We design a new PS statistical selection technique that optimally combines the full set of interferometric observations as well as repeat pass spatiotemporal acquisition intervals.

7. We perform a case study to estimate the performance of PCPS identification accuracy versus false detection compared to existing PS techniques.

8. We implement and utilize this selection technique with the StaMPS framework in order to extract deformation measurements for a variety of wavelengths, terrain, and geophysical processes.

9. We compare the PS selection results on real InSAR data for the PCPS technique compared to existing PS methods.

1.2 Thesis roadmap

The remaining chapters of the thesis are organized as follows.

In Chapter 2, we provide a brief overview of radar remote sensing and imaging, InSAR, and prior work on PS techniques.

In Chapter 3, we present a new radar scattering model that relates the PCPS signal moments to physical properties of the surface. From this scattering model, we derive a new analytic model for the spatiotemporal decorrelation of persistent scatterers as a function of baseline and signal-to-clutter ratio (SCR). This model quantifies the partial correlation of persistent scatterer pixels over large baselines, providing a means to characterize and compare the phase stability of PS, non-PS, and ideal point scatterer pixels. Our analysis fundamentally explains why PS coherence remains high over large baselines and justifies the use of interferometric data with baselines equal to or greater than the critical baseline. We support our analytic models with decorrelation measurements from real InSAR data.

In Chapter 4, we present a more complete statistical characterization of the PS decorrelation phase statistics, derived from PS scattering principles. We review previous interferometric phase distributions based on a model of the PS SAR pixel. Next, we use the new PS backscattering model and interferometric stack system model in Chapter 3 to derive the joint phase-amplitude distribution for the entire stack of pixels as a function of SCR and spatial baseline. We discuss the fundamental differences in the PS models and quantitatively compare the resulting analytical distributions in Section 4.5. We show that the new PS backscatter model and resulting distribution fit simulated data better than previous analysis.

In Chapter 5, we present an algorithm for improved PS selection and show results of this algorithm for a variety of radar data sets. We first describe the general StaMPS framework for PS deformation measurement, emphasizing the critical step of PS selection. Next, we present a review of existing PS selection techniques. We then show a new method of PS characterization and selection based on the analytical results of the previous chapters. This method optimally combines the full stack of phase and amplitude observations, as well as information about the spatiotemporal baselines. We

perform a case study to estimate the performance in terms of PS identification and false detection compared other PS methods. Our results based on simulated and real data demonstrate that with an increased amount of information, we obtain better PS parameter estimation and selection. We present a set of example deformation measurements from a variety of real satellite radar data using our PCPS selection method.

Finally, we present a concluding summary and directions for future research in Chapter 6.

Chapter 2

Background

2.1 Radar remote sensing

Radar is a sensing modality based on the reflection and detection of radio frequency (RF) electromagnetic waves. The term *radar* originated as an acronym for "radio detection and ranging," as the technology was initially developed to detect and track moving objects such as airplanes and ships in the 1930s and 1940s [Brown, 1999]. Radar is now used for a much broader range of applications, including high resolution imaging [Ausherman et al., 1984, Odendaal et al., 1994], target characterization [Kim et al., 2002, Smith and Goggans, 1993], activity recognition [Kim and Ling, 2009, Liu et al., 2011], gesture sensing [Lien et al., 2016], ground penetration [Daniels, 2004, Jol, 2008], health monitoring [Li et al., 2009, Droitcour et al., 2001], and geophysical monitoring [Elachi et al., 1990, Massonnet and Feigl, 1995].

Satellite radar has been used for remote sensing and imaging of the Earth since the launch of SEASAT in 1978 [Bamler and Hartl, 1998]. Radar has several advantages as an instrument for remote Earth monitoring. Satellite radar enables large coverage, spatially dense observations that are not feasible with in situ measurements. Unlike optical sensors, radars are actively powered and hence not limited to daytime operation. Because atmosopheric attenuation is low at radio frequencies, radar can penetrate atmosphere, clouds, and precipitation that cameras cannot see through. Radar also enables high resolution three-dimensional mappings of terrain.

Satellite radars are typically pulsed, coherent, and operate in the range of 10^6 to 10^{12} Hz, making them sensitive to objects on the order of centimeters to meters in size. A basic satellite radar system, shown in Figure 2.1 consists of a transmitter and receiver, antenna, oscillator, modulator, and circulator. Remote sensing radar satellites generally operate in near geosynchronous orbit, at altitudes ranging from 600-800 kilometers. As the satellite moves along the orbit path, a side-looking radar antenna illuminates an area of the Earth's surface called a *footprint* or *radar swath*. The direction along the orbit path is referred to as *azimuth* or *along-track*, while the perpendicular

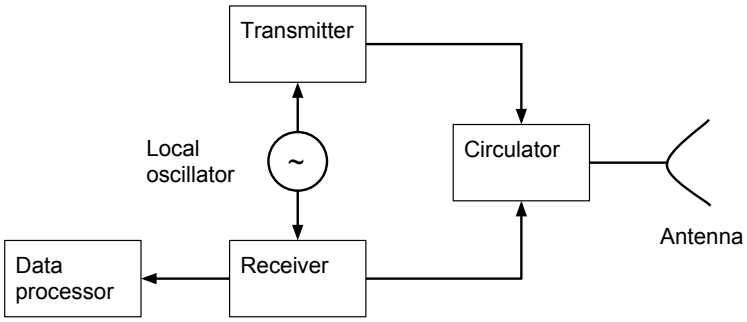

Figure 2.1: Basic radar components

direction is called *range* or *across-track*.

2.2 Radar imaging

One of the primary advantages of radar as a remote sensing modality is its ability to produce spatially dense measurements of the Earth's surface. Because radar can simultaneously measure the reflectivity as well as spatial location of scatterers, the measurements can be registered to spatial coordinates in order to produce a radar image. Two figures of merit for a radar imaging system are its signal-to-noise ratio (SNR) and resolution, the ability of the system to distinguish two point targets.

The total received radar signal from a transmitted pulse is the coherent sum of time-delayed reflections from scatterers within the illuminated ground swath. The pulse reflections are amplitude-modulated by the scattering properties of the swath. The reflected energy from each discrete scatterer back in the direction of the radar is a factor of many properties, including its physical size, shape, surface smoothness, and material. Signal processing techniques are used to spatially resolve scatterers and improve SNR.

In the range dimension, the distance r from the radar to a scatterer is determined by the two-way time delay t_d between the pulse transmission and reception of the echo:

$$r = \frac{ct_d}{2} \tag{2.1}$$

where c is the speed of light.

Range resolution is produced using pulse compression, in which the received signal is processed through a matched filter. By correlating the received signal with the transmitted signal, the reflected energy is compressed into an effectively shorter pulse, increasing the resolution and SNR. Using this

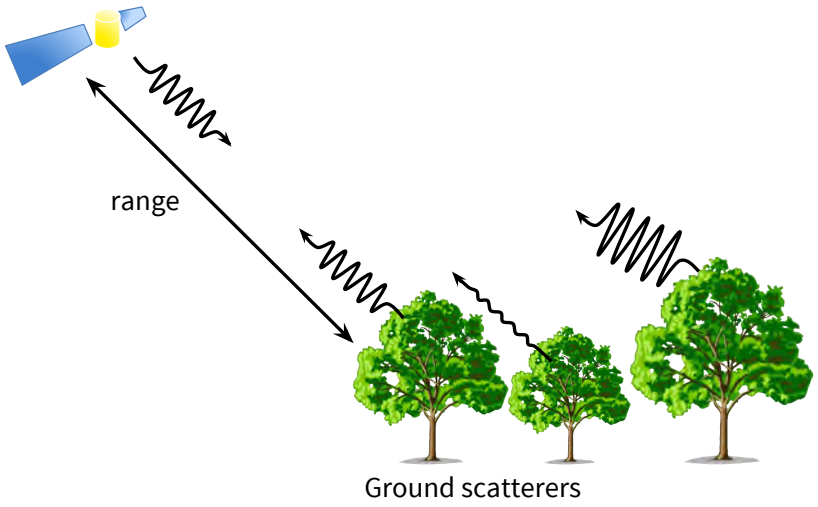

Figure 2.2: Range resolution refers to the ability to distinguish scatterers that are spatially close to each other.

technique, the range resolution δ_r is limited by the bandwidth BW of the transmitted signal:

$$\delta_r = \frac{c}{2BW} \tag{2.2}$$

Bandwidth is generated through pulse modulation schemes such as frequency modulation or phase shift keying, enabling resolutions finer than those determined by the transmission pulse length alone.

The azimuth angular resolution θ_{az} of a real aperture radar system is determined by the antenna's angular beamwidth, which is proportional to the wavelength λ and inversely proportional to the physical aperture dimension l:

$$\theta_{az} = \frac{\lambda}{l}$$

At a range of r, this resolution produces a ground swath of azimuth length

$$\delta_{az} = \frac{\lambda r}{l \cos\theta}$$

where θ is the incidence angle of the transmitted wave.

To achieve fine resolution on the order of meters, a real aperture antenna would need to be on the order of kilometers long. Obviously the size and mass involved is prohibitive for space applications. By using a signal processing concept called SAR, we can instead exploit the relative motion between the ground and the radar in order to synthesize the equivalent of very large antenna aperture using a relatively small physical antenna.

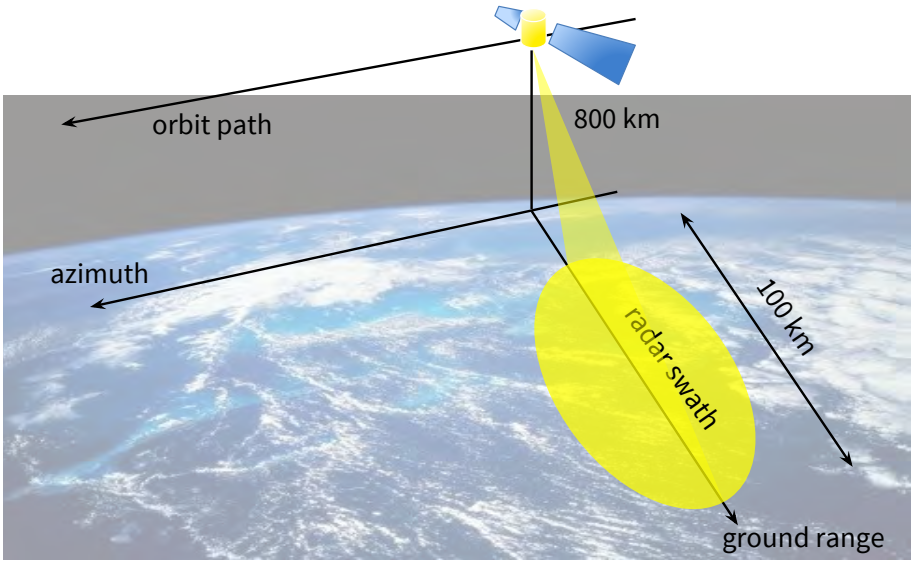

Figure 2.3: Satellite radar geometry, real aperture antenna

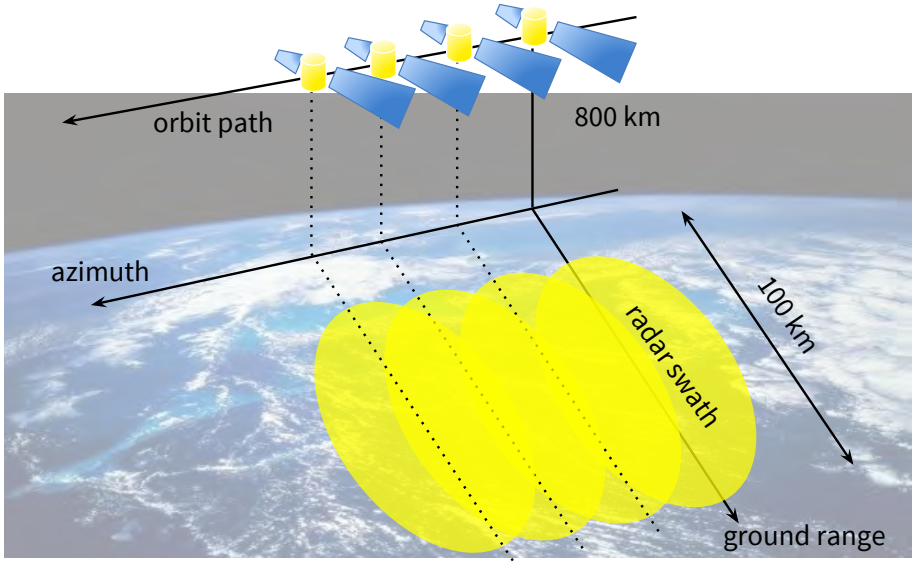

Figure 2.4: Satellite radar geometry, synthetic aperture antenna

2.3 Synthetic aperture radar

SAR is a signal processing technique for producing high resolution radar images. The relative motion between the radar and the ground is used to synthesize a larger aperture and hence narrower beamwidth than the physical dimensions of the antenna afford. As the radar travels along the orbit path, successive transmitted pulses illuminate a ground swath from different antenna positions. The reflected radar echoes are pulse compressed for range resolution and then processed in order to form a two-dimensional image.

SAR exploits the Doppler phenomenon in order to resolve scatterers in the azimuth direction. The phase of the received radar echo from a point scatterer at range $r(t)$ is given by

$$\phi(t) = -\frac{4\pi}{\lambda} r(t) = -\frac{4\pi}{\lambda}\sqrt{r_0^2 + v^2 t^2} \tag{2.3}$$

where r_0 is the range to the scatterer at the radar's closest approach and v is the radar platform's velocity. As the satellite travels, the range to a fixed scatterer, and hence the phase of its reflection, also varies. The time-varying phase produces a Doppler frequency

$$f_D = \frac{d\phi}{dt} = \frac{2v \cdot u}{\lambda} \tag{2.4}$$

where $v \cdot u$ represents the projection of the radar platform's velocity onto the line of sight vector from the radar to the scatterer.

By correlating the range-compressed radar data with the phase history of a point scatterer, the response from a ground scatterer can be coherently integrated over multiple pulses. This matched filter improves the azimuth resolution to

$$\delta_{az} = \frac{l}{2}. \tag{2.5}$$

Equation 2.5 shows that with SAR, the azimuth resolution is no longer limited by the size of the antenna. In fact, the resolution improves as the antenna size decreases. Intuitively, this is because a smaller aperture causes a larger radar ground swath, which in turns means that each ground resolution element is in the ground swath for more radar pulses as the radar passes overhead. This enables the matched filter to compress a greater amount of collected energy into a smaller azimuth location.

The complex value of each SAR pixel is determined by the coherent sum of reflections from multiple scatterers within the corresponding ground resolution element, convolved with the radar imaging impulse response. These reflections add constructively and destructively, producing a speckle effect on the pixel amplitude [Lee, 1981]. The absolute phase of a single SAR pixel is essentially random and generally not useful.

2.4 Interferometric SAR

2.4.1 Technique

Interferometric synthetic aperture radar (InSAR) is a signal processing technique to extract the difference in phase between multiple SAR acquisitions. SAR images acquired from different imaging geometries are first coregistered and resampled so that pixels map to the same ground resolution elements. An interferogram is then produced by multiplying one complex SAR image, the master, by the complex conjugate of a second SAR image, the slave. The phase of the resulting image equals the difference in phase between two SAR images and is related to the difference in the path length $\Delta\rho$ in the radar line-of-sight (LOS) between the acquisitions:

$$\Delta\phi = -\frac{4\pi}{\lambda}\Delta\rho. \tag{2.6}$$

If the SAR images are acquired from different orbital positions and no deformation occurs between the passes (for example, if the images are acquired simultaneously from displaced antennae), then the path length difference $\Delta\rho$ is a function of the orbital and Earth geometry [Rodriguez and Martin, 1992], producing a topographic phase term

$$\phi_{topo} = \frac{4\pi}{\lambda}\Delta\rho = \frac{4\pi}{\lambda}B\cos(\theta+\alpha) \tag{2.7}$$

where B is the physical baseline separation between the antennae, α is the angle between the baseline and the local normal, and θ is the look angle. InSAR can thus be used to produce high resolution topographic maps of the Earth's terrain [Zebker and Goldstein, 1986].

If ground topography is known, either from another interferogram or a digital elevation model (DEM), then repeat pass InSAR can be used to image spatiotemporal deformation fields of the Earth's surface [Gabriel et al., 1989]. This technique, sometimes known as Differential InSAR (D-InSAR), was first applied to measure crustal deformation associated with the 1992 Landers earthquake [Massonnet et al., 1993, Zebker and Rosen, 1994]. The interferometric phase contribution due to ground deformation Δr in the radar's line-of-sight between acquisitions is

$$\Delta\phi_{def} = -\frac{4\pi}{\lambda}\Delta r. \tag{2.8}$$

An example interferogram produced from European Remote Sensing (ERS) C-band radar data is shown in Figure 2.6. The fringes in the interferogram show deformation contour lines resulting from the Hector Mine earthquake. Each fringe cycle corresponds to LOS displacement of $\frac{\lambda}{2}$.

Because phase is measured modulo 2π, interferometric phase has an inherent ambiguity; a phase

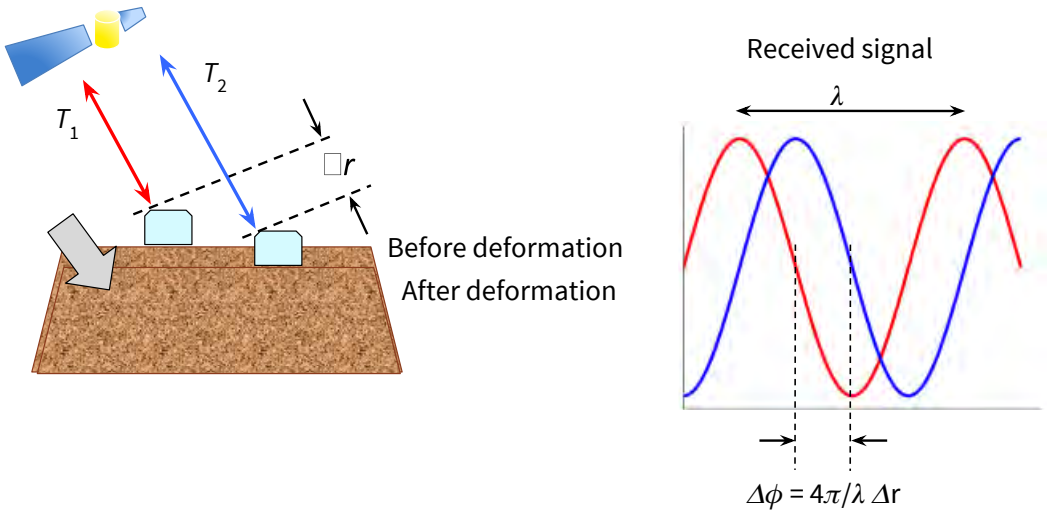

Figure 2.5: The change in phase between two SAR acquisitions is related to amount of ground deformation in the radar line-of-sight.

value of ϕ is indistinguishable from phases of $\phi \pm 2n\pi$ for all integer values of n. This results in phase discontinuities in the image. These ambiguities and discontinuities are resolved by a process known as phase unwrapping, in which the differential phases between adjacent pixels are integrated over the interferogram [Zebker and Lu, 1998, Costantini, 1998, Chen and Zebker, 2002].

By combining SAR phase data collected at varying times and orbit geometries, we can produce wide coverage images of crustal deformation fields with centimeter-level accuracy. With a coregistered multi-temporal stack of interferograms, deformation times series over periods of days to decades can be extracted. InSAR data is used for a wide variety of geophysical remote sensing applications, including imaging crustal deformation due to earthquakes [Massonnet et al., 1993, Jónsson et al., 2002] and volcanoes [Amelung et al., 2000, Yun et al., 2006]; monitoring landslides [Lauknes et al., 2010, Tarchi et al., 2003]; and measuring ground subsidence [Amelung et al., 1999, Hoffmann et al., 2001].

2.4.2 Interferometric phase terms

Extraction of the deformation signal is complicated by the presence of other interferometric phase terms. We model the the total interferometric phase ϕ_{ifg} as a sum of these terms:

$$\Delta\phi_{\text{ifg}} = \phi_{\text{def}} + \phi_{\text{atm}} + \phi_{\text{err}} + \phi_{\text{decorr}} + \phi_{\text{noise}}. \tag{2.9}$$

The interferometric phase terms are described below and summarized in Table 2.1.

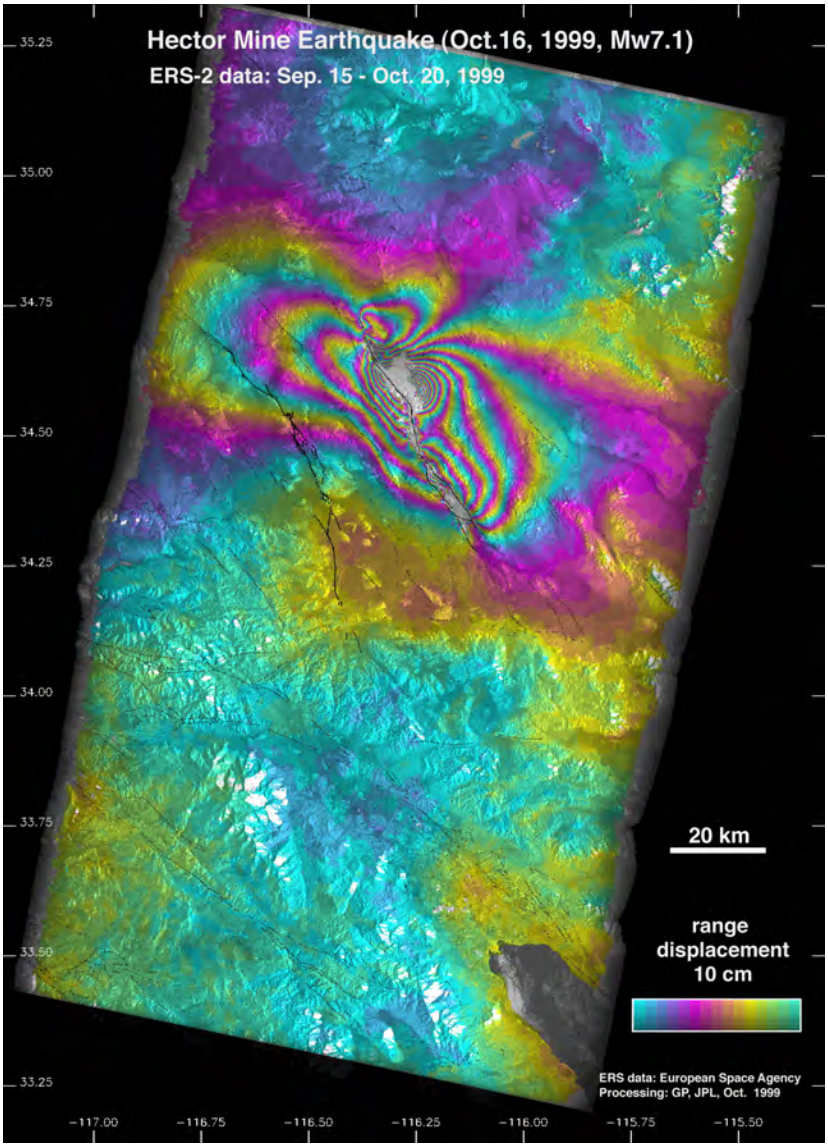

Figure 2.6: 1999 Hector Mine earthquake interferogram (credit: Jet Propulsion Lab)

Phase term		Structure
Deformation (signal of interest)	ϕ_{def}	Spatially, temporally correlated
Atmosphere	ϕ_{atm}	Spatially correlated
Topographic	ϕ_{topo}	Deterministic
Errors in orbital/topographic information	ϕ_{err}	Function of imaging geometry
Noise	ϕ_{noise}	Random
Decorrelation	ϕ_{decorr}	Random

Table 2.1: Interferometric phase terms

Deformation ϕ_{def}

The deformation phase is the signal of interest. This term tends to be both spatially and temporally correlated, although high frequency deformation is often difficult to spatiotemporally model and extract.

Atmospheric phase ϕ_{atm}

The atmospheric phase term arises from variations in signal propagation delay, largely due to differences in tropospheric water vapor content [Massonnet et al., 1994]. Its contribution to the interferometric phase is typically on the order of one-tenth of a wavelength [Tarayre and Massonnet, 1996]. Atmospheric phase tends to be correlated spatially and with topography [Hanssen, 2001], but essentially temporally uncorrelated after a period of about 30 days. Its effects can be compensated using terrain data, existing weather models, or atmospheric data from other sensing modalities [Bonforte et al., 2001, Li et al., 2005].

Orbital error ϕ_{err}

The orbital error phase terms are due to imprecise knowledge of the orbit path or geometry. The orbital error phase terms are spatially correlated and can therefore be compensated or filtered with some knowledge of the orbital geometry [Agram, 2010]. Alternatively, ground control points may be used to constrain the satellite position at known times [Shimada, 2000].

Thermal noise ϕ_{noise}

Thermal noise adds a random phase term that is modeled as white and Gaussian.

Decorrelation ϕ_{decorr}

Decorrelation due to spatial and temporal baseline is a major limiting factor in estimating the crustal deformation signal from interferometric phase data [Zebker and Villasenor, 1992]. Decorrelation arises because the measured radar return for a ground resolution element is the sum of complex echoes from multiple discrete scatterers located within the element [Rosen et al., 2000]. Changes in the radar imaging geometry, scatterer positions, or scattering behavior between radar passes alters the amplitude or path length of reflections from discrete scatterers. The change in constructive and destructive interference of these reflections causes the coherent sum to have a random, noise-like decorrelation phase term that obscures the deformation signal.

Temporal decorrelation occurs when the scattering behavior or scatterer positions changes between radar passes. Vegetation, seasonal changes such as snow coverage or melting, man-made changes, and other phenomenon tend to contribute to temporal decorrelation. The amount of

decorrelation is varies with the temporal separation between radar passes, known as the temporal baseline T_{12}.

Spatial decorrelation results from changes in the radar imaging geometry. A change in the wave incidence angle causes different interference patterns in the coherent sum of reflections from discrete scatterers. Spatial decorrelation increases with the perpendicular baseline B_{12}.

At critical limits on the temporal baseline or spatial baseline, the interferogram suffers from complete loss of coherence, and no useful deformation information can be extracted. Decorrelation leads to a loss in image spatial coherence and prevents the use of large baseline data [K.Li and Goldstein, 1990], decreasing the temporal resolution of the InSAR data.

2.4.3 Multi-temporal InSAR

Multi-temporal InSAR data can be used to mitigate the effect of extraneous phase terms and improve extraction of crustal deformation time series. Two broad categories of multi-temporal techniques are small baseline subset (SBAS) and Persistent Scatterer (PS), the latter of which is the focus of this thesis.

2.5 Persistent scatterer techniques

Conventional InSAR techniques often fail to recover a coherent deformation signal when the radar imaging geometry or surface scattering properties change significantly between radar passes. This phenomenon, known as decorrelation, produces a random phase term that obscures the deformation signal and reduces the amount of InSAR data suitable for time series analysis.

We can overcome these limitations by exploiting a subset of intrinsically phase-stable pixels, the so-called persistent scatterers (PS). PS pixels are those which are dominated by a point-like scatterer and in which the decorrelation phase term is small. Using a network of such pixels, we can filter noise, estimate the remaining phase terms, and accurately recover the deformation signal [Ferretti et al., 2001].

Identifying such pixels is a crucial component of this analysis, since phase unwrapping and subsequent deformation estimation on the spatially sparse PS network depends on both pixel selection accuracy and the network density. PS techniques have been shown to work well in urban areas with many strong, stable reflectors, but identifying an appropriate network of pixels in natural or vegetated terrain remains a challenge due to other spatiotemporally varying phase terms.

2.5.1 Prior work

PS techniques were first proposed as a method called Permanent Scatterer InSAR (PS-InSAR) by Ferretti et al. in 2001 [Ferretti et al., 2001]. This technique utilizes an assumed deformation model

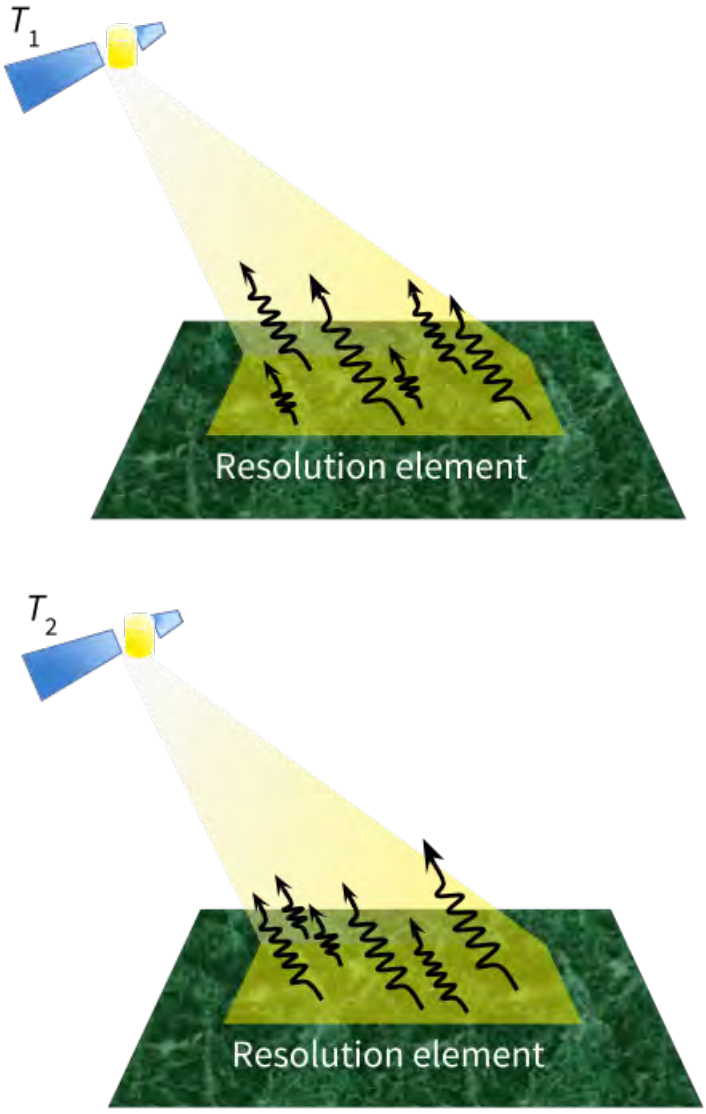

Figure 2.7: Temporal decorrelation occurs when the scattering behavior or scatterer positions changes between radar passes. Vegetated terrain and areas prone to seasonal changes such as snow coverage tend to suffer from decorrelation as function of the temporal baseline $T_{12} = T_2 - T_1$.

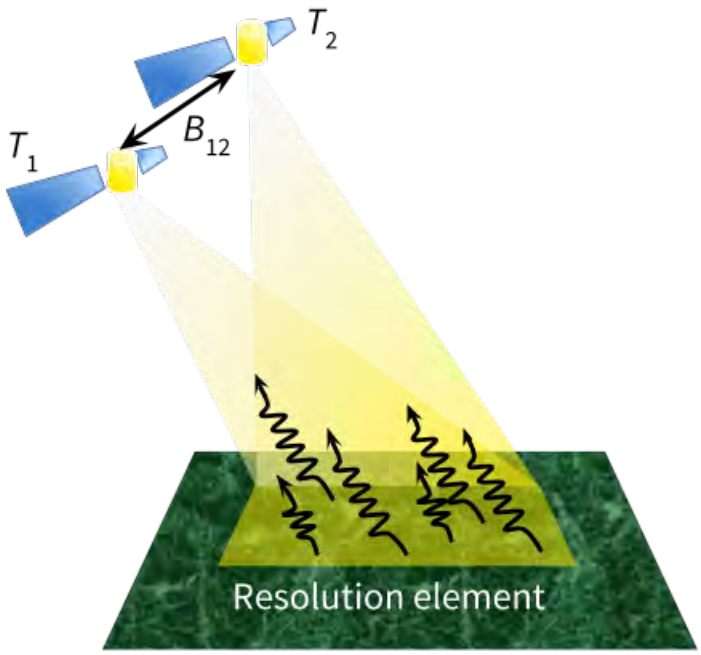

Figure 2.8: Spatial decorrelation results from changes in the radar imaging geometry. A change in the perpendicular baseline B_{12} causes different interference patterns in the coherent sum of reflections from discrete scatterers.

in order to identify PS pixels. Versions of PS-InSAR have been applied to study landslides [Farina et al., 2006, Colesanti et al., 2003b], seasonal ground deformation [Colesanti et al., 2003a], and fault creep [Lyons and Sandwell, 2003], and general geophysical phenomena [Vilardo et al., 2009].

In 2004, Hooper et al. developed and demonstrated the Stanford Method for PS (StaMPS) algorithm that removed the need for prior deformation knowledge [Hooper et al., 2004]. StaMPS provides a framework to estimate and remove spatiotemporally correlated phase terms from the PS network. Shankar et al. refined this algorithm by developing a maximum likelihood statistical estimation method to identify and select PS pixels based on the observed interferometric phases [Shanker and Zebker, 2007]. Additional work in PS techniques include [Kampes, 2005].

In each of these existing works, the PS is modeled as a non-decorrelating point scatterer with additive white decorrelation noise. In effect the decorrelation phase term is lumped with the thermal noise phase term, with the resultant term modeled as white Gaussian noise.

In this thesis, we examine how PS selection and deformation measurements can be improved through better statistical characterization and modeling of the decorrelation phase term. We decouple decorrelation effects from thermal noise and show that the PS decorrelation phase term is in fact partially correlated and baseline-dependent. From this model, we develop an improved statistical selection technique for partially correlated persistent scatterers (PCPS) that utilizes the full stack of phase and amplitude observations, as well as imaging geometry parameters.

Chapter 3

Spatiotemporal decorrelation of partially correlated persistent scatterers

3.1 Introduction

Interferometric synthetic aperture radar (InSAR) is an effective tool for measuring temporal changes in the Earth's surface [Gabriel et al., 1989, Rosen et al., 2000]. By combining SAR echoes collected at varying times and orbit geometries, InSAR techniques permit computations of high accuracy, wide coverage images of crustal deformation fields. InSAR has been used to study a wide range of geophysical phenomena, including seismic and volcanic activity [Massonnet et al., 1993, Zebker and Rosen, 1994, Hooper et al., 2004], land subsidence [Massonnet et al., 1997], and glacial ice flow [Zebker, 2000].

The measured radar return for a ground resolution element is the sum of complex echoes from multiple discrete scatterers located within the element. Changes in the radar imaging geometry, scatterer positions, or scattering behavior between radar passes causes the coherent sum to vary, leading to a decorrelation phase term that obscures the deformation signal and prevents the use of large baseline data. Decorrelation due to spatial and temporal baseline is a major limiting factor in estimating the crustal deformation signal from interferometric phase data [Zebker and Villasenor, 1992].

Spatial and temporal decorrelation effects may be ameliorated by using persistent scatterer (PS) techniques [Ferretti et al., 2001, Hooper et al., 2004]. Persistent scattering pixels are those in which a dominant, point-like scatterer causes the pixel to remain relatively phase-stable over the set of interferograms. By identifying a network of PS pixels, deformation measurements on the order of

millimeters may be obtained even in areas of low coherence, where conventional InSAR fails to produce useful observations [Colesanti et al., 2003a].

A quantitative theory for PS decorrelation behavior is necessary for fundamentally understanding and justifying PS techniques. Accurate PS decorrelation models also enable improved PS selection and subsequent deformation estimation algorithms. Previous work [Hooper et al., 2004, Ferretti et al., 2001, Colesanti et al., 2003b, Kampes, 2005, Agram, 2010] has generally relied on the assumption that some pixels will be less affected by spatiotemporal decorrelation, and that these pixels may be identified via simple statistical tests on the observed phase or amplitude. Thus far, however, there has not been an analytical model that justifies these assumptions by quantifying the relation between PS scattering characteristics, imaging baselines, and spatiotemporal decorrelation.

In this chapter, we present a new radar scattering model that relates the PS signal moments to physical properties of the surface. From this scattering model, we derive a new analytic model for the spatiotemporal decorrelation of persistent scatterers as a function of baseline and signal-to-clutter ratio (SCR). This model quantifies the partial correlation of persistent scatterer pixels over large baselines, providing a means to characterize and compare the phase stability of PS, non-PS, and ideal point scatterer pixels. Our analysis fundamentally explains why PS coherence remains high over large baselines and justifies the use of interferometric data with baselines equal to or greater than the critical baseline. We support our analytic models with decorrelation measurements from real InSAR data.

This chapter is arranged as follows. We first present a new PS model based on probabilistic backscattering characteristics in Section 3.2. In Section 3.3, we derive an analytical model that quantifies PS spatial decorrelation as a function of spatial baseline and signal-to-clutter ratio (SCR). We also present a series of radar scattering simulations and show that the simulated spatial decorrelation matches well with our analytic results. In Section 3.4, we present three candidate models for PS temporal decorrelation. Finally, we use our spatiotemporal decorrelation expressions with maximum likelihood SCR estimation in Section 3.6 to analyze an area of the Hayward Fault Zone, imaged by the European Remote Sensing (ERS) 1 and 2 satellites. Our results show that decorrelation observed in real radar data corresponds well with our theoretical analysis.

3.2 Persistent scatterer backscatter model

A PS pixel is typically characterized as one arising from a dominant scatterer with high backscatter power relative to surrounding non-dominant scatterers, or clutter [Kampes, 2005, Agram, 2010]. We mathematically formalize the PS characterization using the following statistical PS backscatter model.

Consider a ground resolution element ("resel") of size R_x in azimuth and R_y in range. The azimuth and ground range distances from the center of the resel are denoted by variables x and y

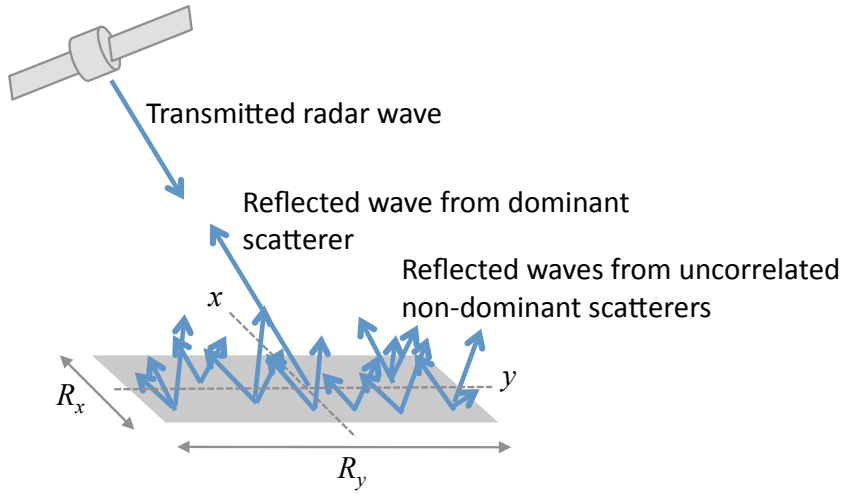

Figure 3.1: PS backscatter mechanism. The resolution element is composed of a centered dominant scatterer surrounded by uncorrelated, uniformly distributed scatterers contributing to clutter.

respectively. The dimensions of the scattering centers are assumed to be very small compared to the size of the resel. We model the scattering centers contributing to clutter as uncorrelated and uniformly spatially distributed, with average reflectivity $\frac{\sigma_c}{R_x R_y}$ over the resel, where σ_c is the radar cross section of the clutter. The dominant scatterer, located at $(x, y) = (0, 0)$, is uncorrelated with the clutter and has radar cross section σ_s.[1] The signal-to-clutter ratio of the resolution element is defined as $\text{SCR} = \sigma_s/\sigma_c$. Figure 3.1 shows a schematic of the PS backscatter mechanism.

Based on the backscatter characteristics described above, we model the surface backscatter within the patch as a complex random spatial function $f(x, y)$. We can decompose $f(x, y)$ into a signal component arising from the dominant scatterer and a clutter component, denoted $f_s(x, y)$ and $f_c(x, y)$ respectively:

$$f(x, y) = f_s(x, y) + f_c(x, y). \tag{3.1}$$

Both $f_s(x, y)$ and $f_c(x, y)$ are modeled as zero mean random spatial functions that are uncorrelated

[1] If the dominant scatterer is not located at the origin, an additional decorrelation term will arise; this analysis will be left for future presentation. In principle, the subpixel position of the dominant scatterer can be estimated [Adam et al., 2003] and the image resampled such that the dominant scatterer lies in the center of the resolution element.

for all x, y, x', y'. The autocorrelation function of $f(x,y)$ is therefore given by

$$\mathrm{E}[f(x,y)f^*(x',y')] = \begin{cases} \frac{\sigma_c}{R_x R_y} & \text{if } (x,y) = (x',y') \neq (0,0) \\ \sigma_s + \frac{\sigma_c}{R_x R_y} & \text{if } (x,y) = (x',y') = (0,0) \\ 0 & \text{if } (x,y) \neq (x',y') \end{cases} \tag{3.2}$$

$$= \frac{\sigma_c}{R_x R_y}\delta(x-x',y-y') + \sigma_s \delta(x,y)\delta(x-x',y-y') \tag{3.3}$$

where $\delta(.,.)$ denotes the two-dimensional Dirac delta function.

Note that this PS model constrains only the first and second moments of the backscatter function and the location of the dominant scatterer. The actual probability distribution function of the backscatter random spatial process does not need to be constrained for our ensuing analysis.

In the following sections, we examine how explicit expressions for PS decorrelation derive from this backscatter model.

3.3 Analytic spatial decorrelation

Spatial decorrelation arises from changes in the radar orbiting geometry relative to the scatterer positions.

3.3.1 Derivation

We consider an interferometric radar system imaging the surface described in Section 3.2. Two antennas illuminate the surface from incidence angles θ_1 and θ_2. For convenience, we assume that the radar data are sampled such that the single look pixel is approximately the same size as the resolution element. The complex pixel values in the processed SAR images are given by the superposition integrals

$$s_1 = \iint f(-x,-y)e^{-j\frac{4\pi}{\lambda}(r+y\sin\theta_1)}W(x,y)dxdy \tag{3.4}$$

$$s_2 = \iint f(-x,-y)e^{-j\frac{4\pi}{\lambda}(r+y\sin\theta_2)}W(x,y)dxdy, \tag{3.5}$$

where r is the distance from the sensor to the center of the resolution element, λ is the radar wavelength, and $W(x,y)$ is the radar imaging impulse response [Zebker and Villasenor, 1992].Because a change in r between radar passes does not affect the magnitude of correlation, we assume for simplicity that r is equal for both antennas.

Using the typical impulse response $W(x,y) = \mathrm{sinc}(\frac{x}{R_x})\mathrm{sinc}(\frac{y}{R_y})$ and the PS backscatter function

$f(x, y)$ modeled in Section 3.2, the expected interferometric pixel value reduces to

$$\mathrm{E}[s_1 s_2^*] = \iiiint \mathrm{E}[f(-x,-y)f^*(-x',-y')]\cdot \tag{3.6}$$

$$e^{-j\frac{4\pi}{\lambda}(y\sin\theta_1 - y'\sin\theta_2)} W(x,y)W^*(x',y')dxdydx'dy' \tag{3.7}$$

$$= \sigma_c \int e^{-j\frac{4\pi}{\lambda}y(\sin\theta_1 - \sin\theta_2)}\mathrm{sinc}^2(y)dy + \sigma_s. \tag{3.8}$$

The first term may be interpreted as the Fourier transform of the function $\mathrm{sinc}^2(y)$. Evaluating the transform yields the result

$$\mathrm{E}[s_1 s_2^*] = \begin{cases} \sigma_c\left(1 - \frac{2R_y(\sin\theta_1 - \sin\theta_2)}{\lambda}\right) + \sigma_s, & \sin\theta_1 - \sin\theta_2 < \frac{\lambda}{2R_y} \\ \sigma_s, & \sin\theta_1 - \sin\theta_2 \geq \frac{\lambda}{2R_y}. \end{cases} \tag{3.9}$$

Typically the incidence angle changes very little between radar passes; both θ_1 and θ_2 deviate from a nominal incidence angle θ by only a small amount. We can therefore write $\theta_1 = \theta + \delta\theta_1$ and $\theta_2 = \theta + \delta\theta_2$. Using a Taylor series expansion about θ and discarding higher order terms, we find that $\sin\theta_1 - \sin\theta_2 \approx (\theta_1 - \theta_2)\cos\theta$. When the perpendicular baseline B is much smaller than the range r, as is usually the case, then $\theta_1 - \theta_2 \approx \frac{B}{r}$. Hence, the expected interferometric pixel value can be rewritten in terms of perpendicular baseline as

$$\mathrm{E}[s_1 s_2^*] = \begin{cases} \sigma_c\left(1 - \frac{2R_y\cos\theta|B|}{\lambda r}\right) + \sigma_s, & |B| < B_{\mathrm{crit}} \\ \sigma_s, & |B| \geq B_{\mathrm{crit}}, \end{cases} \tag{3.10}$$

where the critical baseline is given by [Zebker and Villasenor, 1992]

$$B_{\mathrm{crit}} = \frac{\lambda r}{2R_y\cos\theta}. \tag{3.11}$$

Finally, after normalizing by the factor

$$\frac{1}{\sqrt{\langle s_1 s_1^*\rangle}\sqrt{\langle s_2 s_2^*\rangle}} = \frac{1}{\sigma_c + \sigma_s}, \tag{3.12}$$

we arrive at the following analytic spatial correlation function[2]:

$$\begin{aligned}\rho_{\text{spatial}}(B;\text{SCR}) &= \frac{\langle s_1 s_2^* \rangle}{\sqrt{\langle s_1 s_1^* \rangle}\sqrt{\langle s_2 s_2^* \rangle}} \\ &= \begin{cases} \frac{1}{1+\text{SCR}}\left(1 - \frac{2R_y \cos\theta|B|}{\lambda r}\right) + \frac{\text{SCR}}{1+\text{SCR}}, & |B| < B_{\text{crit}} \\ \frac{\text{SCR}}{1+\text{SCR}}, & |B| \geq B_{\text{crit}}. \end{cases}\end{aligned} \tag{3.13}$$

Equation 3.13 shows that the spatial correlation of a PCPS pixel is a weighted sum of correlation terms. The first term, arising solely from clutter, decreases linearly as the perpendicular baseline increases, until the critical baseline is reached. At that point, the clutter decorrelates completely, and the associated term in the expression goes to 0. The second term in the expression is the constant correlation of an ideal point scatterer and is independent of baseline. The weights of these terms are determined by the signal-to-clutter ratio of the resolution element. Theoretical PCPS spatial decorrelation plots for varying SCR are shown in Figure 3.2.

As a check, we see that when no dominant scatterer exists, the correlation expression reduces to

$$\rho_{\text{spatial}}(B;\text{SCR}=0) = \begin{cases} 1 - \frac{2R_y \cos\theta|B|}{\lambda r}, & |B| < B_{\text{crit}} \\ 0, & |B| \geq B_{\text{crit}}. \end{cases} \tag{3.14}$$

This result matches the correlation expression derived in [Zebker and Villasenor, 1992] for a fully distributed scattering pixel. When SCR increases to infinity, ρ_{spatial} approaches a constant value of 1, as expected for an ideal point scatterer which does not decorrelate with spatial baseline.

The PCPS spatial decorrelation expression in Equation 3.13 provides a quantitative measure of theoretical PS phase stability. We can use this expression to calculate the improvement in correlation for non-zero-SCR pixels over fully distributed scattering pixels for any given baseline. Similarly, we can quantify the difference between an ideal point scatterer and a partially correlated persistent scatterer with finite SCR. Finally, the expression justifies the use of large spatial baseline data in PS analysis, since it shows that pixels with high SCR maintain coherence at baselines greater than B_{crit}.

3.3.2 Simulation

To verify the theoretical analysis of Section 3.3.1, we compute a series of radar scattering simulations and calculate the resulting decorrelation as a function of spatial baseline for varying values of SCR. We set the simulated radar parameter values to those typical for a C-band system: $\lambda = 0.0566$ m, $\theta = 23.3°$, $R_x = 6.5$ m, $R_y = 24.3$ m, $B_{\text{crit}} = 1052$ m.

For each value of SCR, we simulate 100 pixels. Each pixel k is generated from a radar ground

[2]We use the notation $f(x;\mathbf{p})$ to denote a function f of variable x that is parameterized by $\mathbf{p}$.

swath with uniformly distributed scatterers, where each resel within the swath contains an average of 100 scatterers. The complex reflectivity of the scatterers are independently distributed according to the circularly symmetric complex normal distribution $\mathcal{CN}(0, \frac{1}{1+\text{SCR}}\frac{100}{R_x R_y})$. A dominant scatterer with radar cross section $\frac{\text{SCR}}{1+\text{SCR}}$ is simulated at the center of the resel. We then compute the SAR image pixels $s_1^{(k)}$, $s_2^{(k)}$ and resulting interferometric pixel $z^{(k)}$ over a range of spatial baseline values B:

$$z^{(k)}(B, \text{SCR}) = s_1^{(k)}(\text{SCR}) s_2^{(k)*}(B, \text{SCR}). \tag{3.15}$$

Finally, we compute the spatial decorrelation by ensemble averaging over the 100 simulated pixels for each pair of SCR and B values:

$$\rho_{\text{spatial}}(B, \text{SCR}) = \tag{3.16}$$

$$\left| \frac{\sum_{k=1}^{N_i} z^{(k)}(B, \text{SCR})}{\sqrt{\sum_{k=1}^{N_i} s_1^{(k)}(\text{SCR}) s_1^{(k)*}(\text{SCR})} \sqrt{\sum_{k=1}^{N_i} s_2^{(k)}(B, \text{SCR}) s_2^{(k)*}(B, \text{SCR})}} \right|. \tag{3.17}$$

The simulation results are plotted in Figure 3.2. As expected, we find that the simulated spatial decorrelation, shown in red, corresponds well with the analytic decorrelation derived in Equation 3.13, plotted in blue.

3.3.3 Random dominant scatterer position

If the dominant scatterer is located at a random unknown position rather than centered at the origin of the resel, we expect increased spatial decorrelation. By modeling the distribution of the dominant scatterer position as uniform over the resel, we can quantify the expected increase in decorrelation, leading to a more general model for PCPS spatial decorrelation. This analytical generalization is left for future work.

3.4 Temporal decorrelation models

In this section, we discuss possible models for PS temporal decorrelation. Temporal decorrelation arises from changes in the sub-pixel scatterer positions and reflectivity between radar passes. In general, temporal decorrelation is a complex phenomenon that depends on several factors, including vegetation type, land use, seasonal effects, wind patterns, biomass, and radar wavelength [Askne and Smith, 1997, Ahmed et al., 2008, Meng and Sandwell, 2010, Ahmed et al., 2011, Lee et al., 2013] over varying time scales. For PCPS temporal decorrelation, we focus on understanding and modeling the dependence on SCR.

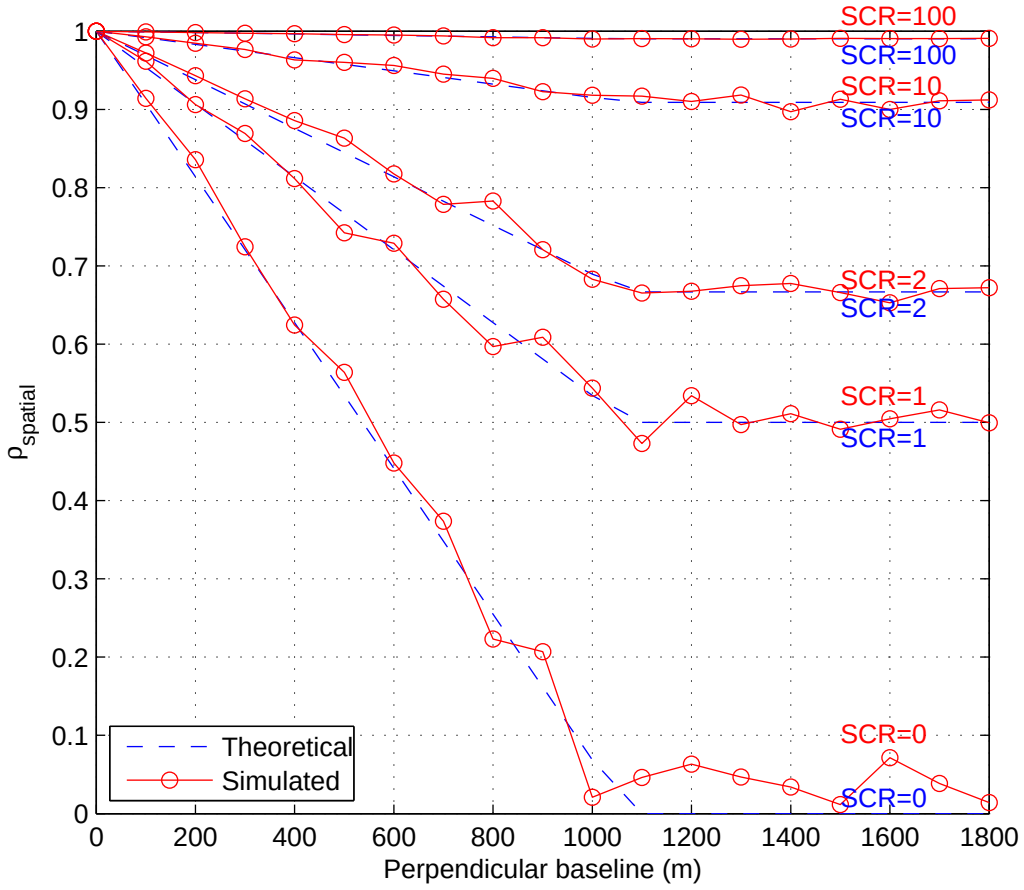

Figure 3.2: Analytic and simulated spatial decorrelation

3.4.1 Linear temporal decorrelation models

This model is based on the empirical observation that correlation decreases linearly with temporal baseline T in a variety of terrain [Zebker and Villasenor, 1992].

Base model

In our first model, the temporal correlation is constrained to equal 1 (perfect correlation) when $T = 0$. The decorrelation function then decreases linearly to 0 (complete decorrelation) when $T = T_{\text{crit}}$, where the critical temporal baseline T_{crit} is the parameter of the model. The decorrelation function is expressed as

$$\rho_{\text{temp1}}(T; T_{\text{crit}}) = \begin{cases} 1 - \frac{|T|}{T_{\text{crit}}}, & |T| < T_{\text{crit}} \\ 0, & |T| \geq T_{\text{crit}}. \end{cases} \tag{3.18}$$

The perfect correlation constraint at zero baseline makes theoretical sense, since no temporal decorrelation should occur if the two radar passes occur at the same time.

Unconstrained short term decorrelation

In this model, we add another degree of freedom to the first model by making the correlation value at $T = 0$ a parameter of the model, denoted ρ_0. This parameter allows for the possibility of independent short-term decorrelating effects – those that happen over time spans shorter than the radar repeat interval – and long-term decorrelation. The rate of long-term decorrelation is determined by the critical temporal baseline parameter T_{crit}. The resulting decorrelation function is

$$\rho_{\text{temp2}}(T; T_{\text{crit}}, \rho_0) = \begin{cases} \min(\rho_0 - \frac{\rho_0 |T|}{T_{\text{crit}}}, 1), & |T| < T_{\text{crit}} \\ 0, & |T| \geq T_{\text{crit}}. \end{cases} \tag{3.19}$$

Linearly decorrelating clutter with stationary dominant scatterer

The third temporal decorrelation model is based on the persistent scatterer model presented in Section 3.2, extended to account for temporal variation. We now denote the PS backscatter function as $f(x, y, t)$ to indicate its dependence on time t. As before, we can decompose the backscatter function into its signal and clutter components

$$f(x, y, t) = f_s(x, y, t) + f_c(x, y, t), \tag{3.20}$$

where $f_s(x, y, t)$ and $f_c(x, y, t)$ are each spatially uncorrelated functions for all t. Additionally, $f_c(x, y, t)$ is uncorrelated with $f_s(x', y', t')$ for all x, x', y, y', t, t'. We further assume that the

dominant scatterer does not move or vary in backscatter between radar passes, i.e. $f_s(x, y, t) = f_s(x, y, t')$ for all x, y, t, t'.

Based on the modeling assumptions here and in Section 3.2, we can decompose the autocorrelation of the backscatter function into a sum of signal autocorrelation and clutter autocorrelation. Consequently, the expected interferometric pixel value and temporal decorrelation can be similarly decomposed. The signal component of ρ_{temp} is given by

$$\frac{1}{\sigma_c + \sigma_s} \iiiint \mathrm{E}[f_s(-x, -y, t) f_s^*(-x', -y', t')] e^{-j\frac{4\pi}{\lambda}(y-y')\sin\theta}. \tag{3.21}$$

$$W(x, y) W^*(x', y') dx dy dx' dy' = \frac{\mathrm{SCR}}{1 + \mathrm{SCR}}. \tag{3.22}$$

We model the clutter component of ρ_{temp} as decreasing linearly with temporal baseline according to the constrained model in 3.4.1. We assume that the clutter component is weighted relative to the signal component as in Equation 3.13. The resulting total temporal decorrelation is then

$$\rho_{\text{temp3}}(T; T_{\text{crit}}, \rho_f) = \begin{cases} (1 - \rho_f)(1 - \frac{|T|}{T_{\text{crit}}}) + \rho_f, & |T| < T_{\text{crit}} \\ \rho_f, & |T| \geq T_{\text{crit}}. \end{cases} \tag{3.23}$$

Figure 3.3 displays the linear decorrelation base model, linear decorrelation model with unconstrained short term decorrelation, and linear decorrelation model with stationary dominant scatterer, plotted for varying values of their parameters.

3.4.2 Exponential temporal decorrelation models

If distributed scatterers within a resolution element move independently with Gaussian-distributed change of position in each direction, then the resulting theoretical correlation decreases exponentially with the root mean square displacement [Zebker and Villasenor, 1992]. Below, we suggest directions for adapting this analytical model to PCPS temporal decorrelation.

Base model

If the change in scatterer position in each spatial dimension is independent of other scatterers, independent of its motion in all other dimensions, and Gaussian distributed, then a pixel of distributed scatterers decorrelates as a function of the root mean square displacement in range σ_y and height σ_z [Zebker and Villasenor, 1992]:

$$\rho(\sigma_y, \sigma_z) = e^{-\frac{1}{2}\left(\frac{4\pi}{\lambda}\right)^2 (\sigma_y^2 \sin^2\theta + \sigma_z^2 \cos^2\theta)}. \tag{3.24}$$

In order to derive the dependence on temporal baseline, we assume that each scatterer maintains an average rate of movement in the range direction, denoted m_y, and neglect movement in the height

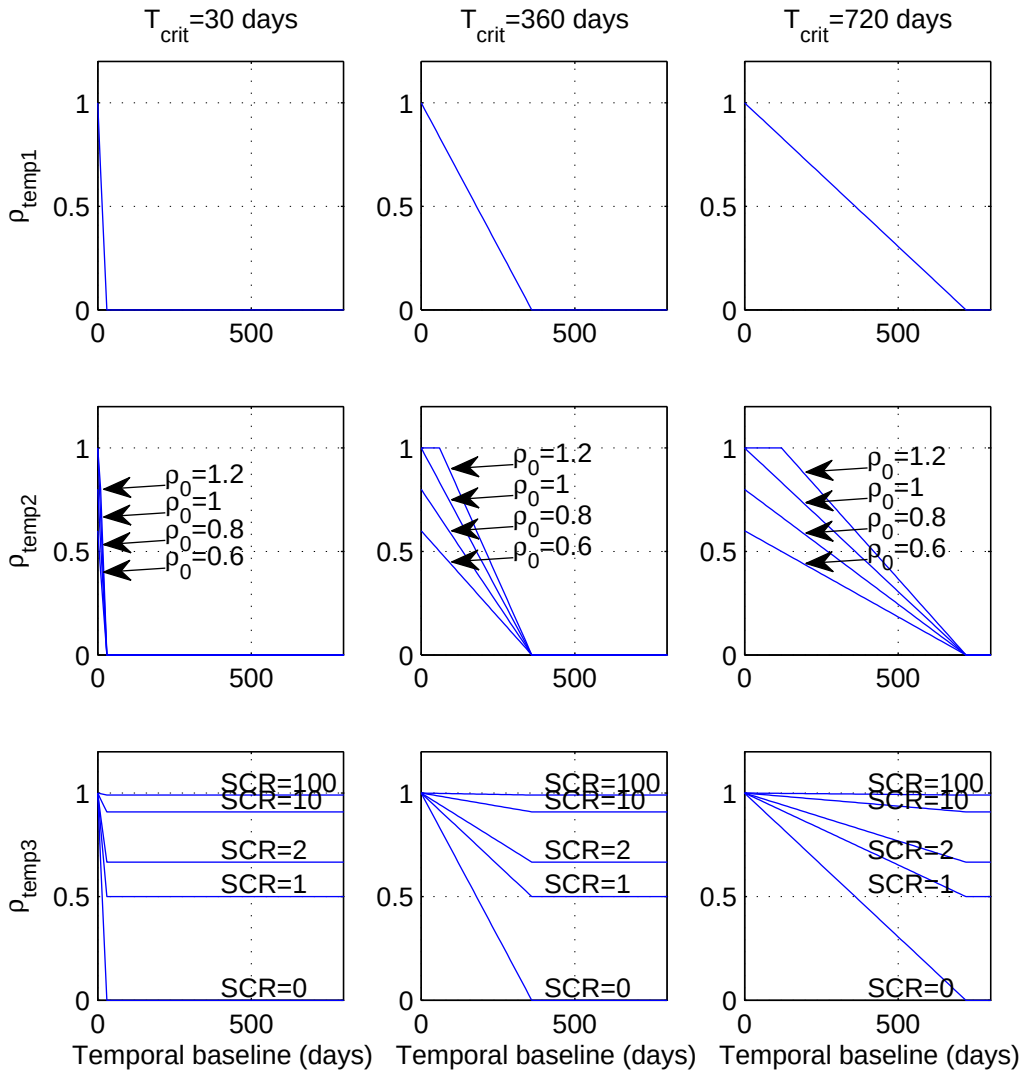

Figure 3.3: The constrained linear (ρ_{temp1}), unconstrained linear (ρ_{temp2}), and weighted sum (ρ_{temp3}) temporal decorrelation models. Each plot displays a temporal decorrelation model plotted for the value of T_{crit} listed at the top of the column. The unconstrained linear and weighted sum models are further plotted for varying values of ρ_0 and SCR, respectively.

dimension for simplicity.[3] Under these assumptions, we perform a change of variables $\sigma_y = m_y T$, resulting in correlation as a function of temporal baseline T:

$$\rho_{\text{temp}}(T; m_y) = e^{-\frac{1}{2}\left(\frac{4\pi}{\lambda}\right)^2 (m_y T)^2} \tag{3.25}$$

To generalize this model, we group terms into a single parameter σ_T that expresses the rate of temporal decorrelation decay:

$$\rho_{\text{temp}}(T; \sigma_T) = e^{-\frac{T^2}{2\sigma_T^2}}. \tag{3.26}$$

In future work, this model should be modified to account for random motion in the height dimension and for true Brownian motion, where the direction of displacement between each radar pass is random and uniformly distributed.

Unconstrained short term decorrelation effects

Again, we account for different short-term and long-term decorating effects by allowing a non-unity initial temporal decorrelation at ρ_0. This parameter allows for the possibility of decorrelating effects that happen over time spans shorter than the radar repeat interval.

The resulting temporal decorrelation model is parameterized by the decay parameter σ_T and the short term decorrelation factor ρ_0:

$$\rho_{\text{temp}}(T; \rho_0, \sigma_T) = \rho_0 e^{-\frac{T^2}{2\sigma_T^2}}. \tag{3.27}$$

Exponentially decorrelating clutter with stationary dominant scatterer

We now denote the PS backscatter function as $f(x, y, t)$ to indicate its dependence on time t. As before, we can decompose the backscatter function into its signal and clutter components

$$f(x, y, t) = f_s(x, y, t) + f_c(x, y, t), \tag{3.28}$$

where $f_s(x, y, t)$ and $f_c(x, y, t)$ are each spatially uncorrelated functions for all t. We additionally assume that $f_c(x, y, t)$ is uncorrelated with $f_s(x', y', t')$ for all x, x', y, y', t, t'. Based on the modeling assumptions here and in Section 3.2, we can decompose the autocorrelation of the backscatter function into a sum of signal autocorrelation and clutter autocorrelation. Consequently, the expected interferometric pixel value and temporal decorrelation can be similarly decomposed.

[3] Due to symmetry between the range and height variables in Equation 3.24, the results can be extended easily to include movement in the height dimension.

We assume that the dominant scatterer does not move or vary in backscatter between radar passes, i.e. $f_s(x, y, t) = f_s(x, y, t')$ for all x, y, t, t'. This scenario is feasible for persistent scatterers arising from a strongly reflecting fixed object such as a road or manmade reflector placed in natural terrain. The signal component of ρ_{temp} is given by

$$\frac{1}{\sigma_c + \sigma_s} \iiiint \mathrm{E}[f_s(-x, -y, t) f_s^*(-x', -y', t')] e^{-j\frac{4\pi}{\lambda}(y-y')\sin\theta}. \tag{3.29}$$

$$W(x, y) W^*(x', y') dx dy dx' dy' = \frac{\mathrm{SCR}}{1 + \mathrm{SCR}}. \tag{3.30}$$

Assuming that the dominant scatterer remains unmoving while the non-dominant scatterers move according to the assumptions in Section 3.4.2, the temporal decorrelation is given by

$$\rho_{\text{temp}}(T; \sigma_T, \mathrm{SCR}) = \frac{1}{1 + \mathrm{SCR}} e^{-\frac{T^2}{2\sigma_T^2}} + \frac{\mathrm{SCR}}{1 + \mathrm{SCR}}. \tag{3.31}$$

Finally, we note that several more sophisticated temporal decorrelation models exist in the literature (e.g. [Lavalle et al., 2012]). The models described above may be extended to account for more complex temporal decorrelation effects in future work.

3.5 Other decorrelation terms

Other sources of decorrelation include relative rotation of the orbit path [Zebker and Villasenor, 1992], volumetric scattering [Hoen et al., 2000], and thermal noise [Ahmed et al., 2011]. The total decorrelation is the product of the various decorrelation terms. We group the non-spatiotemporal decorrelation multiplicative terms into a single term ρ_{other}, resulting in the following total correlation expression:

$$\rho = \rho_{spatial} \cdot \rho_{temporal} \cdot \rho_{other} \tag{3.32}$$

3.6 Comparison with data: Hayward Fault Zone analysis

In this section, we analyze PS decorrelation trends in ERS radar data and compare the results to our theoretically derived PS decorrelation expression. We first describe our interferometric radar data set and pre-processing steps to remove nuisance phase terms. Next, we implement a maximum likelihood technique to estimate the SCR of each pixel. We then calculate the decorrelation in the data as a function of SCR and baseline. Finally, we choose the best fit parameters of our analytic decorrelation expression for the data and analyze the results.

Parameter		Value
Wavelength	λ	0.0566 m
Look angle	θ	23.3°
Azimuth resolution	R_x	6.5 m
Ground range resolution	R_y	24.3 m
Critical baseline	B_{crit}	1052 m
Number of interferograms	N_{ifg}	37

Table 3.1: InSAR system parameters for Hayward Fault Zone analysis

3.6.1 Interferometric data

Our data set consists of 38 descending SAR acquisitions collected by the European Remote Sensing (ERS-1/2) radar satellites between May 1995 and December 2000 (Track 70, Frame 2853). Parameters of the ERS system are listed in Table 3.1. The images cover a 29 km by 31 km area at the southern end of the San Francisco Bay, near the Hayward Fault Zone. Areas of urban infrastructure occur in the upper left and bottom edge of the image, while the central part of the image is largely natural terrain.

We form a stack of $N_{\text{ifg}} = 37$ single look interferograms using an acquisition from December 1997 as the common master. Figure 3.4 displays one such interferogram, created with a September 1997 acquisition as the slave image. The interferogram shows that a large portion of the area suffers low coherence due to natural terrain, even at relatively low temporal baseline.

In order to analyze decorrelation of the data set, we wish to first remove deformation and atmospheric effects from the interferometric phase. We assume that the deformation and atmospheric phase components are both characterized by low spatial frequency, while phase terms arising from spatial baseline, temporal baseline, and noise are spatially uncorrelated [Emardson et al., 2003, Hooper, 2006]. Each interferogram is processed with a 10-by-10-pixel low pass filter, and the resulting signal is subtracted from the interferogram. The remaining interferometric phase is assumed to consist of only the spatial, temporal, and noise decorrelation terms. While more sophisticated methods may be applied to remove nuisance phase components, we chose to use a relatively simple filter in order to focus primarily on the decorrelation analysis.

3.6.2 Methodology

Maximum likelihood SCR estimation

We estimate the SCR of each pixel using the maximum likelihood (ML) technique developed by Shanker and Zebker [Shanker and Zebker, 2007]. Each pixel is processed individually. For each pixel i, we assume the interferometric pixel value z_i is independently and identically distributed as a complex circular Gaussian around a constant signal in each interferogram. The SCR of the pixel is given by the ratio of signal amplitude to Gaussian variance. The interferometric phase of pixel

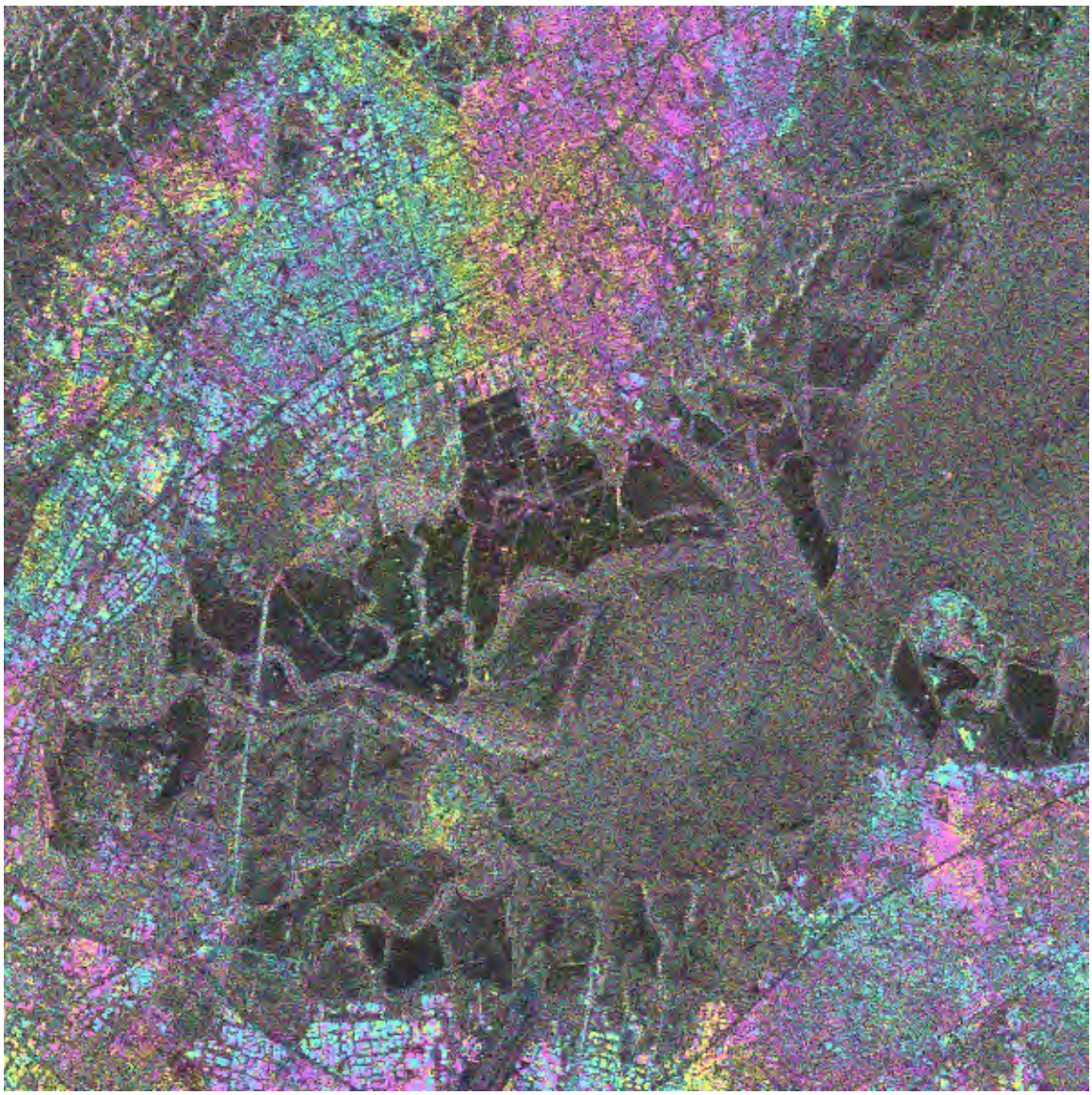

Figure 3.4: Sample interferogram from ERS stack, September 1997 (slave)-December 1997 (master). For display purposes, the image has been scaled to produce square pixels.

i in each interferogram is then independently and identically distributed according to the following distribution, parameterized by SCR [Abramowitz and Stegun, 1972]:

$$p_\phi(\phi; \mathrm{SCR}) = \frac{1}{2\pi} e^{-\mathrm{SCR}\sin^2(\phi)}. \tag{3.33}$$

$$\{e^{-\mathrm{SCR}\cos^2(\phi)} + \sqrt{\pi \mathrm{SCR}}\cos(\phi)[1 - \mathrm{erf}(-\sqrt{\mathrm{SCR}\cos(\phi)})]\}. \tag{3.34}$$

The joint PDF of all the interferometric phases in the stack, denoted $\phi_{i,1}, \ldots, \phi_{i,N_{\mathrm{ifg}}}$, is then given by

$$p(\phi_{i,1}, \ldots, \phi_{i,N_{\mathrm{ifg}}}; \mathrm{SCR}) = \prod_{k=1}^{N_{\mathrm{ifg}}} p_\phi(\phi_{i,k}; \mathrm{SCR}). \tag{3.35}$$

We estimate the SCR of the pixel by maximizing the joint phase PDF over the SCR parameter, given the observed phases $\phi_{i,1}, \ldots, \phi_{i,N_{\mathrm{ifg}}}$:

$$\mathrm{SCR}_{\mathrm{ML},i} = \arg\max_{\mathrm{SCR}} p(\phi_{i,1}, \ldots, \phi_{i,N_{\mathrm{ifg}}}; \mathrm{SCR}) \tag{3.36}$$

$$= \arg\max_{\mathrm{SCR}} \prod_{k=1}^{N_{\mathrm{ifg}}} p_\phi(\phi_{i,k}; \mathrm{SCR}) \tag{3.37}$$

A map of the estimated SCR values is displayed in Figure 3.5. The map shows that the estimated SCR is roughly correlated with the terrain; areas with urban infrastructure (in the upper left and lower portions of the image) tend to have slightly higher estimated SCR than vegetated or natural areas. Figure 3.6 shows a histogram of SCR values, with the number of pixels is displayed in $\log_{10}$-scale. The vast majority of pixels have very low estimated SCR (< 0.3), as we would expect for terrain that is largely vegetated and devoid of many dominant scattering centers.

Decorrelation estimation

We wish to measure the observed decorrelation as a function of perpendicular baseline, temporal baseline, and SCR. Because adjacent pixels in general have different SCR, we cannot estimate the decorrelation of individual pixels via spatial averaging, as is usually done. Instead, we estimate the decorrelation by averaging over pixels of near-equal estimated SCR, independent of the pixel locations.

In order to group pixels of similar estimated SCR, we truncate each pixel's maximum likelihood SCR value to one decimal digit. Pixels are then partitioned into sets of equal truncated SCR values. The resulting sets of pixel indices may be defined as

$$\mathcal{S}_j = \{i \mid 0.1j \leq \mathrm{SCR}_{\mathrm{ML},i} < 0.1(j+1)\},\ j = 0, 1, 2, \ldots. \tag{3.38}$$

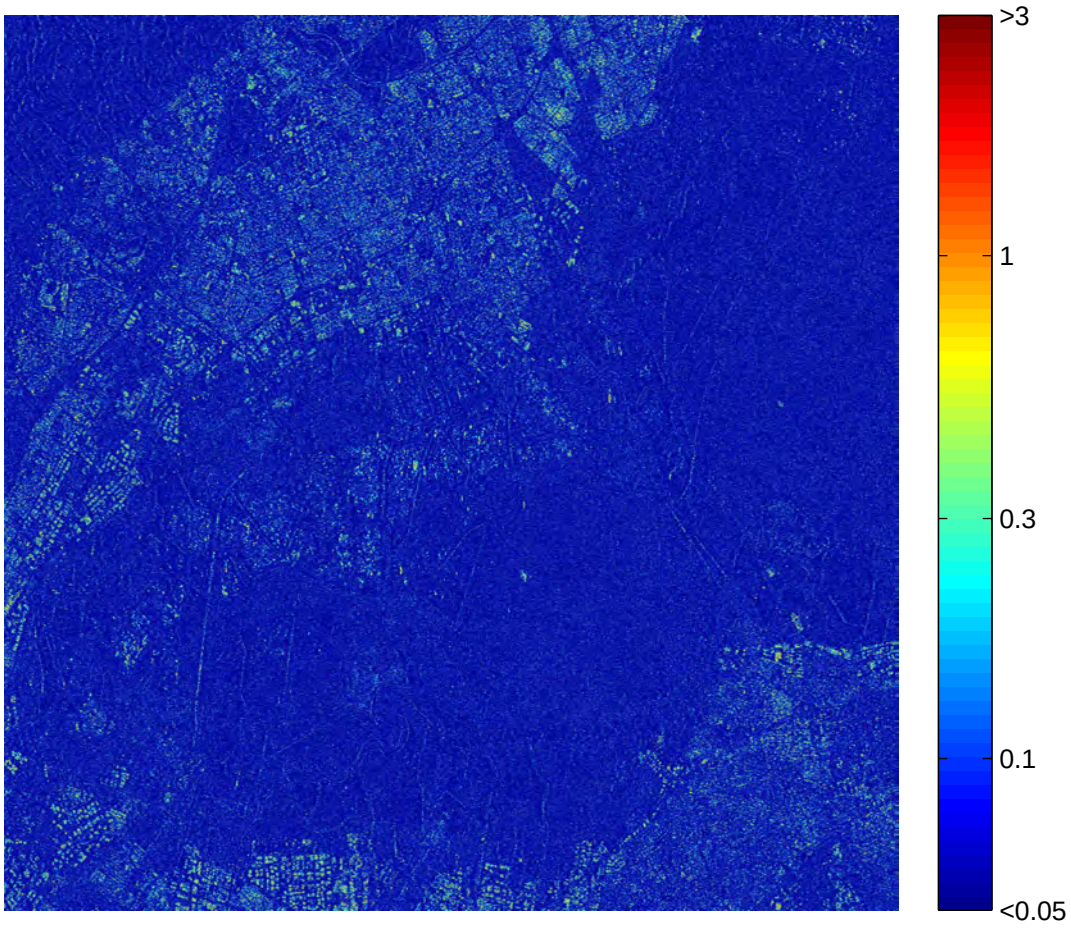

Figure 3.5: Maximum likelihood estimated SCR. For display purposes, the image has been scaled to produce square pixels.

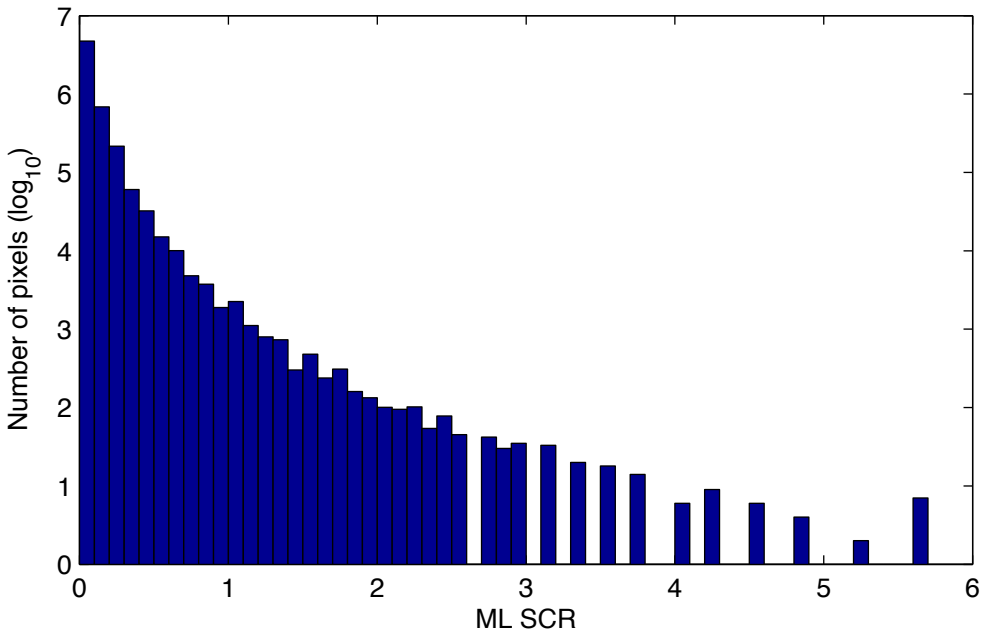

Figure 3.6: Histogram of maximum likelihood estimated SCR values. Binning corresponds to the pixel sets used to calculate decorrelation in Section 3.6.2.

Set $\mathcal{S}_0$ contains pixels with estimated SCR between 0 and 0.1, set $\mathcal{S}_1$ contains pixels with estimated SCR between 0.1 and 0.2, and so on. The histogram bins in Figure 3.6 correspond to these sets.

We now calculate the observed correlation over each set of pixels. Each interferogram k, characterized by its perpendicular baseline B_k and temporal baseline T_k, is processed individually. The correlation for pixels in set $\mathcal{S}_j$ in interferogram k is given by

$$\rho_j(B_k, T_k) = \frac{\sum_{i \in \mathcal{S}_j} s_k^{(i)} [s_0^{(i)}]^*}{\sqrt{\sum_{i \in \mathcal{S}_j} s_0^{(i)} [s_0^{(i)}]^*} \sqrt{\sum_{i \in \mathcal{S}_j} s_k^{(i)} [s_0^{(i)}]^*}} \tag{3.39}$$

$$\text{for } j = 0, 1, 2, \ldots, \tag{3.40}$$

$$k = 1, \ldots, N_{\text{ifg}}, \tag{3.41}$$

where $s_0^{(i)}$ is the master SAR pixel i and $s_k^{(i)}$ is the slave SAR pixel i. Hence, for for each range of estimated SCR values, we obtain a collection of decorrelation data points that vary with perpendicular baseline B_k and temporal baseline T_k.

Decorrelation model fitting

For each set of pixels $\mathcal{S}_j$ with estimated SCR between $0.1j$ and $0.1(j+1)$, we wish to fit our theoretical decorrelation model to the observed data points $\rho_j(B_k, T_k)$. Given the preprocessing of the interferometric data, we assume that the most significant sources of coherence loss in $\rho_j(B_k, T_k)$ are spatial decorrelation and temporal decorrelation. The total spatiotemporal decorrelation is given by the product of the spatial and temporal decorrelation models [Zebker and Villasenor, 1992]:

$$\rho_{\text{spatiotemp}}(B, T; \text{SCR}, \mathbf{p}_{\text{temp}}) = \rho_{\text{spatial}}(B; \text{SCR}) \cdot \rho_{\text{temp}}(T; \mathbf{p}_{\text{temp}}). \tag{3.42}$$

The spatial decorrelation component of Equation 3.42 is given by the expression derived in Section 3.3.1:

$$\rho_{\text{spatial}}(B; \text{SCR}) = \begin{cases} \frac{1}{1+\text{SCR}} \left(1 - \frac{2R_y \cos\theta |B|}{\lambda r}\right) + \frac{\text{SCR}}{1+\text{SCR}}, & |B| < B_{\text{crit}} \\ \frac{\text{SCR}}{1+\text{SCR}}, & |B| \geq B_{\text{crit}}, \end{cases} \tag{3.43}$$

where $B_{\text{crit}} = \frac{\lambda r}{2R_y \cos\theta}$.

Our goal is to find the best-fitting analytic spatiotemporal decorrelation model $\rho_{\text{spatiotemp}}$ for the decorrelation data points $\rho_j(B_k, T_k)$; that is, we wish to determine the best parameters for the spatial decorrelation model and each of the candidate temporal decorrelation models described in Section 3.4. We then analyze the best fit model parameters and compare the best fit SCR values to the ML SCR values calculated in Section 3.6.2.

Before model fitting, we first discard any data points $\rho_j(B_k, T_k)$ if the size of the pixel set $\mathcal{S}_j$ is

Set	ML SCR range	Number of pixels	Effective ML SCR	Description
$\mathcal{S}_0$	0.0-0.1	4,721,277	0.0312	Poorly correlated
$\mathcal{S}_{10}$	1.0-1.1	2,245	1.0358	Moderately correlated
$\mathcal{S}_{20}$	2.0-2.1	101	2.0303	Well correlated

Table 3.2: Characteristics of pixel sets presented in Figures 3.7-3.8

less than 3.

We use a minimum root mean square error (RMSE) criterion for model fitting, searching over a range of possible values for the model parameters $\mathbf{p}$. Each set of pixels $\mathcal{S}_j$, characterized by their effective ML SCR value $\text{SCR}_{\text{MLeff},j}$, is analyzed individually. The best fitting model parameters for set $\mathcal{S}_j$ are given by

$$\begin{bmatrix} \text{SCR}_{\text{fit},j} \\ \mathbf{p}_{\text{tempfit},j} \end{bmatrix} = \arg \min_{\text{SCR},\mathbf{p}_{\text{temp}}} \sqrt{\frac{1}{|\mathcal{S}_j|} \sum_{k=1}^{N_{\text{ifg}}} |\rho_{\text{spatiotemp}}(B_k, T_k; \text{SCR}, \mathbf{p}_{\text{temp}}) - \rho_j(B_k, T_k)|^2}. \quad (3.44)$$

3.6.3 Results

We first present the decorrelation data points $\rho_j(B_k, T_k)$ with their best fit models for three representative pixel sets $\mathcal{S}_j$, described in Table 3.2. Figure 3.7 shows the measured decorrelation data plotted versus spatial baseline B. The subplots in each column display the data points $\rho_j(B_k, T_k)$ for the same pixel set $\mathcal{S}_j$, while each row corresponds to a different model for the temporal decorrelation component. The best fit spatiotemporal decorrelation model for the data points is plotted in red. Figure 3.8 shows the same data points $\rho_j(B_k, T_k)$, now plotted versus temporal baseline T. The best fit spatiotemporal model for the data points is again plotted in red.

A qualitative examination of the decorrelation data points $\rho_j(B_k, T_k)$ clearly reveals linearly decreasing correlation as the spatial baseline B_k increases. The correlation also increases with the estimated SCR. We expect both of these trends based on our theoretical analysis. The agreement between our theoretical analysis and measured data is reflected by the increasing best fit model SCR_{fit} as the effective measure SCR increases. Figures 3.7-3.8 show that the measured decorrelation data points $\rho_j(B_k, T_k)$ trend more strongly with spatial baseline than with temporal baseline. In general, there does not appear to be a strong trend of decorrelation with temporal baseline. This may be because the temporal decorrelation trends are obscured by a stronger spatial decorrelation trend.

Figure 3.9 compares the best fit model parameters over all pixel sets $\mathcal{S}_j$ according to their effective ML SCR values $\text{SCR}_{\text{MLeff},j}$. Figure 3.9(a) shows the best fit SCR values. The constrained and weighted sum linear temporal models generally agree at low SCR (< 1), but then diverge as the SCR increases. Using the unconstrained temporal decorrelation model, however, we obtain agreement between the estimated and best fit SCR values, almost throughout the full range of SCR.

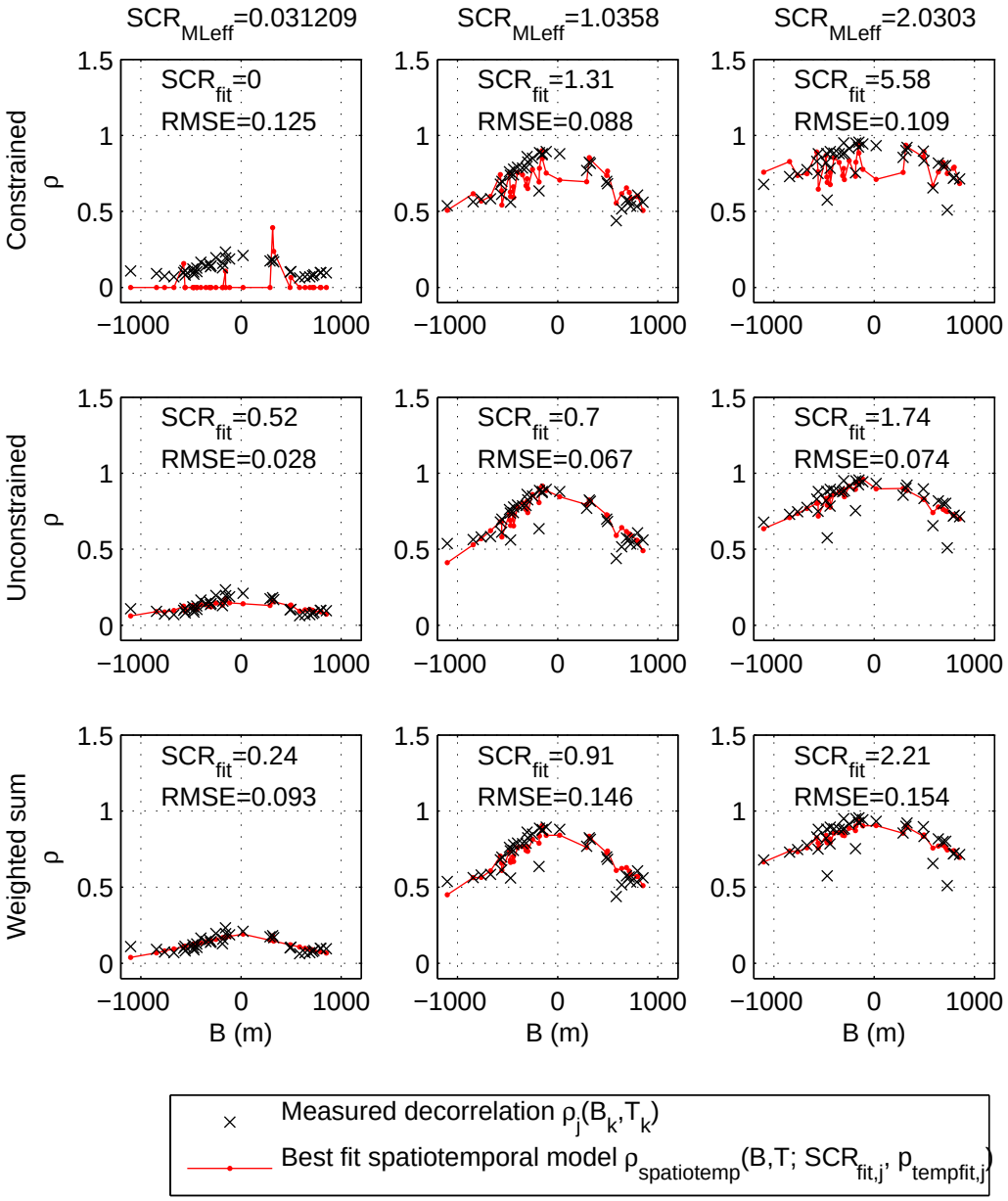

Figure 3.7: Decorrelation results by spatial baseline. Each plot displays the measured decorrelation points for the effective ML SCR listed at the top of the column, as well as the best fit spatiotemporal model for the temporal decorrelation model listed at the beginning of the row.

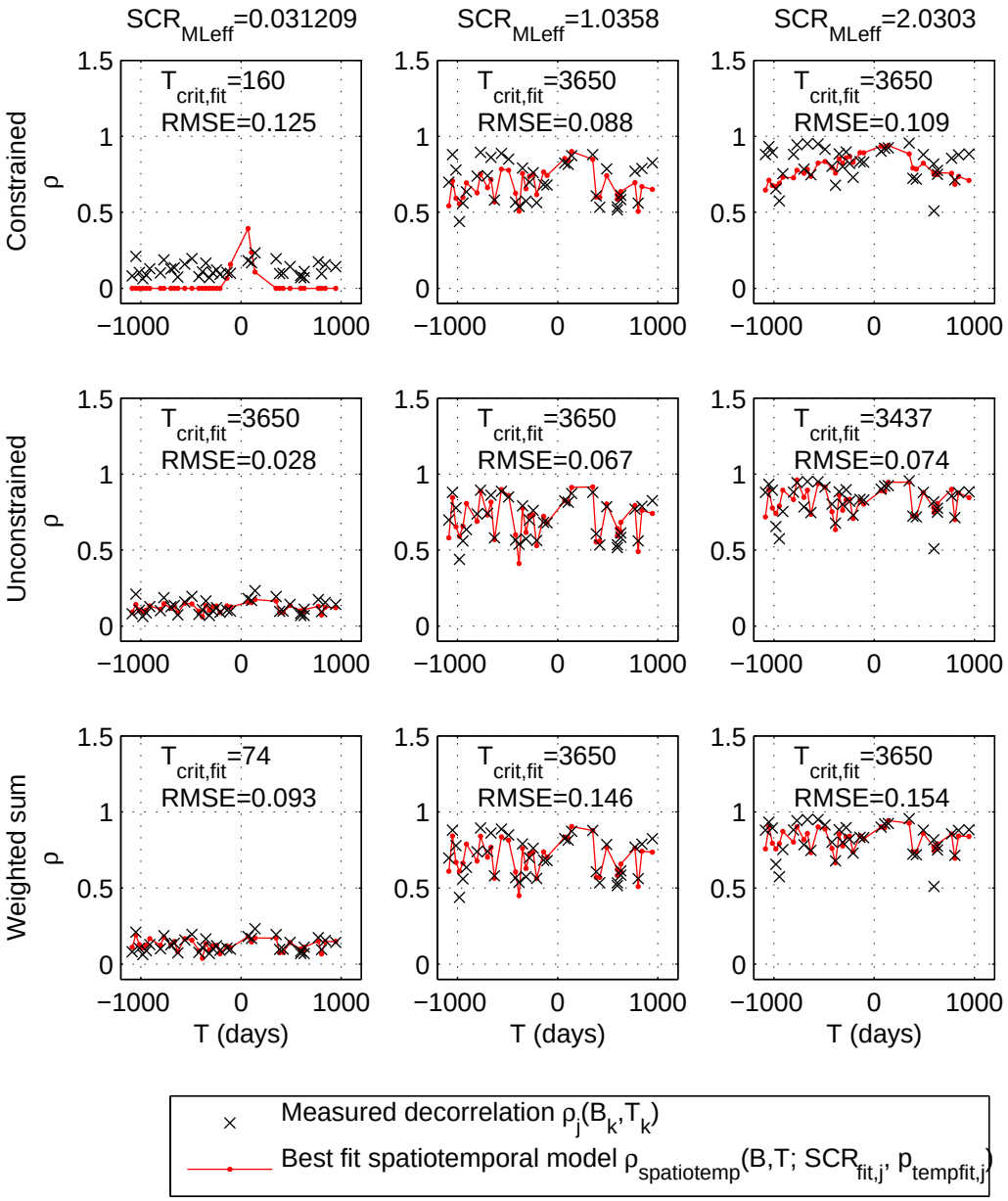

Figure 3.8: Decorrelation results by temporal baseline

There is more divergence at very high SCR (< 4), which may be due to estimating correlation values over very small pixel sets.

In Figure 3.9(b), we plot the best fit critical temporal baseline values for the temporal decorrelation models. We first examine the constrained and unconstrained linear models. Using the $T = 0$ constraint, the critical baseline increases from about 1000 days for near-zero $\mathrm{SCR}_{\mathrm{MLeff}}$ to 10 years (the maximum of our critical baseline parameter search space) for $\mathrm{SCR}_{\mathrm{MLeff}} \geq 0.4$. We expect the temporal critical baseline to increase with SCR; resolution elements containing strong dominant scatterers tend to be located in urban areas, which decorrelate more slowly than natural terrain.

The unconstrained temporal model for $\mathrm{SCR}_{\mathrm{MLeff}} < 0.4$ has the maximum critical baseline of 10 years, but the best fit correlation values ρ_0 are less than 1, as shown in Figure 3.9(c). As the effective estimated SCR increases, the best fit ρ_0 increases past 1. These values are physically infeasible and reflect the limitations of the model; the decorrelation function becomes piecewise linear, with no appreciable temporal decorrelation occurring until several weeks after the initial radar pass.

While the absolute critical baseline values for the constrained and unconstrained temporal models are larger than we might expect, this may be due to the limitations of these decorrelation models and their inability to accommodate different temporal decorrelation rates within the same resolution element. The weighted sum temporal model explicitly accounts for different decorrelation times in dominant and non-dominant scatterers. For this model, the critical temporal baseline applies to only the clutter scatterers, as the dominant scatterer is assumed to have zero temporal decorrelation; hence we expect the best fit critical baseline to be relatively uncorrelated with $\mathrm{SCR}_{\mathrm{MLeff}}$. This is in fact seen in the data in Figure 3.9(b), as the red data points corresponding to the weighted sum temporal model are generally uncorrelated with $\mathrm{SCR}_{\mathrm{MLeff}}$.

Finally, in Figure 3.9(d) we plot the optimal residual error values for all pixel sets. The linear unconstrained temporal model produces the best fit to the decorrelation points $\rho_j(B_k, T_k)$, with an average rms error of 0.068. The linear constrained model performs slightly worse, as we would expect given the additional model constraint. The weighted sum decorrelation function has the highest RMS error, suggesting that it does not accurately model temporal changes in the imaged area.

From Figures 3.7-3.8, we see that the unconstrained temporal decorrelation model produces a spatiotemporal fit with the lowest root mean square error across all SCR values. This suggests that multiple temporal decorrelation mechanisms that operate at different time scales should be modeled. The root mean square error associated with the weighted sum temporal decorrelation model is larger than the constrained, but the best fit SCR value is closer to the ML estimate.

The average discrepancy between $0 < \mathrm{SCR} < 1.1$ is less than 29% for both the constrained and unconstrained linear models.

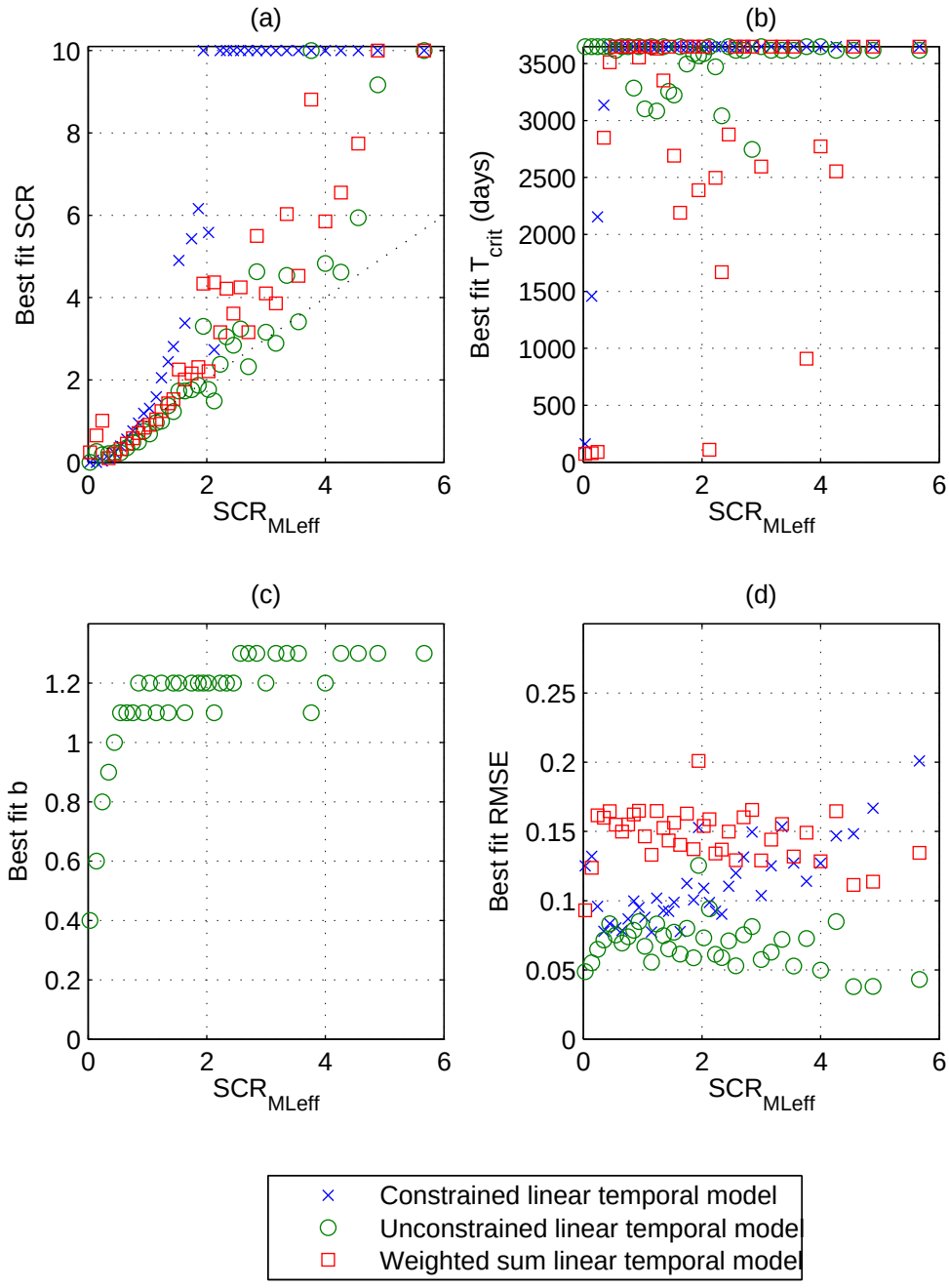

Figure 3.9: Best fit decorrelation model parameters

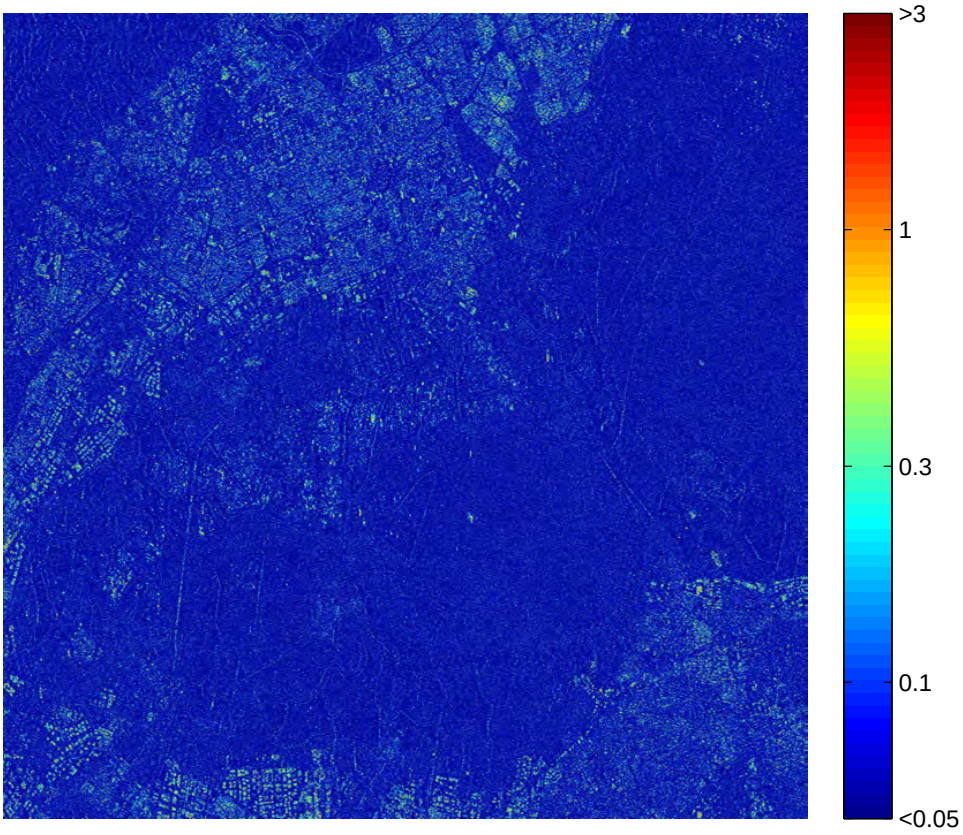

Figure 3.10: Maximum likelihood estimated SCR comparison

3.7 Discussion and conclusion

In this chapter, we have developed a quantitative theory for persistent scatterer spatial decorrelation derived from a statistical backscatter model. The resulting closed form expression, parameterized by signal-to-clutter ratio, quantifies the partial correlation of PS pixels over a large range of baselines. Using ERS interferometric data, we demonstrated that spatial decorrelation trends observed in actual InSAR data correspond well with our theory.

The decorrelation analysis presented here provides a theoretical framework to characterize partially correlated persistent scatterers. In the following chapters, we will use this framework to develop new PS identification, selection, and phase unwrapping algorithms. Quantifying the phase stability of PS pixels allows us to develop fundamental limits on the accuracy of PS techniques as a function of SCR-based selection thresholds.

Overall, ERS observations of decorrelation agree with our theoretically derived spatial decorrelation analysis. We find that correlation both decreases linearly as perpendicular baseline increases, and increases as a function of weights with SCR. Additional work is needed to improve the PS temporal decorrelation theory. For instance, we used a single temporal decorrelation model for all pixels in a set, regardless of terrain. If urban and natural terrain decorrelate at different rates, multiple models may be required to accurately capture the temporal decorrelation of a set. Unmodeled sources of decorrelation that might contribute to RMSE include thermal noise, orbital errors, and atmospheric phase that was not completely filtered out by the interferometric stack preprocessing.

In future work, the PS pixel backscatter model (Section 3.2) and subsequent analysis can be extended to accommodate more complex PS scattering behavior. For example, multiple dominant scatterers within a resolution cell [Ferretti et al., 2005] may be modeled by representing the backscatter spatial function $f(x, y)$ in Equation 3.1 as the sum of clutter backscatter $f_c(x, y)$ and dominant scatterer signal functions $f_{s,k}(x, y)$ for $k = 1, \ldots, N_s$:

$$f(x, y) = f_{s,1}(x, y) + f_{s,2}(x, y) + \ldots + f_{s,N_s}(x, y) + f_c(x, y). \tag{3.45}$$

In the simplest case, the location (x_k, y_k) and radar cross section $\sigma_{s,k}$ of each dominant scatterer k are known, and the reflectivity spatial functions $f_{s,k}(x, y)$ are mutually uncorrelated and uncorrelated with the clutter component $f_c(x, y)$. The backscatter autocorrelation function can then be

analytically evaluated as

$$\mathrm{E}[f(x,y)f^*(x',y')] = \begin{cases} \frac{\sigma_c}{R_x R_y} & \text{if } (x,y) = (x',y') \neq (x_k,y_k) \forall k \\ \sigma_{s,k} + \frac{\sigma_c}{R_x R_y} & \text{if } (x,y) = (x',y') = (x_k,y_k) \\ 0 & \text{if } (x,y) \neq (x',y') \end{cases} \tag{3.46}$$

$$= \frac{\sigma_c}{R_x R_y}\delta(x-x',y-y') + \sum_{k=1}^{N_s} \sigma_{s,k}\delta(x-x_k,y-y_k)\delta(x-x',y-y'). \tag{3.47}$$

The spatial decorrelation analysis in Section 3.3 can then be extended in a straight-forward manner.

A more realistic model may consider the locations of the dominant scatterers to be randomly distributed within the resolution cell according to some parametric spatial distribution (e.g. uniform or Poisson). Other potential PS models to investigate include spatially correlated clutter backscatter. We leave in depth statistical analysis of higher order PS scattering mechanisms to future work.

Chapter 4

Persistent scatterer models and derived statistics

4.1 Introduction

PS pixels are those in which the decorrelation phase term ϕ_{decorr} is small enough that the deformation signal ϕ_{def} can be reliably extracted. By identifying a network of PS pixels, deformation measurements on the order of millimeters may be obtained even in areas of low coherence, where conventional InSAR fails to produce useful observations [Colesanti et al., 2003a]. PS selection is highly dependent on accurate characterization of the pixel statistics. In Chapter 3, we quantified PS phase stability within single interferograms by deriving analytical expressions for spatial and temporal decorrelation ρ_{spatial} and ρ_{temporal} as a function of SCR and imaging baselines. In this chapter, we extend that analysis to a full statistical characterization of the decorrelation phase term ϕ_{decorr} across a stack of interferograms. This analysis will inform improved PS selection and deformation estimation techniques presented in Chapter 5.

Previous statistical decorrelation phase analysis has treated clutter as an additive white noise temporal process. This model leads to a characterization of ϕ_{decorr} as a white noise term that is lumped together with the noise phase term ϕ_{noise}. We will show that these assumptions result in over-simplified statistical characterization of the interferometric pixel stack distribution. A more accurate analytic distribution can be derived if the decorrelation and white noise terms are modeled and characterized independently, leading in term to better PS selection and techniques.

In this chapter, we present a more complete statistical characterization of the PS decorrelation phase statistics, derived from PS scattering principles. We first present a mathematical problem formulation in Section 4.2. In Section 4.3, we review previous interferometric phase distributions based on models of the PS SAR pixel. Next, we use a new PCPS backscattering model and multipass

interferometric system model in Section 4.4 to derive the joint phase-amplitude distribution for the entire stack of interferometric pixels as a function of SCR and spatial baseline. We discuss the fundamental differences in the PS models and quantitatively compare the resulting analytical distributions in Section 4.5. Finally, in Section 3.3.2, we show that the new PS backscatter model and resulting distribution fit simulated data better than previous analysis.

4.2 Problem formulation

We consider a stack of N_{sar} coregistered single look complex SAR images, indexed by $i \in \{0, \ldots, N_{sar}-1\}$. Without loss of generality, we consider SAR image $i = 0$ as the master and images $i = 1, \ldots, N_{sar} - 1$ as the slaves.

Let $u_i(\mathbf{x})$ represent the complex value of a pixel at coordinates $\mathbf{x}$ in SAR image i. The amplitude and phase of $u_i(\mathbf{x})$ are denoted by $r_i(\mathbf{x})$ and $\phi_i(\mathbf{x})$ respectively, i.e.

$$u_i(\mathbf{x}) = r_i(\mathbf{x})e^{j\phi_i(\mathbf{x})},\ i \in \{0, \ldots, N_{sar} - 1\}. \tag{4.1}$$

A stack of $N = N_{sar} - 1$ interferograms is formed by multiplying the master image $i = 0$ by the complex conjugate of each slave image $i \in \{1, \ldots, N_{sar} - 1\}$. Within each resulting interferogram, the interferometric pixel at coordinates $\mathbf{x}$ is given by

$$z_i(\mathbf{x}) = u_0(\mathbf{x})u_i^*(\mathbf{x}) \tag{4.2}$$

$$= r_{0i}(\mathbf{x})e^{j\phi_{0i}(\mathbf{x})},\ i \in \{1, \ldots, N\} \tag{4.3}$$

with amplitude $r_{0i}(\mathbf{x}) = r_0(\mathbf{x})r_i(\mathbf{x})$ and phase $\phi_{0i}(\mathbf{x}) = \phi_0(\mathbf{x}) - \phi_i(\mathbf{x})$.

Statistical characterization of the interferometric pixel stack $\{z_1(\mathbf{x}), \ldots, z_N(\mathbf{x})\}$ forms the fundamental basis for PS identification and selection techniques. Our objective in this chapter is to derive the probability distribution functions (PDFs) for the stack of interferometric amplitudes $\{r_{01}(\mathbf{x}), \ldots, r_{0N}(\mathbf{x})\}$ and phases $\{\phi_{01}(\mathbf{x}), \ldots, \phi_{0N}(\mathbf{x})\}$.

The interferometric pixel distributions are heavily dependent on the PS models from which they are derived. In the next section, we first review the existing PS models based on SAR pixel signal models, as well as the resulting interferometric pixel PDFs. We then summarize the limitations of these PS SAR pixel models. Next, we present a new, more generalized PCPS statistical analysis beginning from models of the physical backscattering mechanism and multipass interferometric system. These models, drawn from first principles, lead to a more complete joint statistical characterization of the interferometric PCPS amplitudes and phases as a function of SCR and imaging parameters.

For the remainder of this chapter, our analysis focuses on characterization of pixel $u_i(\mathbf{x})$ and $z_i(\mathbf{x})$ across imaging passes, i.e. as a function of i, rather than as a function of their coordinates $\mathbf{x}$ within each image. We therefore treat the pixel coordinates $\mathbf{x}$ as fixed and drop the variable from

notation for brevity when the context is clear.

We use the following notation for complex Gaussian distributions. A proper complex Gaussian random variable z with mean $\mathrm{E}[z] = \mu$, variance $\mathrm{E}[(z-\mu)(z-\mu)^*] = \sigma^2$, and pseudo-variance $\mathrm{E}[(z-\mu)^2] = 0$ is denoted $z \sim \mathcal{CN}(\mu, \sigma^2)$. A proper complex Gaussian random vector $\mathbf{z}$ with mean $\mathrm{E}[\mathbf{z}] = \mu$, covariance matrix $\mathrm{E}[\mathbf{z}\mathbf{z}^\dagger] = \Sigma$, and pseudo-covariance matrix $\mathrm{E}[\mathbf{z}\mathbf{z}^T] = \mathbf{0}$ is denoted $\mathbf{z} \sim \mathcal{CN}(\mu, \mathbf{\Sigma})$.

We denote the matrix of size $n \times m$ with all entries equal to 1 by $\mathbf{1}_{n\times m}$ and the analogous matrix with all entries equal to 0 by $\mathbf{0}_{n\times m}$. The identify matrix of size $n \times n$ is denoted by $\mathbf{I}_n$.

4.3 SAR pixel model and derived statistics

Existing PS analyses [Ferretti et al., 2001, Hooper, 2006, Shanker and Zebker, 2007] model PS pixels using signal properties of the SAR pixel values u_i over the acquisitions $i = 0, \ldots, N$. We call this PS model the *SAR pixel PS model*, in contrast to the *backscatter PS model* presented in Section 4.4.

In the SAR pixel PS model, each complex single look SAR pixel u_i is modeled as the sum of a constant signal component s and a clutter term c_i that varies with acquisition i:

$$u_i = s + c_i, \ i = 0, \ldots, N. \tag{4.4}$$

Statistical modeling of the signal component s of the SAR pixel has varied in prior work. In the following subsections, we review three possible models for s:

- a general, proper, complex Gaussian random variable (derived in Section 4.3.1)
- a zero-mean, circularly-symmetric, complex Gaussian random variable (used in [Just and Bamler, 1994, Shanker and Zebker, 2007], reviewed in Section 4.3.2)
- a deterministic variable (used in [Ferretti et al., 2001], reviewed in Section 4.3.3)

Note that for each of these cases, the value of s is assumed constant over the SAR pixel stack for $i = 0, \ldots, N$, regardless of whether it is considered random or deterministic but unknown.

In all cases, the clutter term c_i is modeled as a zero mean, circularly symmetric complex Gaussian white noise random process that is independent of the signal s:

$$c_i \sim \mathcal{CN}(0, \sigma_c^2), \text{ i.i.d. for } i = 0, \ldots, N. \tag{4.5}$$

The SAR pixel model thus fundamentally assumes that the PS clutter term is uncorrelated between SAR acquisitions, i.e. $\mathrm{E}[c_i c_j] = \mathrm{E}[c_i]\mathrm{E}[c_j] = 0$ for $i \neq j$, regardless of the spatial and temporal baselines between passes i and j.

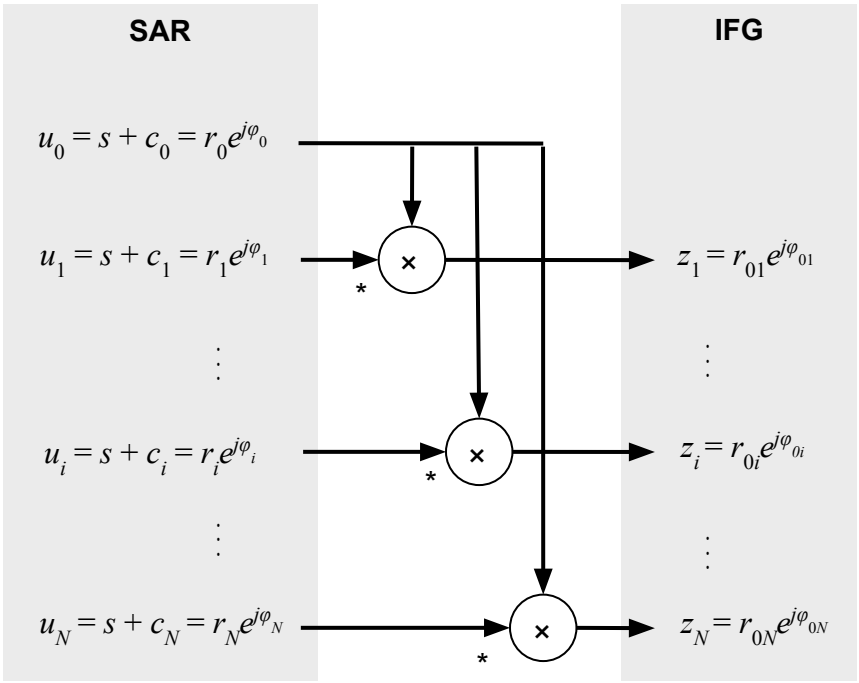

Figure 4.1: In the SAR pixel PS model, each complex single look SAR pixel u_i is modeled as the sum of a constant signal component s and a clutter term c_i that varies with acquisition i. The interferometric stack $z_1, \ldots, z_N$ is formed from a common master SAR image, as shown in the system block diagram above.

From the SAR pixel stack $\{u_0, \ldots, u_N\}$, the interferometric stack $\{z_1, \ldots, z_N\}$ is formed with common master acquisition $i = 0$. The block diagram for the system from input $\{u_0, \ldots, u_N\}$ to output $\{z_1, \ldots, z_N\}$ is shown in Figure 4.1.

The statistics of the interferometric pixels $\{z_1, \ldots, z_N\}$ depend on the model for the signal component s of the SAR pixel. In the following subsections, we derive the PDFs for the interferometric pixels for each model of s.

4.3.1 Proper complex Gaussian signal

We first examine the general case where the signal s is a proper, complex Gaussian random variable with complex mean μ and covariance $\mathrm{E}[(s-\mu)(s-\mu)^*] = \sigma_s^2$, i.e.

$$s \sim \mathcal{CN}(\mu, \sigma_s^2). \tag{4.6}$$

The clutter term c_i is specified by Equation 4.5, where s and c_i are mutually independent for all i. The signal s and clutter $\mathbf{c} = [c_0, \ldots, c_N]^T$ are therefore jointly Gaussian and form the proper

complex Gaussian random vector

$$\begin{bmatrix} s \\ \mathbf{c} \end{bmatrix} \sim \mathcal{CN}\left(\begin{bmatrix} \mu \\ \mathbf{0}_{(N+1)\times 1} \end{bmatrix}, \begin{bmatrix} \sigma_s^2 & \mathbf{0}_{1\times(N+1)} \\ \mathbf{0}_{1\times(N+1)} & \sigma_c^2 \mathbf{I}_{N+1} \end{bmatrix} \right) \tag{4.7}$$

The SAR pixel values are then a linear combination of uncorrelated, jointly Gaussian random variables, given by

$$\mathbf{u} = \begin{bmatrix} \mathbf{1}_{(N+1)\times 1} & \mathbf{I}_{N+1} \end{bmatrix} \begin{bmatrix} s \\ \mathbf{c} \end{bmatrix} \tag{4.8}$$

and distributed as

$$\mathbf{u} \sim \mathcal{CN}(\mu\mathbf{1}, \sigma_s^2\mathbf{1} + \sigma_c^2\mathbf{I}). \tag{4.9}$$

Equation 4.9 shows that unless the signal component is deterministic (i.e. the variance of s is 0), the SAR pixels in the stack are correlated. The expected SAR pixel power for this signal model is $\mathrm{E}[|u_i|^2] = |\mu|^2 + \sigma_s^2 + \sigma_c^2$.

The joint amplitude-phase distribution of the SAR complex values $\{u_0, \ldots, u_N\}$ is obtained by performing a change of variables $u_i = r_i e^{j\phi_i}$ for $i = 0, \ldots, N$, resulting in

$$\begin{aligned} f(r_0, \ldots, r_N, \phi_0, \ldots, \phi_N) = \frac{1}{(\pi\sigma^2)^{N+1}|\mathbf{\Gamma}|} \left(\prod_{i=0}^{N} r_i \right) \cdot \\ \exp\left(-\frac{1}{\sigma^2} \sum_{i=0}^{N} \sum_{j=0}^{N} (\mathbf{\Gamma}^{-1})_{ij} \left[r_i r_j \cos(\phi_i - \phi_j) + (r_i a_i + r_j a_j) + |\mu|^2 \right] \right), \end{aligned} \tag{4.10}$$

where $\sigma^2 = \sigma_s^2 + \sigma_c^2$, $a_i = \mathrm{Re}\{\mu\}\cos\phi_i + \mathrm{Im}\{\mu\}\sin\phi_i$, and the entries of the covariance matrix $\mathbf{\Gamma} \in \mathcal{R}^{(N+1)\times(N+1)}$ are given by

$$\mathbf{\Gamma}_{ij} = \begin{cases} 1, & i = j \\ \frac{\sigma_s^2}{\sigma_s^2 + \sigma_c^2}, & i \neq j. \end{cases} \tag{4.11}$$

For a single SAR image ($N = 0$), the joint amplitude-phase distribution simplifies to

$$f(r_i, \phi_i) = \frac{r_i}{\pi\sigma^2} \exp\left(-\frac{r_i^2 + 2r_i(\mathrm{Re}\{\mu\}\cos\phi_i + \mathrm{Im}\{\mu\}\sin\phi_i) + |\mu|^2}{\sigma^2} \right). \tag{4.12}$$

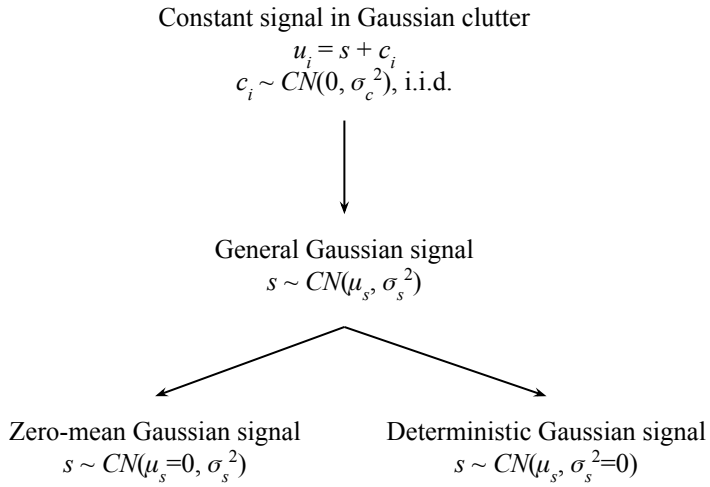

Figure 4.2: Statistical modeling of the signal component s for the PS SAR pixel model has varied in prior work. The signal models reviewed in this chapter are shown here in order of increasing specificity from top to bottom.

The marginal single SAR pixel amplitude and phase distributions are derived by integrating Equation 4.12 over ϕ_i and r_i respectively, producing

$$f(r_i) = \frac{2r_i}{\sigma^2} e^{-\frac{r_i^2+|\mu|^2}{\sigma^2}} I_0\left(\frac{2|\mu|}{\sigma^2} r_i\right) \tag{4.13}$$

$$f(\phi_i) = \frac{1}{\pi\sigma^2} e^{-\frac{(|\mu|^2-a_i)^2}{\sigma^2}} \left(\frac{\sigma^2}{2} e^{-\frac{a_i^2}{\sigma^2}} + \frac{a_i}{2}\sqrt{\pi\sigma^2}\left[1 - \text{erf}\left(-\sqrt{\frac{1}{\sigma^2}} a_i\right)\right]\right) \tag{4.14}$$

where $I_0(.)$ denotes the modified Bessel function and erf(.) denotes the error function.

For the general proper complex Gaussian signal model, the interferometric pixel amplitude and phase PDFs do not have closed forms. In the following subsections, we will examine two specific cases of the proper Gaussian signal model and derive the associated PDFs. Figure 4.2 shows how these cases relate to each other.

4.3.2 Circularly-symmetric Gaussian signal

By setting $\mu = 0$ in Equation 4.6, we model the SAR pixel signal component s as a circularly-symmetric (and by definition, zero-mean) complex Gaussian random variable. In classical radar

signal models, this distribution arises from a superposition of a large number of individual scatterers within the resolution cell, each with identically distributed backscatter amplitude and uniformly distributed phase. This model is therefore not physically valid for a single dominant scatterer in a PS cell. Regardless, we analyze the resulting PS distributions for completeness and due to the use of this signal model in prior work.

We compute the signal-to-clutter ratio for this model as

$$\mathrm{SCR} = \frac{\mathrm{E}[|s|^2]}{\mathrm{E}[|c|^2]} = \frac{\sigma_s^2}{\sigma_c^2}. \tag{4.15}$$

The single SAR amplitude-phase distribution in Equation 4.10 simplifies to

$$f(r_i, \phi_i) = \frac{r_i}{\pi\sigma^2} e^{-\frac{r_i^2}{\sigma^2}}, \tag{4.16}$$

showing that the pixel amplitude and phase are independent. The marginal SAR pixel amplitude is Rayleigh distributed, while the marginal phase is uniformly distributed over 2π:

$$f(r_i) = \frac{2r_i}{\sigma^2} e^{-\frac{r_i^2}{\sigma^2}} \tag{4.17}$$

$$f(\phi_i) = \frac{1}{2\pi}. \tag{4.18}$$

These distributions are plotted in Figure 4.3.

The single interferometric phase distribution is given by [Just and Bamler, 1994]

$$f(\phi_{0i}) = \frac{1}{2\pi} \frac{1-\rho^2}{1-(\rho\cos\phi_{0i})^2} \left[1 + \frac{\rho\cos\phi_{0i}}{\sqrt{1-(\rho\cos\phi_{0i})^2}} \arccos(-\rho\cos\phi_{0i})\right], \tag{4.19}$$

with correlation $\rho = \frac{\mathrm{SCR}}{1+\mathrm{SCR}}$. The marginal distributions are plotted in Figure 4.3 for varying values of SCR. Prior work utilizing this PS model [Shanker and Zebker, 2007] assumed that the interferometric phases $\{\phi_{01}, \ldots, \phi_{0N}\}$ are independent and identically distributed according to the marginal phase distribution in Equation 4.19.

In this work, we additionally derive the joint multipass amplitude-phase distributions over the full stack. For the circularly-symmetric Gaussian SAR pixel model, the SAR amplitude-phase distribution in Equation 4.10 simplifies to

$$f(r_0, \ldots, r_N, \phi_0, \ldots, \phi_N) = \frac{1}{(\pi\sigma^2)^{N+1}|\mathbf{\Gamma}|} \left(\prod_{i=0}^{N} r_i\right) \exp\left(-\frac{1}{\sigma^2} \sum_{i=0}^{N}\sum_{j=0}^{N} (\mathbf{\Gamma}^{-1})_{ij} r_i r_j \cos(\phi_i - \phi_j)\right) \tag{4.20}$$

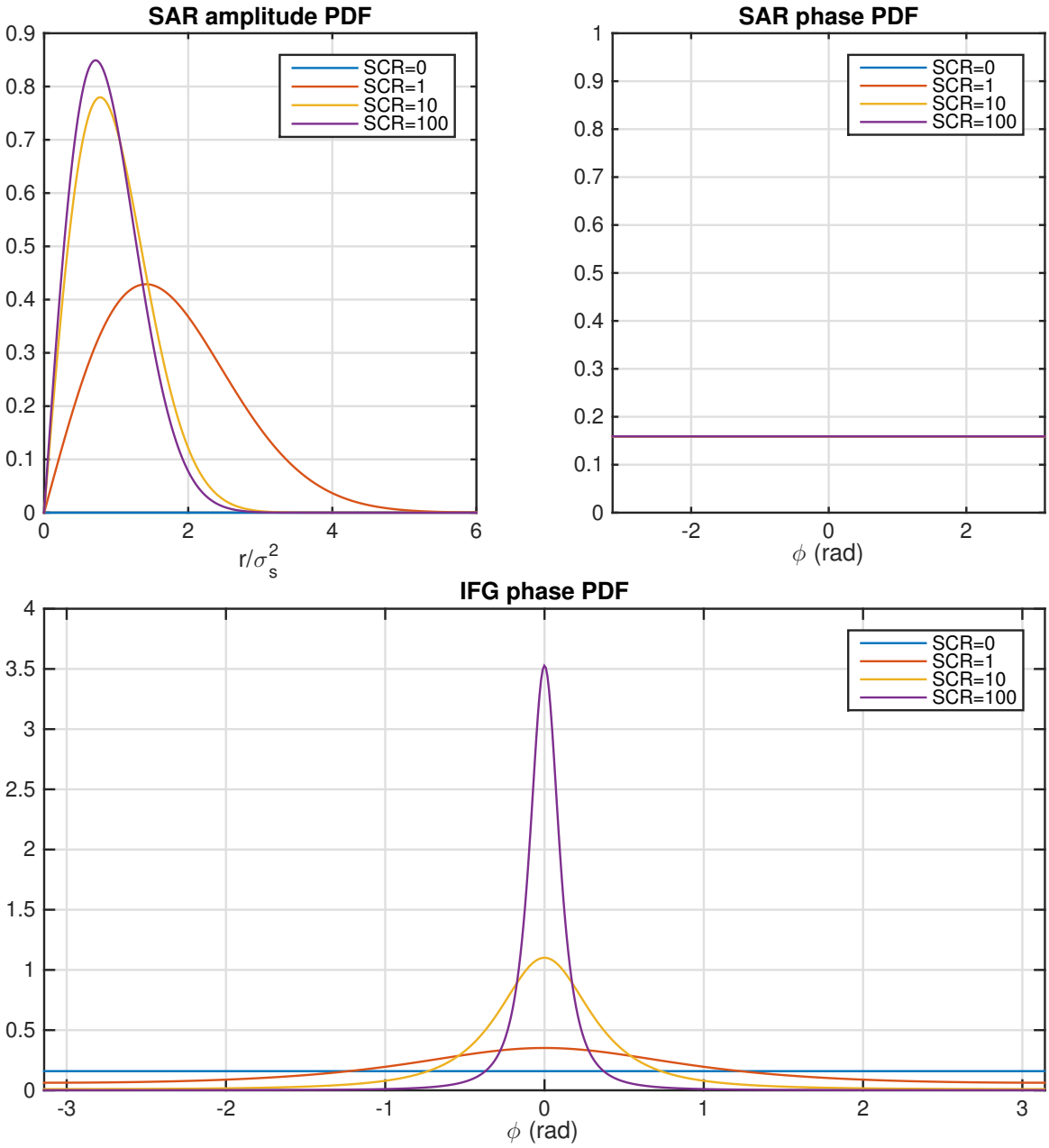

Figure 4.3: Marginal PDFs for the PS SAR pixel model with zero-mean Gaussian signal $s \sim \mathcal{CN}(0, \sigma_s^2)$, plotted for constant average total backscatter power $\sigma^2 = 1$. *Top left:* The distribution of the SAR pixel amplitude $r = |u|$, normalized by the average signal power σ_s^2. *Top right:* The SAR pixel phase is uniformly distributed, independent of SCR. *Bottom:* The interferometric phase is uniform over $[\pi, \pi]$ for a purely distributed scattering pixel with SCR $= 0$. As SCR increases, the interferometric phase distribution becomes increasingly concentrated about $\phi = 0$.

where the entries of the covariance matrix $\mathbf{\Gamma}$ are given by

$$\mathbf{\Gamma}_{ij} = \begin{cases} 1, & i = j \\ \frac{\mathrm{SCR}}{\mathrm{SCR}+1}, & i \neq j. \end{cases} \tag{4.21}$$

By performing the change of variables

$$\phi_{0i} = \phi_0 - \phi_i,\ i = 1, \ldots, N, \tag{4.22}$$

and integrating over ϕ_0, we obtain the joint multipass PDF of the interferometric phases and SAR amplitudes:

$$f(r_0, \ldots, r_N, \phi_{01}, \ldots, \phi_{0N}) = \frac{2\pi}{(\pi\sigma^2)^{N+1}|\mathbf{\Gamma}|} \left(\prod_{i=0}^{N} r_i \right) \exp\left(-\frac{1}{\sigma^2} \sum_{i=0}^{N} \sum_{j=0}^{N} (\mathbf{\Gamma}^{-1})_{ij} r_i r_j \alpha_{ij} \right) \tag{4.23}$$

where

$$\alpha_{ij} = \begin{cases} 1, & i = j \\ \cos(\phi_{0j}), & i = 0, j \neq 0 \\ \cos(\phi_{0i}), & i \neq 0, j = 0 \\ \cos(\phi_{0j} - \phi_{0i}), & \text{otherwise.} \end{cases} \tag{4.24}$$

Equations 4.21 and 4.23 show that in the circularly-symmetric Gaussian SAR pixel model, the interferometric pixel phases ϕ_{0i} and ϕ_{0j} are generally correlated for $i \neq j$, contrary to the assumptions of prior work.

4.3.3 Deterministic signal in Gaussian clutter

We now consider a SAR pixel PS model in which the SAR signal component s is a deterministic (but generally a priori unknown) value. We model this as a specific case of the complex Gaussian signal in Section 4.3.1 by setting the variance σ_s^2 equal to 0 in Equation 4.6; that is, s has the deterministic value μ. The signal-to-clutter ratio in this case is computed as

$$\mathrm{SCR} = \frac{\mathrm{E}[|s|^2]}{\mathrm{E}[|c|^2]} = \frac{|\mu|^2}{\sigma_c^2}. \tag{4.25}$$

Early work in PS techniques [Ferretti et al., 2001] utilized the SAR pixel deterministic signal model, though with numerically computed phase and amplitude statistics, rather than analytically derived.

The marginal SAR amplitude and phase distributions were previously computed for the case where $\mathrm{Im}\{\mu\} = 0$ (implying a loss of generality for the SAR distributions but not the interferometric

distributions) [Abramowitz and Stegun, 1972]. These distributions are respectively given by

$$f(r_i) = \frac{2r_i}{\sigma_c^2} I_0\left(\frac{2r_i}{\sigma_c^2}\right) e^{-\frac{1+r_i^2}{\sigma_c^2}}, \tag{4.26}$$

where $I_0(.)$ denotes the modified Bessel function, and

$$f(\phi_i) = \frac{1}{2\pi} e^{-\mathrm{SCR}\sin^2(\phi_i)}. \left(e^{-\mathrm{SCR}\cos^2(\phi_i)} + \sqrt{\pi \mathrm{SCR}}\cos(\phi_i)\left[1 - \mathrm{erf}\left(-\sqrt{\mathrm{SCR}}\cos(\phi_i)\right)\right]\right). \tag{4.27}$$

The interferometric distributions have no closed form, but the marginal amplitude and phase PDFs were numerically computed in [Agram, 2010]. The interferometric phase plot is duplicated in Figure 4.4 for varying values of SCR.

In addition to the previously published single image phase and amplitude distributions, we present a derivation for the multipass joint phase-amplitude distributions. The covariance matrix $\mathbf{\Gamma}$ in Equation 4.11 now simplifies to the identity matrix $\mathbf{I}$. The resulting joint SAR amplitude-phase distribution is given by

$$f(r_0, \ldots, r_N, \phi_0, \ldots, \phi_N) = \frac{1}{(\pi\sigma_c^2)^{N+1}} \left(\prod_{i=0}^{N} r_i\right) \cdot \exp\left(-\frac{1}{\sigma_c^2}\sum_{i=0}^{N}\sum_{j=0}^{N}\left[r_i r_j \cos(\phi_i - \phi_j) + (r_i a_i + r_j a_j) + |\mu|^2\right]\right) \tag{4.28}$$

where $a_i = \mathrm{Re}\{\mu\}\cos\phi_i + \mathrm{Im}\{\mu\}\sin\phi_i$.

4.3.4 Limitations of existing models

The SAR pixel PS model described in this section abstracts the complex SAR pixel u_i as the sum of a signal component s and a clutter component c_i. We presented three statistical models for the signal component s:

- a general, proper, complex Gaussian random variable (Section 4.3.1)
- a zero-mean, circularly-symmetric, complex Gaussian random variable (Section 4.3.2)
- a deterministic variable (Section 4.3.3)

In each case, the clutter c_i is modeled as an independent and identically distributed, circularly-symmetric, white Gaussian process.

The SAR pixel PS model is limited by several simplifying assumptions, summarized below:

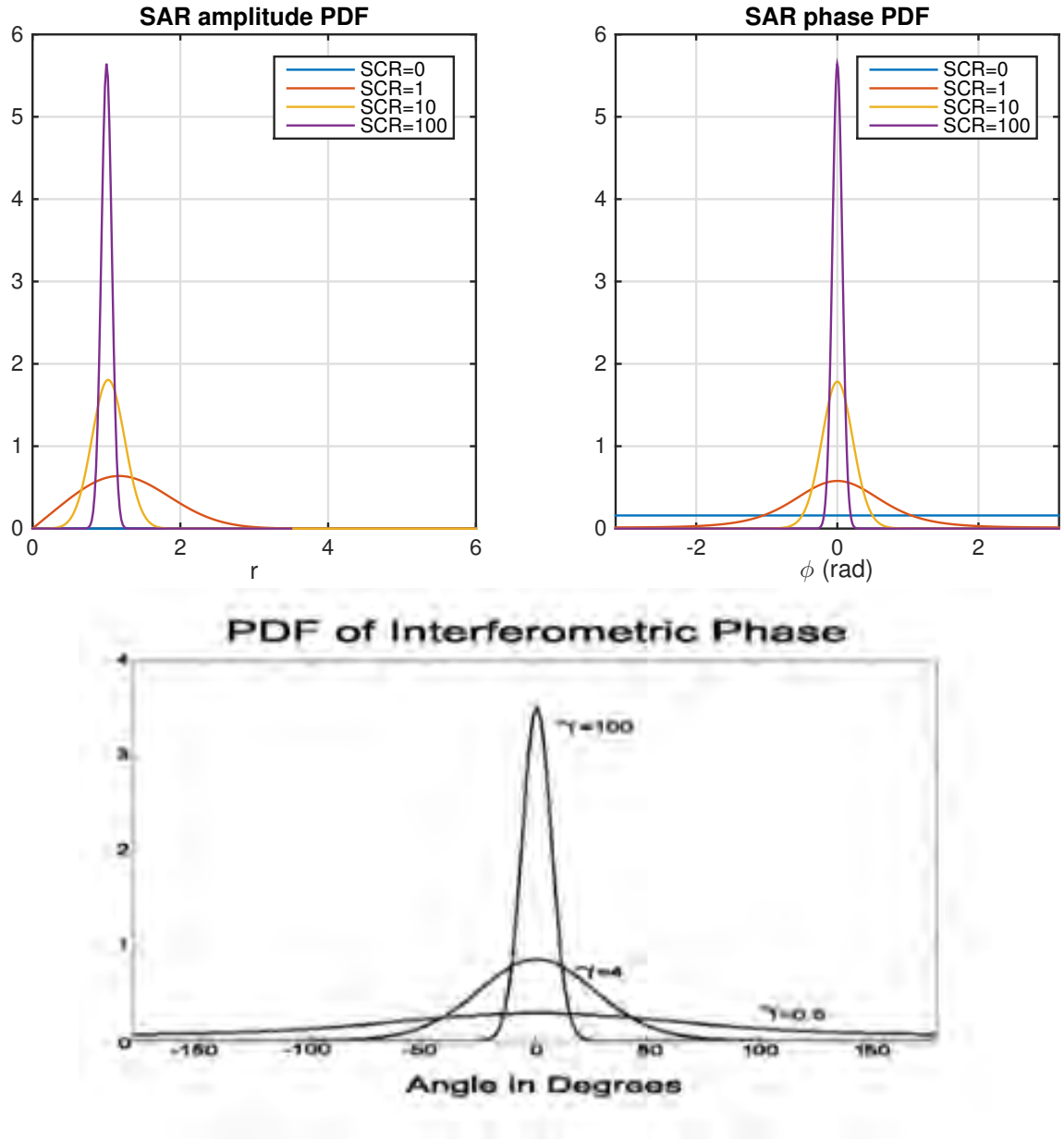

Figure 4.4: Marginal PDFs for the PS SAR pixel model with deterministic signal ($s \sim \mathcal{CN}(\mu, 0)$), plotted for constant signal power $\mu = 1$. *Top left:* The distribution of the SAR pixel amplitude $r = |u|$, normalized by the signal power $|\mu|^2$. *Top right:* The SAR pixel phase for a purely distributed scatterer (SCR $= 0$) is uniformly distributed over $[\pi, \pi]$. Unlike the complex Gaussian signal model, the SAR phase distribution for the constant signal model becomes tighter as SCR increases. *Bottom:* The interferometric phase is uniform over $[\pi, pi]$ for a purely distributed scattering pixel with SCR $=$ 0. As SCR increases, the interferometric phase distribution becomes increasingly concentrated about $\phi = 0$.

- The clutter component c_i is modeled as an additive white Gaussian noise process. Hence the PS model fundamentally assumes that c_i is uncorrelated between SAR acquisitions i and j, regardless of the spatial baseline B_{ij} and temporal baseline T_{ij} between passes. That is, the SAR pixel PS models assumes

$$\mathrm{E}[c_i c_j] = \mathrm{E}[c_i]\mathrm{E}[c_j] = 0 \text{ for } i \neq j. \tag{4.29}$$

- Because the statistical dependence of clutter on spatial and temporal baselines is not modeled, the resulting interferometric pixel and phase distributions also do not account for imaging system baselines. This SAR pixel model assumption is mathematically expressed as

$$f(u_0, \ldots, u_N | B_{01}, \ldots, B_{0N}, T_{01}, \ldots, T_{0N}) = f(u_0, \ldots, u_N), \tag{4.30}$$

$$f(z_1, \ldots, z_N | B_{01}, \ldots, B_{0N}, T_{01}, \ldots, T_{0N}) = f(z_1, \ldots, z_N), \tag{4.31}$$

$$f(\phi_{01}, \ldots, \phi_{0N} | B_{01}, \ldots, B_{0N}, T_{01}, \ldots, T_{0N}) = f(\phi_{01}, \ldots, \phi_{0N}). \tag{4.32}$$

- The interferometric pixel phases $\{\phi_{01}, \ldots, \phi_{0N}\}$ are modeled as independent and identically distributed according to the marginal PDF $f(\phi_{0i})$. The PS SAR pixel model thus assumes

$$f(\phi_{01}, \ldots, \phi_{0N}) = \prod_{i=1}^{N} f(\phi_{0i}). \tag{4.33}$$

In the next section, we present a more complete and accurate PS model and statistical characterization, derived from first principles of radar backscattering. This *PS backscatter model* models the reflectivity of individual scatterers contributing to clutter, in contrast to the *SAR pixel PS model*, which models their coherent sum. The new derivation removes the simplifying assumptions described in Equations 4.29-4.33 and quantitatively accounts for clutter correlation between acquisitions; effect of spatial and temporal baseline; and the joint distribution of all pixels in the multipass stack. This extended PS statistical characterization then leads to an improved analytical foundation for PS identification and selection in the following chapter.

4.4 PCPS multipass interferometric system model, backscatter model, and derived statistics

In this section, we derive the probabilistic distribution functions for the interferometric PCPS pixel values. Rather than using the abstracted SAR pixels signal models described in Section 4.3, our analysis is based on first principles for radar backscattering and imaging.

In Section 4.4.1, we present a new system model for multipass interferometric imaging, which

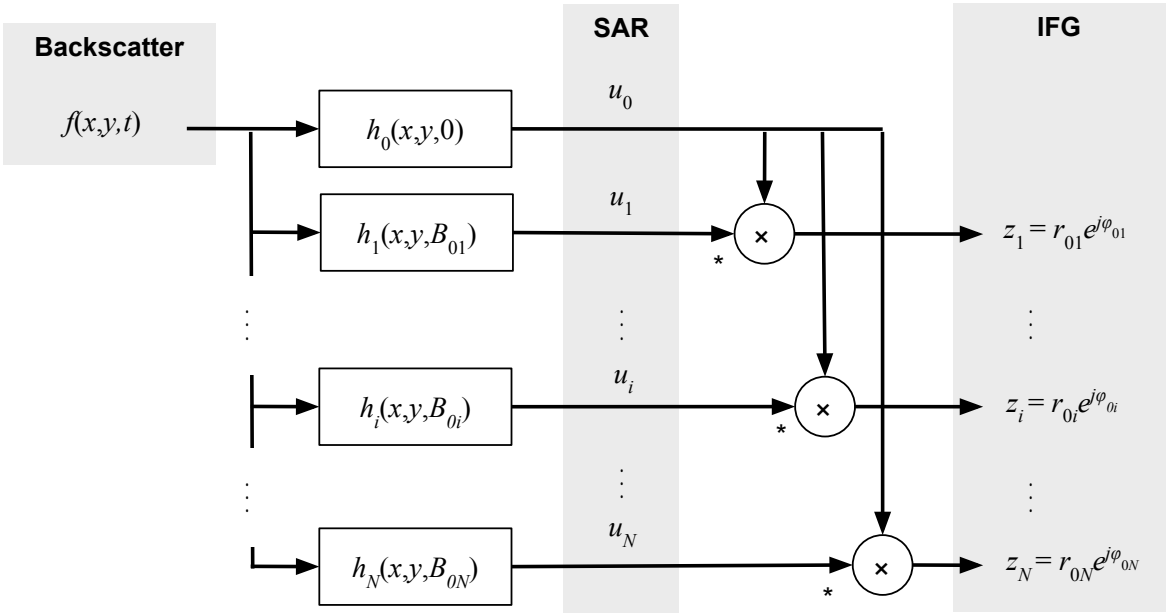

Figure 4.5: Multipass interferometric system block diagram

takes the surface backscatter function as input and outputs the stack of interferometric pixels. We then present a probabilistic backscattering function parameterized by SCR to model the PCPS resolution element in Section 4.4.2. Using this backscattering model as the input to the imaging system, we derive the statistical distribution of the resulting PCPS SAR pixels as a function of SCR and spatial baseline in Section 4.4.3. By starting from the backscattering model rather than an abstract signal model, we show that the correlation between SAR pixels is nonzero and can be analytically quantified. Finally, we show the distribution of the PCPS interferometric pixel stack.

4.4.1 Multipass interferometric system model

Rather than modeling each interferogram independently, our multipass interferometric system model considers all radar imaging passes jointly. Each pass i is characterized by its imaging impulse response $h_i(x, y, B_{0i})$, which is a function of azimuth x, range y, and perpendicular baseline B_{0i} with respect to the master pass $i = 0$.

Consider an imaging radar illuminating a ground resolution element. Let θ_0 be the incidence angle of the master image. Each single-look complex SAR image $i \in \{0, \ldots, N\}$ is produced by a radar pass with perpendicular baseline B_{0i} relative to the master image and incidence angle $\theta_i = \theta_0 + \delta\theta_i$,

with associated impulse response

$$h_i(x,y) = e^{-j\frac{4\pi}{\lambda}(r+y\sin\theta_i)}W(x,y). \tag{4.34}$$

where x and y denote the azimuth and range dimensions, r is the distance from the sensor to the center of the patch, λ is the radar wavelength, θ is the incidence angle, and $W(x,y)$ is the image processing impulse response due to range and azimuth compression. We use the typical imaging impulse response arising from compression of a linear frequency modulated chirp transmission,

$$W(x,y) = \text{sinc}(x/R_x)\text{sinc}(y/R_y) \tag{4.35}$$

where R_x and R_y denote the azimuth and range resolution, respectively.

The resulting single look complex SAR pixel u_i is given by the two-dimensional convolution of the imaging impulse response $h_i(x,y)$ with the surface backscatter function $f(x,y)$:

$$u_i = f(x,y,t_i) * h_i(x,y,B_{0i}) \tag{4.36}$$

$$= \int_x \int_y f(x,y,t_i)h_i(-x,-y)dxdy. \tag{4.37}$$

Using linear system matrix notation, we can represent the stack of SAR pixel values $\mathbf{u} = [u_0,\ldots,u_N]^T$ as the output of linear system $\mathbf{H}$:

$$\mathbf{u} = \begin{bmatrix} u_0 \\ \vdots \\ u_N \end{bmatrix} = \mathbf{Hf} \tag{4.38}$$

where each row $i \in \{0,\ldots,N\}$ of the matrix $\mathbf{H}$ is formed from the imaging impulse response $h_i(x,y)$ and the input $\mathbf{f}$ is formed from the surface backscatter function $f(x,y)$, i.e.

$$\mathbf{H} = \begin{bmatrix} -h_0(x,y)- \\ \vdots \\ -h_N(x,y)- \end{bmatrix} \tag{4.39}$$

$$\mathbf{f} = \begin{bmatrix} | \\ f(x,y) \\ | \end{bmatrix}. \tag{4.40}$$

Note that though we use matrix notation for simplicity, the input $f(x,y)$ and impulse responses $h_i(x,y)$ are continuous functions of the spatial variables x and y. We temporarily ignore temporal

changes in the backscatter function and bring them into the analysis at a later stage.

The interferometric pixels are formed as

$$z_i = u_0 u_i^*, \ i = 1, \ldots, N. \tag{4.41}$$

We represent the stack of coregistered interferometric pixels by the vector

$$\mathbf{z} = \begin{bmatrix} z_1 \\ \vdots \\ z_N \end{bmatrix} = \begin{bmatrix} r_{01} e^{j\phi_{01}} \\ \vdots \\ r_{0N} e^{j\phi_{0N}} \end{bmatrix}. \tag{4.42}$$

The full system diagram from backscatter function to interferometric stack is shown in Figure 4.5.

4.4.2 PCPS backscatter model

We model the PS pixel resulting from a ground resolution element of size R_x in azimuth and R_y in range, shown in Figure 4.6. Let σ_s^2 represent the average backscatter power of the dominant scatterer and σ_c^2 represent the total average backscatter power due to clutter. The signal-to-clutter ratio of the pixel is defined as

$$\text{SCR} \equiv \frac{\sigma_s^2}{\sigma_c^2}. \tag{4.43}$$

We model the surface backscatter function $f(x, y, t)$ as a random white, circularly symmetric complex Gaussian spatial function distributed as

$$f(x, y, t) \sim \begin{cases} \mathcal{CN}(0, \sigma_s^2 + \frac{\sigma_c^2}{R_x R_y}), & x = x_{\text{dom}}, y = y_{\text{dom}} \\ \mathcal{CN}(0, \frac{\sigma_c^2}{R_x R_y}), & \text{otherwise} \end{cases} \tag{4.44}$$

where $(x_{\text{dom}}, y_{\text{dom}})$ denote the distance in range and azimuth of the dominant scatterer from the center of the resel.

The vector $\mathbf{f}$ representing the backscatter function is then described by a circularly symmetric

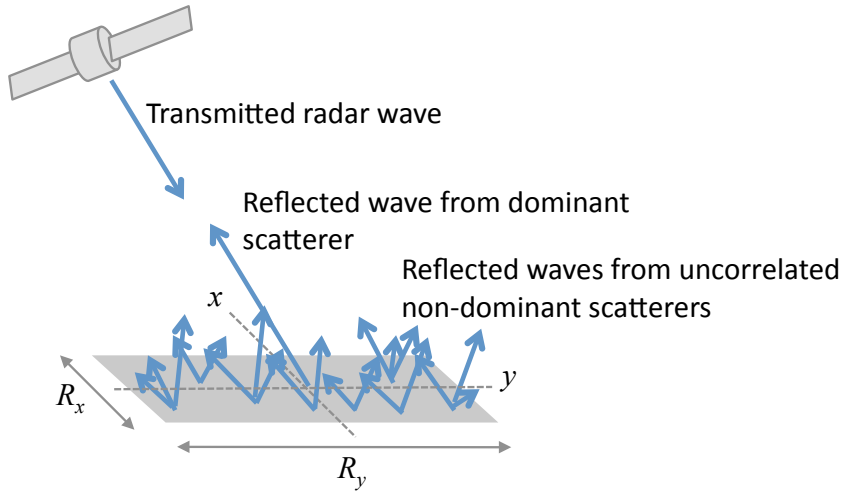

Figure 4.6: PS backscatter mechanism. The resolution element is composed of a centered dominant scatterer surrounded by uncorrelated, uniformly distributed scatterers contributing to clutter.

complex Gaussian random vector with mean $\mu = \mathbf{0}$ and covariance matrix

$$\boldsymbol{\Sigma}_{\mathbf{f}} = \mathrm{E}[\mathbf{f}\mathbf{f}^{\dagger}] \tag{4.45}$$

$$= \frac{\sigma_c^2}{R_x R_y}\mathbf{I} + \sigma_s^2 \begin{bmatrix} 0 & 0 & \dots & & 0 \\ 0 & \ddots & & & \\ \vdots & & 1 & & \\ & & & \ddots & \\ 0 & & & & 0 \end{bmatrix} \tag{4.46}$$

where $\mathbf{I}$ is the identify matrix and $\mathbf{f}^{\dagger}$ denotes the complex conjugate of the transpose of $\mathbf{f}$. The nonzero entry of the right-most matrix in Equation 4.46 occurs in the position corresponding to $(x_{\mathrm{dom}}, y_{\mathrm{dom}})$.

We note that the interferometric system model is independent from the specific form of the input backscatter model $f(x, y, t)$. As such, the system model is not limited to PS analysis and may be used for other forms of $f(x, y, t)$ beyond that specified in Equation 4.44.

4.4.3 Derived statistics

Given the probabilistic distribution of the backscatter function $f(x, y)$, we derive the statistics of the SAR pixel stack $\mathbf{u}$ from the linear relation $\mathbf{u} = \mathbf{Hf}$. Since $\mathbf{f}$ is a circularly symmetric Gaussian random vector $\mathbf{f} \sim \mathcal{CN}(\mathbf{0}, \mathbf{\Sigma_f})$, the random vector $\mathbf{u}$ is also circularly symmetric and Gaussian, distributed as $\mathbf{u} \sim \mathcal{CN}(\mathbf{0}, \mathbf{H\Sigma_f H}^\dagger)$ where $\mathbf{H}^\dagger$ is the Hermitian transpose of $\mathbf{H}$.

Covariance of u

For $\mathbf{\Sigma_f}$ in Equation 4.46, the covariance of $\mathbf{u}$ is given by

$$\text{cov}(\mathbf{u}) = \mathbf{H\Sigma_f H}^\dagger \tag{4.47}$$

$$= \frac{\sigma_c^2}{R_x R_y}\mathbf{HIH}^\dagger + \sigma_s^2\mathbf{H}\begin{bmatrix} 0 & 0 & \dots & & 0 \\ 0 & \ddots & & & \\ \vdots & & 1 & & \\ & & & \ddots & \\ 0 & & & & 0 \end{bmatrix}\mathbf{H}^\dagger \tag{4.48}$$

$$= \frac{\sigma_c^2}{R_x R_y}\mathbf{HH}^\dagger + \sigma_s^2\mathbf{h}(x_{dom}, y_{dom})\mathbf{h}^\dagger(x_{dom}, y_{dom}) \tag{4.49}$$

where $\mathbf{h}(x_{dom}, y_{dom}) = [h_0(x_{dom}, y_{dom}), \dots, h_N(x_{dom}, y_{dom})]^T$.

Each entry of the matrix $\mathbf{HH}^\dagger$ is given by

$$[\mathbf{HH}^\dagger]_{ij} = \int\int h_i(x, y)h_j^*(x, y)dxdy \tag{4.50}$$

$$= \int\int e^{-j\frac{4\pi}{\lambda}y(\sin\theta_i - \sin\theta_j)}|W(x, y)|^2 dxdy \tag{4.51}$$

$$= \int\int e^{-j\frac{4\pi}{\lambda}y(\sin\theta_i - \sin\theta_j)}\text{sinc}^2(x/R_x)\text{sinc}^2(y/R_y)dxdy \tag{4.52}$$

$$= R_x\int e^{-j\frac{4\pi}{\lambda}y(\sin\theta_i - \sin\theta_j)}\text{sinc}^2(y/R_y)dy \tag{4.53}$$

$$= R_x R_y\left(1 - \frac{2R_y\cos\theta|B_{ij}|}{\lambda r}\right)\mathcal{I}\{|B_{ij}| < B_{\text{crit}}\} \tag{4.54}$$

where $\mathcal{I}\{.\}$ is the indicator function that evaluates to 1 when the argument is true and 0 otherwise.

In the case where the dominant scatterer is located at the phase center of the pixel,

$$(x_{dom}, y_{dom}) = (0, 0). \tag{4.55}$$

The entries of the outer product $\mathbf{h}(x_{dom}, y_{dom})\mathbf{h}^{\dagger}(x_{dom}, y_{dom})$ then evaluate to

$$[\mathbf{h}(x_{dom}, y_{dom})\mathbf{h}^{\dagger}(x_{dom}, y_{dom})]_{ij} = h_i(0,0)h_j^*(0,0) \tag{4.56}$$

$$= 1 \text{ for } i, j \in \{0, \ldots, N\}. \tag{4.57}$$

In the rest of the analysis, we assume that the image is resampled such that Equation 4.55 holds. In general, if this is not the case, Equation 4.56 evaluates to less than unity, quantifying the loss of coherence due to offset dominant scatterer.

Substituting Equations 4.54 and 4.57 into Equation 4.49 leads to

$$\text{cov}(\mathbf{u}) = \mathbf{H}\boldsymbol{\Sigma}_{\mathbf{f}}\mathbf{H}^{\dagger} = \sigma^2\boldsymbol{\Gamma} \tag{4.58}$$

where $\sigma^2 = \sigma_s^2 + \sigma_c^2$, and the entries of the matrix $\boldsymbol{\Gamma}$ are given by

$$\boldsymbol{\Gamma}_{ij} = \frac{1}{1+\text{SCR}}\left(1 - \frac{2R_y \cos\theta |B_{ij}|}{\lambda r}\right)\mathcal{I}\{|B_{ij}| < B_{\text{crit}}\} + \frac{\text{SCR}}{1+\text{SCR}}. \tag{4.59}$$

The right-hand side of Equation 4.59 is equal to the analytical PCPS spatial decorrelation between SAR acquisitions i and j as a function of the spatial baseline B_{ij} and SCR, as derived in Chapter 3, Equation 3.13. Thus each entry of the covariance matrix $\text{cov}(\mathbf{u})$ is given by $\sigma^2\boldsymbol{\Gamma}_{ij}$, where

$$\boldsymbol{\Gamma}_{ij} = \rho_{\text{spatial}}(B_{ij}, \text{SCR}). \tag{4.60}$$

We generalize this covariance matrix result by incorporating temporal decorrelation, setting each entry $\boldsymbol{\Gamma}_{ij}$ equal to the total spatiotemporal decorrelation between SAR acquisitions i and j:

$$\boldsymbol{\Gamma}_{ij} = \rho(B_{ij}, T_{ij}, \text{SCR}). \tag{4.61}$$

The analytical derivation for this generalization is left for future work.

As discussed in Chapter 3, the total spatiotemporal decorrelation can be decomposed into its spatial and temporal decorrelation components:

$$\boldsymbol{\Gamma}_{ij} = \rho_{\text{spatial}}(B_{ij}, \text{SCR}) \cdot \rho_{\text{temporal}}(T_{ij}, \text{SCR}). \tag{4.62}$$

The spatial correlation component, parameterized by SCR, has the analytical form

$$\rho_{\text{spatial}}(B_{ij}; \text{SCR}) = \begin{cases} \frac{1}{1+\text{SCR}}\left(1 - \frac{2R_y \cos\theta |B_{ij}|}{\lambda r}\right) + \frac{\text{SCR}}{1+\text{SCR}}, & |B_{ij}| < B_{\text{crit}} \\ \frac{\text{SCR}}{1+\text{SCR}}, & |B_{ij}| \geq B_{\text{crit}}, \end{cases} \tag{4.63}$$

where the critical baseline B_{crit} is given by

$$B_{\text{crit}} = \frac{\lambda r}{2R_y \cos\theta}. \tag{4.64}$$

For the temporal component ρ_{temporal}, we use an empirical linearly decorrelating model [Zebker and Villasenor, 1992] parameterized by the critical temporal baseline T_{crit}:

$$\rho_{\text{temporal}}(T_{ij}; T_{\text{crit}}) = \begin{cases} 1 - \frac{|T_{ij}|}{T_{\text{crit}}}, & |T_{ij}| < T_{\text{crit}} \\ 0, & |T_{ij}| \geq T_{\text{crit}}. \end{cases} \tag{4.65}$$

The full covariance matrix of $\mathbf{u}$ thus takes the form

$$\text{cov}(\mathbf{u}) = \sigma^2 \mathbf{\Gamma}(\text{SCR}, \mathbf{B}, \mathbf{T}), \tag{4.66}$$

where

$$\mathbf{\Gamma}(\text{SCR}, \mathbf{B}, \mathbf{T}) = \begin{bmatrix} 1 & \rho(B_{01}, T_{01}, \text{SCR}) & \rho(B_{02}, T_{02}, \text{SCR}) & \dots & \rho(B_{0N}, T_{0N}, \text{SCR}) \\ \rho(B_{01}, T_{01}, \text{SCR}) & 1 & \rho(B_{12}, T_{12}, \text{SCR}) & & \\ \rho(B_{02}, T_{02}, \text{SCR}) & \rho(B_{12}, T_{12}, \text{SCR}) & 1 & & \\ \vdots & & & \ddots & \\ \rho(B_{0N}, T_{0N}, \text{SCR}) & & & & 1 \end{bmatrix} \tag{4.67}$$

and $\mathbf{B}$ and $\mathbf{T}$ denote the sets of spatial and temporal baselines between every pair of acquisitions in the stack.

Multipass joint phase-amplitude PDF

From the joint SAR pixel distribution

$$\mathbf{u} \sim \mathcal{CN}\left(\mathbf{0}, \sigma^2 \mathbf{\Gamma}(\text{SCR}, \mathbf{B}, \mathbf{T})\right), \tag{4.68}$$

we perform a change of variables $u_i = r_i e^{j\phi_i}$ for $i = 0, \dots, N$ to obtain the joint SAR amplitude-phase distribution

$$f(r_0, \dots, r_N, \phi_0, \dots, \phi_N) = \frac{1}{(\pi\sigma^2)^{N+1}|\mathbf{\Gamma}|} \left(\prod_{i=0}^{N} r_i\right) \exp\left[-\frac{1}{\sigma^2} \sum_{i=0}^{N} \sum_{j=0}^{N} (\mathbf{\Gamma}^{-1})_{ij} \cos(\phi_j - \phi_i) r_i r_j\right], \tag{4.69}$$

where $\mathbf{\Gamma} = \mathbf{\Gamma}(\text{SCR}, \mathbf{B}, \mathbf{T})$ is the generalized covariance matrix discussed above.

Without loss of generality, we let index $i = 0$ represent the master SAR image. Interferogram pixels are then given by $z_i = u_0 u_i^*$. To convert the SAR phases to interferometric phases, we use the following change of variables:

$$\phi_{0i} = \phi_0 - \phi_i \text{ for } i = 1, \ldots, N \tag{4.70}$$

and then integrate over ϕ_0. We thus arrive at the joint PDF for the multipass SAR amplitudes and interferometric phases:

$$f(r_0, \ldots, r_N, \phi_{01}, \ldots, \phi_{0N}) = \frac{2\pi}{(\pi\sigma^2)^{N+1}|\mathbf{\Gamma}|} \left(\prod_{i=0}^{N} r_i \right) \exp\left[-\frac{1}{\sigma^2} \sum_{i=0}^{N} \sum_{j=0}^{N} (\mathbf{\Gamma}^{-1})_{ij} \alpha_{ij} r_i r_j \right], \tag{4.71}$$

where

$$\alpha_{ij} = \begin{cases} 1, & i = j = 0 \\ \cos(\phi_{0j}), & i = 0, j \neq 0 \\ \cos(\phi_{0i}), & i \neq 0, j = 0 \\ \cos(\phi_{0j} - \phi_{0i}), & i \neq 0, j \neq 0 \end{cases} \tag{4.72}$$

and $\mathbf{\Gamma} = \mathbf{\Gamma}(\text{SCR}, \mathbf{B}, \mathbf{T})$.[1]

Equation 4.71 expresses the analytical joint distribution of the PCPS amplitudes and interferometric phases over the full stack of acquisitions. The entries of the covariance matrix $\mathbf{\Gamma}(\text{SCR}, \mathbf{B}, \mathbf{T})$ are given by the analytical spatiotemporal decorrelation between each pair of acqusitions i and j and vary as a function of SCR, the spatial baseline B_{ij}, and the temporal baseline T_{ij}. The model thus accounts for the effect of the physical imaging parameters on the distribution of interferometric observations.

For deeper insight and intuition into the $(2N + 1)$-dimensional joint phase-amplitude PDF, we

[1] From Equation 4.71, it is possible to further derive the joint PDF for the interferometric phases and amplitudes using the change of variables

$$r_{0i} = r_0 r_i \text{ for } i = 0, \ldots, N, \tag{4.73}$$

with associated Jacobian $\prod_{i=0}^{N} r_i$. The resulting PDF is then

$$f(r_{00}, \ldots, r_{0N}, \phi_{01}, \ldots, \phi_{0N}) = \frac{2\pi}{(\pi\sigma^2)^{N+1}|\mathbf{\Gamma}|} \left(\frac{\prod_{k=1}^{N} r_{0k}}{r_{00}^N} \right) \exp\left[-\frac{1}{\sigma^2} \sum_{i=0}^{N} \sum_{j=0}^{N} (\mathbf{\Gamma}^{-1})_{ij} \alpha_{ij} \frac{r_{0i} r_{0j}}{r_{00}} \right], \tag{4.74}$$

where α_{ij} is given by Equation 4.72.

The interferometric phase-interferometric amplitude PDF $f(r_{00}, \ldots, r_{0N}, \phi_{01}, \ldots, \phi_{0N})$ contains the same information as the interferometric phase-SAR amplitude PDF $f(r_0, \ldots, r_N, \phi_{01}, \ldots, \phi_{0N})$, but is more unwieldy for algorithmic use due to the extra operations. Hence for all practical purposes, we will use the PDF form given in Equation 4.71.

compute and plot Equation 4.71 and several derived distributions for a stack of two interferograms (i.e. $N = 2$). We set the simulated radar parameter values to those typical for a C-band system: $\lambda = 0.0566$ m, $\theta = 23.3°$, $R_x = 6.5$ m, $R_y = 24.3$ m, $B_{\text{crit}} = 1052$ m. Only spatial decorrelation is modeled, with no temporal decorrelation contribution. We numerically integrate the joint PDF to compute various lower-dimensional marginalizations of joint phase-amplitude PDF, detailed below.

$f(\phi_{01}, \phi_{02})$: In Figure 4.7, the joint phase PDF $f(\phi_{01}, \phi_{02})$ is plotted for varying values of SCR and varying baseline pairs. We first note that the PDF is not symmetric for the two interferograms; the spread is much greater in the dimension associated with the larger baseline. Moreover, the decorrelation phase terms are not independent across interferograms, as $f(\phi_{02}|\phi_{01}) \neq f(\phi_{02})$. The first row of the figure shows that as the SCR of the pixel increases, the PDF becomes tighter around $(\phi_{01}, \phi_{02}) = (0, 0)$. This is expected; as the PS pixel approaches an ideal point target, the variation in the phase decreases.

In the second row of the figure, we show the variation in the joint phase PDF as a function of the imaging spatial baselines. As the baseline B_{0i} for one interferogram increases toward the critical baseline, the standard deviation of the PDF in the corresponding dimension increases. Convergence in the PDF is reached when $B_{0i} = B_{\text{crit}}$. The angles of the semi-major and semi-minor axes of the PDF depend on the relative baselines between the interferograms.

Finally, we note that the joint PDF diverges when the two spatial baselines are equal. Because only spatial decorrelation is modeled, the rows of the covariance matrix $\mathbf{\Gamma}$ corresponding to exact repeat orbits will be identical. The covariance matrix is then singular and non-invertible, resulting in a divergent PDF.

$f(\phi_{01}, \phi_{02} \mid r)$: Figure 4.8 shows the probabilistic distribution of (ϕ_{01}, ϕ_{02}), given knowledge of interferometric amplitude r_{01} or r_{02}. The SCR and spatial baselines are fixed at SCR = 1, $B_{01} = 200$ m, and $B_{02} = 1200$ m. In the first row, the phase distribution is plotted for varying values of r_{01}, the amplitude associated with the smaller baseline. The second row illustrates the variation in the phase distribution as a function of known r_{02}, the amplitude associated with the larger baseline.

It is immediately obvious that amplitude and phase are not independent; the distribution of both phases is tightly coupled with the amplitude of either. As the known amplitude increases, the phase distribution converges about the origin. We see that r_{02} provides more information about the phase distribution; the PDF is tighter for $f(\phi_{01}, \phi_{02}) \mid r_{02})$ than for $f(\phi_{01}, \phi_{02}) \mid r_{01})$ at equal values of r_{01} and r_{02}. Intuitively, this makes sense; a larger spatial baseline corresponds to greater spatial decorrelation and hence more uncertainty than a smaller spatial baseline. Therefore, knowledge of large baseline interferometric values provides more information.

$f(r_{01}, r_{02})$: In Figure 4.9, the joint amplitude PDF $f(r_{01}, r_{02})$ is plotted for varying values of SCR and spatial baseline values. The first row of the figure shows that the amplitude PDF converges

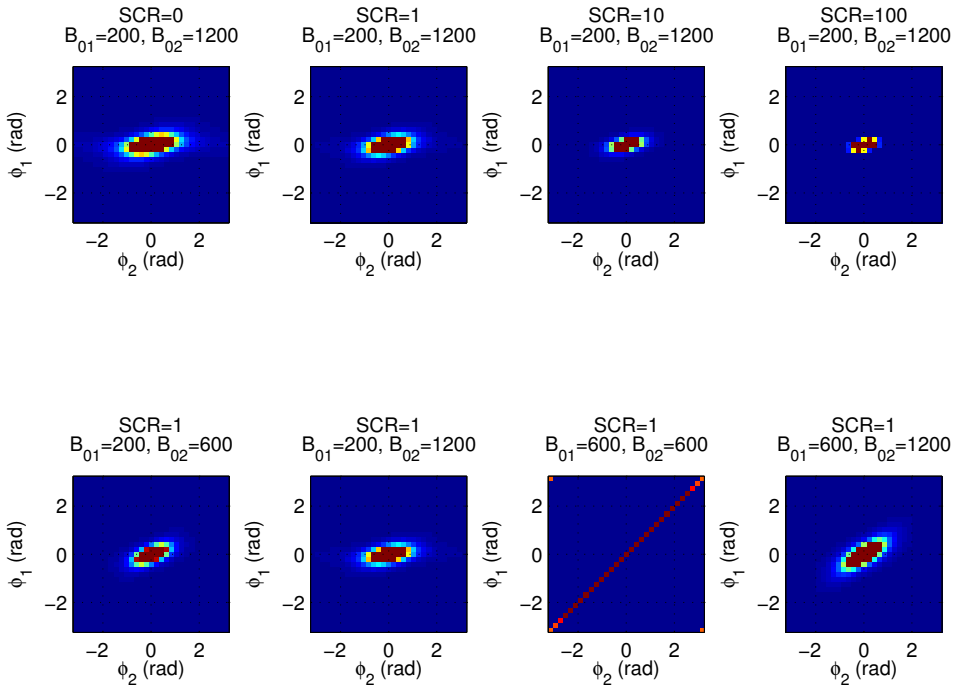

Figure 4.7: Joint phase PDF $f(\phi_{01}, \phi_{02})$ for $N = 2$ interferograms for varying SCR and spatial baseline. Row 1 shows the effect of increasing SCR while baselines are fixed at $B_{01} = 200$ m and $B_{02} = 1200$ m. The plots illustrate that larger baseline causes a larger dispersion in the phase PDF, and that the interferometric phases are not independent. As the SCR increases, the joint phase PDF converges to a delta function at $(\phi_1, \phi_2) = (0, 0)$. Since only spatial decorrelation is modeled, the covariance matrix $\mathbf{\Gamma}$ becomes non-invertible when the two spatial baselines are equal ($B_{01} = B_{02} = 600$ m) and the resulting joint PDF diverges.

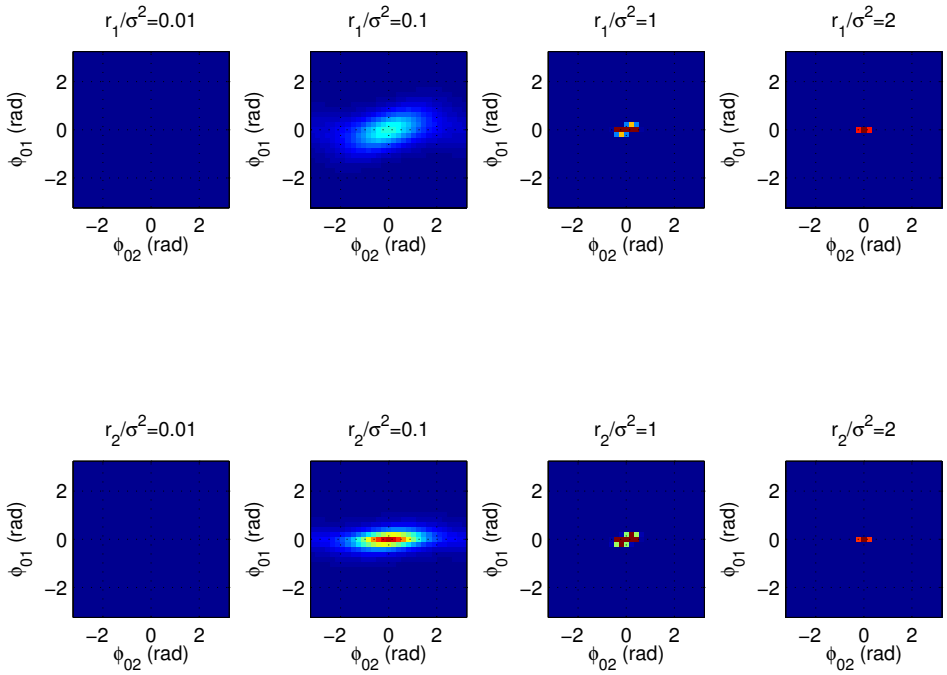

Figure 4.8: Probabilistic distribution $f(\phi_{01}, \phi_{02} \mid r)$ as a function of r. The SCR and spatial baselines are fixed at SCR $= 1$, $B_{01} = 200$ m, and $B_{02} = 1200$ m. In the first row, the phase distribution is plotted for varying given values of r_{01}, the amplitude associated with the smaller baseline. The second row illustrates the variation in the phase distribution as a function of known r_{02}, the amplitude associated with the larger baseline. As either known amplitude increases, the phase distribution converges about the origin. Knowledge of r_{02} provides more information and thus constrains the phase distribution more tightly.

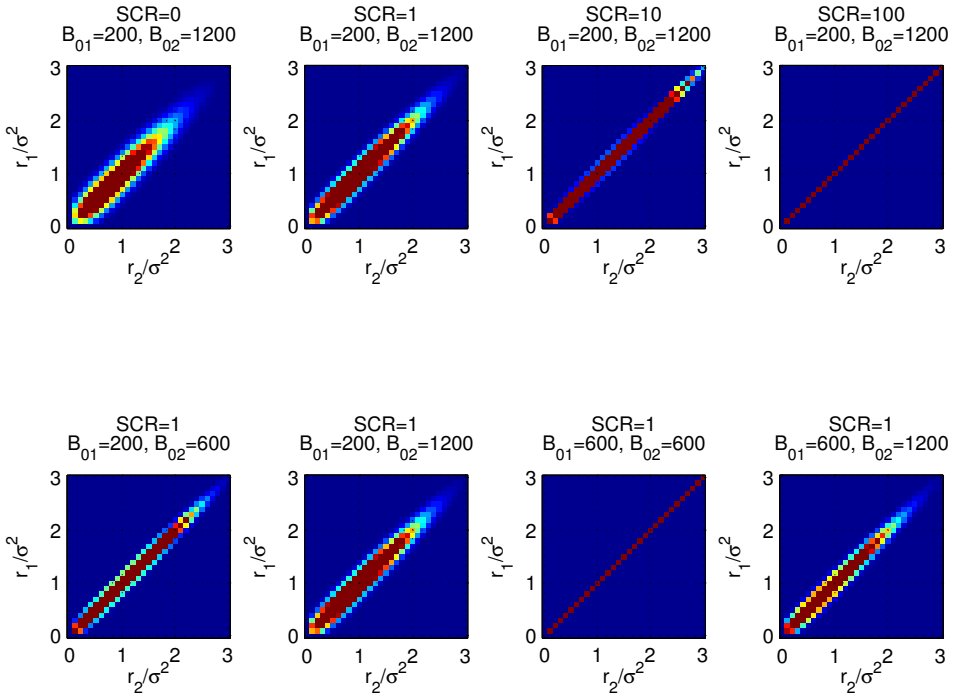

Figure 4.9: Joint amplitude PDF $f(r_{01}, r_{02})$ for $N = 2$ interferograms for varying SCR and spatial baseline. The top row illustrates the effect of increasing SCR while baselines are fixed at $B_{01} = 200$ m and $B_{02} = 1200$ m. As the SCR increases, the joint phase PDF converges toward the diagonal defined by $r_{01} = r_{02}$. The bottom row of the figure shows that dispersion of the PDF about the diagonal depends on the difference between the baselines B_{01} and B_{02} rather than the absolute baseline values themselves. Unlike the joint phase PDF $f(\phi_{01}, \phi_{02})$, the amplitude PDF is virtually symmetric about the diagonal line $r_{01} = r_{02}$ even when $B_{01} \neq B_{02}$, indicating that spatial baseline has much less effect on amplitude dispersion than on phase dispersion.

toward the diagonal line $r_{01} = r_{02}$ as SCR increases. This is expected since the interferometric amplitude for an ideal point target will not vary between radar passes.

In the second row of the figure, we show the variation in the joint amplitude PDF as a function of the imaging spatial baselines. These plots illustrate that the dispersion of the PDF about the diagonal depends on the difference between the baselines B_{01} and B_{02} rather than the absolute baseline values themselves. Unlike the joint phase PDF $f(\phi_{01}, \phi_{02})$, the amplitude PDF is virtually symmetric about the diagonal line $r_{01} = r_{02}$ even when $B_{01} \neq B_{02}$, indicating that spatial baseline has much less effect on amplitude dispersion than on phase dispersion.

Again, we note that the joint PDF diverges when the two spatial baselines are equal. Since only spatial decorrelation is modeled, the covariance matrix $\mathbf{\Gamma}$ becomes non-invertible when the two spatial baselines are equal ($B_{01} = B_{02} = 600$ m) and the resulting joint amplitude PDF diverges.

$f(r_{01}, r_{02} \mid \phi)$**:** Figure 4.8 shows the probabilistic distribution of (r_{01}, r_{02}), given knowledge of interferometric phase ϕ_{01} or ϕ_{02}. The SCR and spatial baselines are fixed at SCR = 1, $B_{01} = 200$ m, and $B_{02} = 1200$ m. In the first row, the amplitude distribution is plotted for varying known values of ϕ_{01}, the phase associated with the smaller baseline. The second row shows the variation in the amplitude distribution as a function of known ϕ_{02}, the phase associated with the larger baseline.

The plots illustrate the interdependence between phase and amplitude, as the distribution of amplitudes varies greatly with known phase. An interferometric phase value of 0 produces the smallest dispersion in the amplitude distribution about the diagonal. As the known phase diverges from 0, the amplitude distribution dispersion increases about the diagonal. Again, the interferogram with the larger baseline and greater spatial decorrelation introduces greater phase uncertainty; hence knowledge of the value of ϕ_{02} provides more information about the amplitude distribution than ϕ_{01}. This is evident by the tighter, higher amplitude distributions in the second row compared to the first.

Marginal amplitude and phase PDFs

The joint phase-amplitude PDF for a single SAR image is computed by setting $N = 0$ in Equation 4.69:

$$f(r_i, \phi_i) = \frac{r_i}{\pi\sigma^2} e^{-\frac{r_i^2}{\sigma^2}}. \tag{4.75}$$

Hence the single SAR marginal amplitude and phase PDFs are given respectively by

$$f(r_i) = \frac{2r_i}{\sigma^2} e^{-\frac{r_i^2}{\sigma^2}} \tag{4.76}$$

$$f(\phi_i) = \frac{1}{2\pi}. \tag{4.77}$$

The PDFs for a single interferogram, formed from the master SAR image and an arbitrary slave $i \in \{1, \ldots, N\}$, can be derived by setting $N = 1$ in the joint multipass PDF (Equation 4.71). The associated covariance matrix is given by

$$\mathbf{\Gamma} = \mathbf{\Gamma}(\mathrm{SCR}, B_{0i}, T_{0i}) = \begin{bmatrix} 1 & \rho(B_{0i}, T_{0i}, \mathrm{SCR}) \\ \rho(B_{0i}, T_{0i}, \mathrm{SCR}) & 1 \end{bmatrix}. \tag{4.78}$$

The resulting single interferogram joint phase-amplitude PDF is

$$f(r_0, r_i, \phi_{0i}) = \frac{2\pi r_0 r_i}{(\pi\sigma^2)^2[1 - \rho^2(B_{0i}, T_{0i}, \mathrm{SCR})]} \exp\left(-\frac{r_0^2 - 2\rho(B_{0i}, T_{0i}, \mathrm{SCR})\cos(\phi_{0i}) r_0 r_i + 2r_i^2}{\sigma^2[1 - \rho^2(B_{0i}, T_{0i}, \mathrm{SCR})]}\right). \tag{4.79}$$

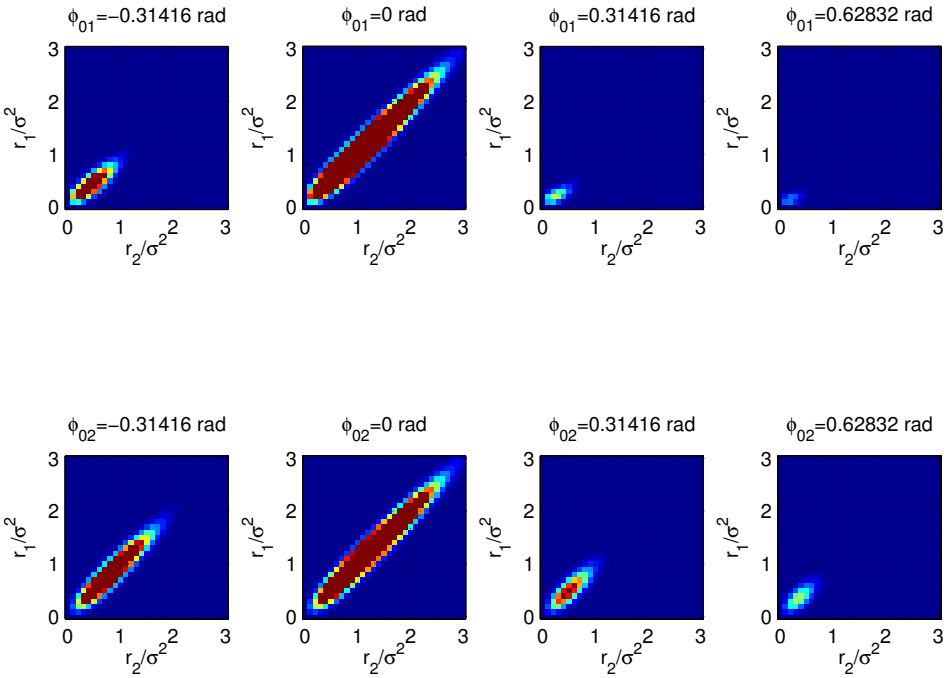

Figure 4.10: Probabilistic distribution $f(r_{01}, r_{02} \mid \phi)$ as a function of ϕ. The SCR and spatial baselines are fixed at SCR = 1, $B_{01} = 200$ m, and $B_{02} = 1200$ m. In the first row, the amplitude distribution is plotted for varying given values of ϕ_{01}, the phase associated with the smaller baseline. The second row illustrates the variation in the amplitude distribution as a function of known ϕ_{02}, the phase associated with the larger baseline. An interferometric phase value of 0 produces the smallest dispersion in the amplitude distribution about the diagonal. As the known phase diverges from 0, the amplitude distribution dispersion increases. Knowledge of the value of larger baseline phase ϕ_{02} provides more information about the amplitude distribution than ϕ_{01}, as evidences by the tighter, higher amplitude distributions in the second row compared to the first.

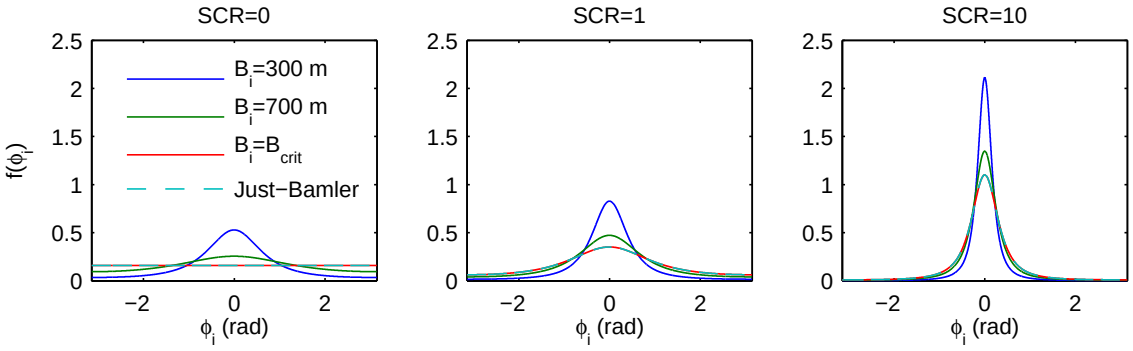

Figure 4.11: The marginal interferometric phase PDF $f(\phi_{0i})$ derived from the PS backscatter model varies as a function of SCR and spatiotemporal baselines. Here the PDF is plotted under the assumption of negligible temporal decorrelation. The PDF converges toward a delta function as SCR goes to infinity or the spatial baseline goes to 0. When the baseline is greater than or equal to the critical baseline, the PDF converges to that derived from the PS SAR pixel model with circularly-symmetric Gaussian signal component [Just and Bamler, 1994].

By integrating Equation 4.79 over the SAR amplitudes r_0 and r_i, we obtain the marginal interferometric phase PDF

$$f(\phi_{0i}) = \frac{1}{2\pi}\frac{1-\rho^2}{1-(\rho\cos\phi_{0i})^2}\left[1+\frac{\rho\cos\phi_{0i}}{\sqrt{1-(\rho\cos\phi_{0i})^2}}\arccos(-\rho\cos\phi_{0i})\right], \tag{4.80}$$

where

$$\rho = \rho(B_{0i}, T_{0i}, \mathrm{SCR}) = \rho_{\mathrm{spatial}}(B_{0i}, \mathrm{SCR}) \cdot \rho_{\mathrm{temporal}}(T_{0i}, \mathrm{SCR}). \tag{4.81}$$

The marginal interferometric phase PDF is plotted in Figure 4.11 as a function of SCR and spatial baseline, assuming that temporal decorrelation is negligible. As the spatial baseline B_{0i} increases for a given SCR, the correlation $\rho(B_{0i}, T_{0i}, \mathrm{SCR})$ decreases, and the interferometric phase PDF (Equation 4.80) becomes more disperse about the mean. This trend holds until $|B_{0i}|$ is greater than the critical baseline B_{crit}, when the correlation converges to $\rho(B_{0i}, \mathrm{SCR}) = \frac{\mathrm{SCR}}{\mathrm{SCR}+1}$. In the case of imaging a purely distributed scattering pixel (SCR $= 0$) with $|B_{0i}| \geq B_{\mathrm{crit}}$, the correlation is equal to 0 and the marginal interferometric phase is uniformly distributed over $[-\pi, \pi]$.

In the limit where the baselines are zero or the SCR goes to infinity, $f(\phi_{0i})$ converges to a delta function at $\phi_{0i} = 0$, as expected.

4.5 Analytical comparison and discussion

In this chapter, we presented two analytical models for persistent scatterers:

- The *PS SAR pixel model* (Section 4.3), which abstracts the complex SAR pixel u_i as the sum of a signal variable s and a clutter variable c_i. We analyzed three statistical models for the signal component s:

  1. $s \sim \mathcal{CN}(\mu, \sigma_s^2)$ (Section 4.3.1)
  2. $s \sim \mathcal{CN}(0, \sigma_s^2)$ (Section 4.3.2)
  3. $s \sim \mathcal{CN}(\mu, 0)$ (Section 4.3.3)

  In each case, the clutter c_i is modeled as an independent and identically distributed, circularly-symmetric, white Gaussian process over acquisitions $i = 0, \ldots, N$.

- The *PS backscatter model* (Section 4.4), which models the backscattering spatial function $f(x, y)$ of the PS resolution element as the superposition of a dominant scatterer, described by backscattering function $f_s(x, y)$, and clutter scatterers, described by backscattering function $f_c(x, y)$. The clutter backscatter function $f_c(x, y)$ is an independent and identically distributed, circularly-symmetric, white, Gaussian process over azimuth x and range y.

In this section, we discuss the relationship between the PS SAR pixel and PS backscatter models. We compare the derived interferometric statistical characterizations and show how the PS backscatter model results generalize those of the PS SAR pixel model.

The fundamental differences between the PS SAR pixel model and the PS backscatter model result from the characterization of clutter correlation. The SAR pixel model uses an initial assumption that c_i is uncorrelated between SAR acquisitions i and j, regardless of the spatial baseline B_{ij} and temporal baseline T_{ij}. The PS backscatter model removes this assumption. Instead, the clutter correlation between acquisitions is analytically derived from first principles, starting from a model of the backscatter function. This derivation shows that the clutter contribution to the SAR pixel value is in fact correlated between acquisitions, and that the amount of clutter correlation is a function of spatiotemporal baselines.

As a result, the SAR pixels $\mathbf{u}$ have covariance matrix entries

$$\mathbf{\Gamma}_{ij} = \begin{cases} 1, & i = j \\ \frac{\mathrm{SCR}}{\mathrm{SCR}+1}, & i \neq j. \end{cases} \tag{4.82}$$

for the PS SAR pixel model derivation, versus

$$\mathbf{\Gamma}_{ij} = \rho(B_{ij}, T_{ij}, \mathrm{SCR}) = \rho_{\mathrm{spatial}}(B_{ij}, \mathrm{SCR}) \cdot \rho_{\mathrm{temporal}}(T_{ij}, \mathrm{SCR}), \tag{4.83}$$

for the PS backscatter model derivation, where

$$\rho_{\text{spatial}}(B_{ij}, \text{SCR}) = \begin{cases} 1, & i = j \\ \frac{1}{1+\text{SCR}} \left(1 - \frac{2R_y \cos\theta |B_{ij}|}{\lambda r}\right) + \frac{\text{SCR}}{1+\text{SCR}}, & i \neq j, |B_{ij}| < B_{\text{crit}} \\ \frac{\text{SCR}}{1+\text{SCR}}, & i \neq j, |B_{ij}| \geq B_{\text{crit}}. \end{cases} \tag{4.84}$$

The PS backscatter model form of $\mathbf{\Gamma}$ thus generalizes the SAR model form by accounting for the effect of spatial and temporal baselines. The two forms are equivalent when the spatial baseline B_{ij} is greater than the critical baseline B_{crit} and temporal decorrelation is ignored.

If the signal component of the PS SAR pixel is modeled as a circularly-symmetric Gaussian, then the derived multipass joint SAR pixel PDF $f(\mathbf{u})$, joint SAR phase-amplitude PDF $f(r_0, \ldots, r_N, \phi_0, \ldots, \phi_N)$, and joint interferometric phase-amplitude PDF $f(r_0, \ldots, r_N, \phi_{01}, \ldots, \phi_{0N})$ have the same form as those derived from the PS backscatter model, except for the entries of the covariance matrix $\mathbf{\Gamma}$. When the covariance matrix forms are equivalent, under the conditions described above, then the phase-amplitude PDFs for the PS SAR pixel model and backscatter model coincide exactly.

Hence the interferometric phase PDF derived from the PS backscatter model (Equation 4.80) is a generalization of the interferometric phase PDF derived from the SAR pixel PS model with circularly-symmetric Gaussian signal (Equation 4.19, [Just and Bamler, 1994]). The PDFs in Equations 4.19 and 4.80 are equivalent except for the value of correlation ρ:

- SAR pixel PS model with Gaussian signal:

$$\rho = \rho(\text{SCR}) = \frac{\text{SCR}}{1 + \text{SCR}} \tag{4.85}$$

- Backscatter PS model:

$$\rho = \rho(\text{SCR}, B_{0i}, T_{0i}) = \rho_{\text{spatial}}(B_{0i}, \text{SCR}) \cdot \rho_{\text{temporal}}(T_{0i}, \text{SCR}), \tag{4.86}$$

  where

$$\rho_{\text{spatial}}(B_{ij}, \text{SCR}) = \begin{cases} \frac{1}{1+\text{SCR}} \left(1 - \frac{2R_y \cos\theta |B_{ij}|}{\lambda r}\right) + \frac{\text{SCR}}{1+\text{SCR}}, & |B_{ij}| < B_{\text{crit}} \\ \frac{\text{SCR}}{1+\text{SCR}}, & |B_{ij}| \geq B_{\text{crit}}. \end{cases} \tag{4.87}$$

The values of ρ for the two models are equivalent in the limit when the temporal decorrelation is ignored and the spatial baseline B_{0i} is greater than the critical baseline B_{crit}.

Figure 4.11 shows a comparison of the interferometric phase PDFs derived from the two PS models (Equations 4.80 and 4.19), ignoring the effect of temporal decorrelation. The PS SAR pixel model underestimates the clutter correlation and thus overestimates the dispersion of the phase PDF when $|B_{0i}| < B_{\text{crit}}$. The derived PDFs coincide when the spatial baseline is greater than or equal to

the critical baseline.

The PS backscatter model thus removes several of the simplifying assumptions inherent in the PS SAR pixel model. By modeling the PS as a backscattering spatial function and incorporating a new multipass imaging system model, we analytically derived the following interferometric statistical characteristics from first principles:

- The clutter contribution to the SAR pixels u_i is generally correlated between acquisitions i and j, not independent. Hence the PS SAR pixel model, which only accounts for correlation of the dominant scatterer, underestimates the total correlation between SAR acquisitions.
- The correlation between SAR pixels u_i and u_j is a function of both SCR and spatiotemporal baselines B_{ij} and T_{ij}. Hence the pixels $\{u_0, \ldots, u_N\}$ are generally not identically distributed.
- The joint distribution of the interferometric phases $\{\phi_{01}, \ldots, \phi_{0N}\}$ is characterized by the covariance matrix $\mathbf{\Gamma}(\text{SCR}, \mathbf{B}, \mathbf{T})$, where each entry $\mathbf{\Gamma}_{ij}$ of the matrix is given by the total correlation between SAR acquisitions i and j. Hence the multipass interferometric phases are generally neither independent nor identically distributed.

The PS backscatter model derivations therefore generalize the PS SAR pixel model derivations, enabling a more complete statistical characterization of the resulting interferometric PS pixels.

4.6 Directions for future analysis

The PS backscatter model analysis presented in this chapter assumed that the interferometric stack $\mathbf{z}$ is formed using a common master SAR image, i.e. $\mathbf{z} = u_0\mathbf{u}^*$. The analysis can be easily extended to account for any instantiation of a well-determined, non-cyclic interferometric stack formation. The interferogram formation process is mathematically represented by the change of variables in Equations 4.70-4.73, which transforms the joint SAR pixel PDF to the joint interferometric pixel PDF. Any non-cyclic formation graph of N interferograms from $N+1$ SAR images will produce an invertible Jacobian matrix J for this change of variables and hence a well-defined joint interferometric PDF. If the formation graph is also fully connected, the resulting covariance matrix $\mathbf{\Gamma}$ is identical to that given in Equations 4.67-4.62. Examples of non-cyclic interferometric stack formation graphs are shown in Figure 4.12.

If cycles are introduced into the interferometric stack formation graph, e.g. those shown in Figure 4.13, then the system is overdetermined. The invertibility of J no longer holds and a straightforward extension of the change of variables in Equations 4.70-4.73 is insufficient. An important direction for further research is extending the analysis of this chapter to such cases.

The most general instantiation of a cyclic interferometric stack is the formation of every possible master-slave interferometric pair from the stack of SAR pixels $\mathbf{u}$. The resulting interferometric pixels are mathematically formulated as $\mathbf{Z} = \mathbf{u}\mathbf{u}^\dagger$, where each row i is denoted by $\mathbf{z}_i$ and corresponds

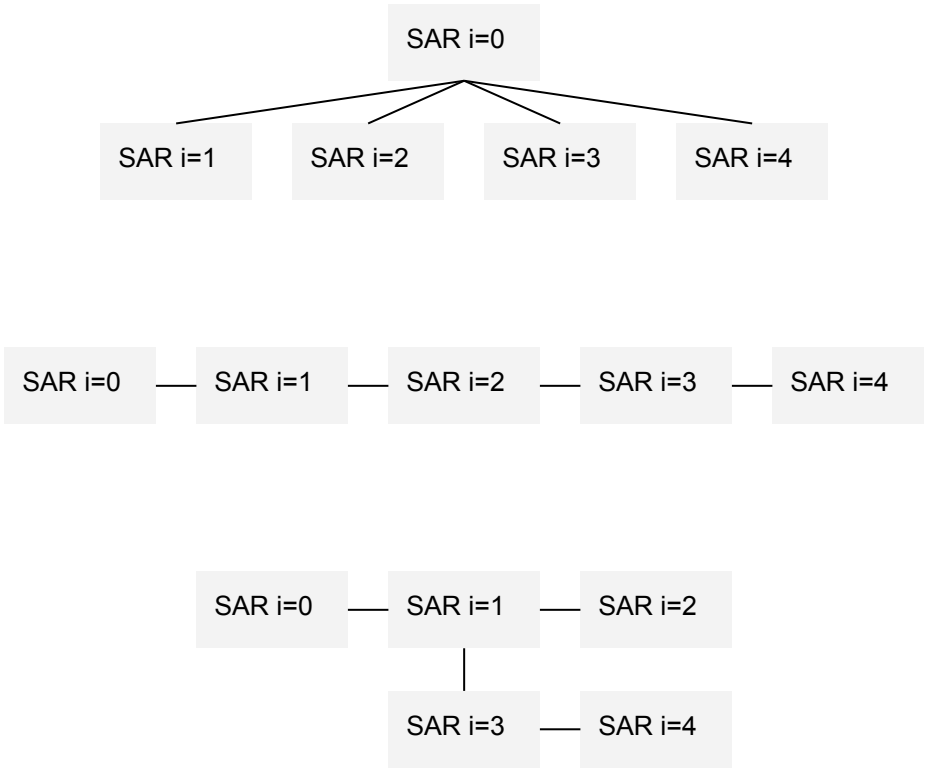

Figure 4.12: Non-cyclic interferometric stack formation graphs with covariance matrix $\mathbf{\Gamma}$ (Equations 4.67-4.62).

to the pixels formed from master SAR image i. One possible approach to deriving the PDF of the full set of pixels is to modify the multipass interferometric system such that each row $\mathbf{z}_i$ as an independent vector observation. We conjecture that the covariance matrix of these pixels is equivalent to Equation 4.67, which already contains the analytical correlation between every pair of SAR images.

Finally, future work is needed to formalize the analysis of temporal decorrelation in the PS backscatter model derivation. In this chapter, we simplified our analysis by first assuming a time-invariant backscatter function $f(x, y)$ and deriving the corresponding PDFs for spatial decorrelation. Temporal decorrelation was then incorporated directly into the entries of the resulting covariance matrix $\mathbf{\Gamma}$. We can remove this simplifying assumption in the future by modeling the temporal change in the backscatter function $f(x, y, t)$.

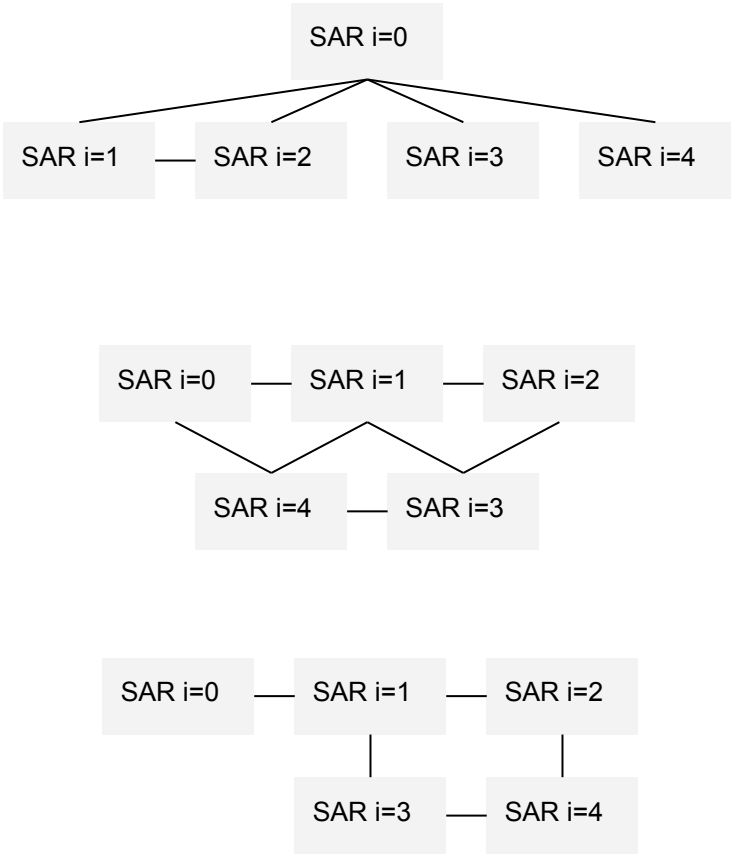

Figure 4.13: Cyclic interferometric stack formation graphs where covariance matrix $\mathbf{\Gamma}$ (Equations 4.67-4.62) is no longer valid.

Chapter 5

Partially correlated persistent scatterer selection for InSAR deformation measurement

5.1 Introduction

In the previous chapters, we quantified the PS spatiotemporal decorration and phase probabilitistic distribution as a function of SCR and spatial and temporal imaging baselines. These results showed that PS pixels – those with a dominant, point-like scatterer – are more immune to decorrelation phase noise than pixels with low SCR. PS techniques aim to utilize this property in order to extract deformation measurements in areas of low coherence, where conventional InSAR fails to produce useful observations [Crosetto et al., 2009, Crosetto et al., 2015].

A critical step in PS techniques is the selection of PS pixels. Phase unwrapping and subsequent deformation estimation on the spatially sparse PS network depends on both pixel selection accuracy and the network density. Existing PS methods that model PS as a non-decorrelating point scatterer with additive white decorrelation noise have been shown to work well in urban areas with many strong, stable reflectors. However identifying an appropriate network of pixels in natural or vegetated terrain remains a challenge due to other spatiotemporally varying phase terms.

In this chapter, we first review existing PS selection techniques. We then present a new method of PS characterization and selection based on the analytical results of the previous chapters. This method optimally combines the full stack of phase and amplitude observations, as well as information about the spatiotemporal baselines. We perform a case study to estimate the performance in terms of PS identification and false detection compared other PS methods. Our results based on simulated and real data demonstrate that with an increased amount of information, we obtain better PS

parameter estimation and selection.

We then show how the improved PS selection method can fit within existing PS frameworks. We describe the general StaMPS framework for PS deformation measurement, emphasizing the critical step of PS selection. Finally, we present a set of example deformation measurements from a variety of real satellite radar data using the StaMPS with the new PCPS selection method.

5.2 Prior PS selection techniques

The selection of PS pixels from the interferometric radar images is a critical step in persistent scatterer techniques. The identification of pixels with low decorrelation phase noise is not trivial due to other phase contributions:

$$\Delta\phi_{\text{ifg}} = \phi_{\text{def}} + \phi_{\text{atm}} + \phi_{\text{err}} + \phi_{\text{decorr}} + \phi_{\text{noise}} \tag{5.1}$$

Prior work in PS characterization and selection techniques have generally utilized ad hoc statistical or empirically-based tests on the observed interferometric amplitudes or phases, summarized below.

5.2.1 Amplitude

The PS-InSAR technique [Ferretti et al., 2001] selects PS pixels based on a measure of amplitude dispersion, given by

$$\mathcal{D}_A = \frac{\sigma_A}{\mu_A}. \tag{5.2}$$

where σ_A and μ_A are the standard deviation and mean of the SAR amplitudes. The authors showed that at high SNR, the amplitude dispersion is well-correlated with phase stability and is more immune to nuisance signals such as atmospheric delay and orbital error. However this correlation between amplitude dispersion and phase stability breaks down as SNR decreases, especially for SNR ≤ 2.

Since the introduction of PS-InSAR, other techniques have been developed that use amplitude analysis to identify PS pixels. The Spatio-Temporal Unwrapping Network (STUN) method [Kampes and Adam, 2006] estimates the signal-to-clutter ratio (SCR) of each oversampled pixel as the ratio of its power to the power of neighboring pixels. SqueeSAR [Ferretti et al., 2011] is a refinement of PS-InSAR designed to jointly process distributed scatterers (DS) along with PS in order to increase the density of selected pixels. This technique utilizes space adaptive filtering in order to increase SNR by averaging over statistically homogenous DS, while preserving the high SNR of single PS pixels, selected using amplitude dispersion.

It is worth noting that many other techniques (e.g. [Werner et al., 2003, Agram, 2010]) employ loose limits on amplitude dispersion or similar simple amplitude statistics in order to identify an

initial set of PS candidates. This initial candidate selection step takes advantage of relatively low complexity criteria to reduce the set of pixels that must be processed, while ultimately employing other selection metrics after some spatiotemporal filtering to choose the final set of selected PS.

5.2.2 Phase

Amplitude-based techniques work well for urban areas where manmade infrastructure produces many bright reflectors, but generally fail to identify a sufficient density of PS pixels in natural or vegetated terrain [Ferretti et al., 2011]. To allow PS analysis to be extended to such areas, Hooper et al. introduced a new class of PS selection techniques based on phase analysis rather than amplitude statistics [Hooper et al., 2004].

In the StaMPS algorithm [Hooper, 2006], PS pixels are identified as those with high temporal phase coherence γ_x, defined as

$$\gamma_x = \frac{1}{N}\left|\sum_{i=1}^{N}\exp\{j\hat{\phi}_{\text{noise},x,i}\}\right| \tag{5.3}$$

where $\hat{\phi}_{\text{noise},x,i}$ is an estimate of the phase noise term for pixel x in interferogram i. StaMPS computes this estimate by iteratively filtering the interferometric phase $\psi_{int,x,i}$ and subtracting the spatially correlated result $\tilde{\psi}_{int,x,i}$, as well as an estimate of the spatially uncorrelated phase term $\Delta\hat{\phi}^{u}_{\theta,x,i}$ due to look angle error:

$$\hat{\phi}_{\text{noise},x,i} = \psi_{int,x,i} - \tilde{\psi}_{int,x,i} - \Delta\hat{\phi}^{u}_{\theta,x,i}. \tag{5.4}$$

Using this phase analysis technique, StaMPS has identified PS networks in non-urban areas such as volcanoes [Hooper et al., 2004, Hooper et al., 2007], rural subsidence bowls [Sousa et al., 2009], and fault zones [Champenois et al., 2012].

The StaMPS phase analysis for PS selection was refined in [Shanker and Zebker, 2007] using an information theoretic approach. Here, the maximum likelihood estimate of each pixel's SCR is computed using the Gaussian signal in Gaussian noise phase PDF model in Equation 4.19 [Just and Bamler, 1994].

Other phase-based analysis for PS selection include the Interferometric Point Target Analysis technique [Werner et al., 2003], which utilizes a measure of spectral phase diversity. The Persistent Scatterer Pairs (PSP) method [Costantini et al., 2008] utilizes a measure of weighted coherence over two spatially close points, in order to eliminate the need to perform spatial filtering to remove atmospheric and orbital error phase contributions prior to selection. The Quasi-Permanent Scatterer (QPS) method [Perissin and Wang, 2012] extends PS analysis to include all possible interferogram pairs from a stack of SAR images, rather than using a single common master. Partially coherent PS pixels are then identified using temporal coherence similar to Equation 5.3, but where each

interferogram's phase contribution to the coherence is weighted by the spatial coherence in a window around the pixel in that interferogram.

In general, the phase-based techniques for identifying and selecting PS pixels improved PS deformation analysis in non-urban areas. However the accuracy and density of the identified networks in natural terrain remain a challenge. Recent work on partially coherent PS pixels [Wang et al., 2008, Prati et al., 2010] have suggested that such techniques can dramatically increase the number of pixels identified over StaMPS.

5.3 PCPS selection

In this section, we present a new method for statistical identification and selection of partially coherent PS pixels, based on the analysis presented in Chapters 3-4.

5.3.1 Analytical foundation

Below, we summarize the main analytical results and their impact on the design of the PS selection technique:

- *Analysis:* We quantified phase stability, the defining property of persistent scatterer pixels, using decorrelation as a function of SCR (Chapter 3).
  Algorithm: We use estimated SCR as a basis for PS identification and selection.

- *Analysis:* We derived the joint multipass interferometric PDF across both phase and amplitude (Chapter 4).
  Algorithm: We use the full stack of interferometric phase and amplitude observations to perform maximum-likelihood SCR estimation.

- *Analysis:* We quantifed the effect of spatial and temporal baselines on the probabilitistic distribution of interferometric phase and amplitude.
  Algorithm: We quantitatively account for the physical imaging parameters of spatial and temporal baseline in the PS characterization and selection.

- *Analysis:* We showed that the interferometric phase observations are neither independent nor identically distributed (Chapter 4).
  Algorithm: We use a joint PDF characterizing the full stack of multipass interferometric observations to perform maximum-likelihood SCR estimation.

- *Analysis:* We quantified the phase stability of partially correlated persistent scatterers for baselines over the critical baseline ($B_{ij} > B_{\text{crit}}$).
  Algorithm: We include all interferograms in the PS selection analysis, including those over the

critical baseline, using analytical models that quantitatively adjust for baseline impact on the decorrelation.

- *Analysis:* We showed that partially correlated persistent scatterers can be quantitatively characterized using SCR.
  Algorithm: By adjusting the threshold on the estimated SCR needed for pixel selection, we analytically tune the tradeoff between PCPS network density and phase stability of the selected pixels.

5.3.2 Maximum likelihood parameter estimation

The basis for our PS selection method is maximum likelihood (ML) parameter estimation. Shanker and Zebker [Shanker and Zebker, 2007] showed that ML estimation provided an information theoretic framework for SCR estimation given an the observed interferometric phase values. They used the assumption that the phase value in each interferogram is independent and identifically distributed according to the marginal phase distribution derived by Just et al. [Just and Bamler, 1994]:

$$\mathrm{SCR}_{\mathrm{ML}} = \arg\max_{\mathrm{SCR}} f(\phi_{01}, \ldots, \phi_{0N} \mid \mathrm{SCR}) \tag{5.5}$$

$$= \arg\max_{\mathrm{SCR}} \prod_i f(\phi_{0i} \mid \mathrm{SCR}), \tag{5.6}$$

where

$$f(\phi_{0i} \mid \mathrm{SCR}) = \frac{1}{2\pi} \frac{1-\rho^2(\mathrm{SCR})}{1-(\rho(\mathrm{SCR})\cos\phi_{0i})^2} \left[1 + \frac{\rho(\mathrm{SCR})\cos\phi_{0i}}{\sqrt{1-(\rho(\mathrm{SCR})\cos\phi_{0i})^2}} \arccos(-\rho(\mathrm{SCR})\cos\phi_{0i})\right], \tag{5.7}$$

and $\rho(\mathrm{SCR}) = \frac{\mathrm{SCR}}{1+\mathrm{SCR}}$.

The maximum likelihood SCR framework can be extended for the analysis presented in earlier chapters by using the joint interferometric stack phase-amplitude PDF (Equation 4.71). Given the observed interferometric phases $\phi_{01}, \ldots, \phi_{0N}$ and SAR amplitudes $r_0, \ldots, r_N$, the maximum likelihood SCR is given by

$$\mathrm{SCR}_{\mathrm{ML}} = \arg\max_{\mathrm{SCR}} f(r_0, \ldots, r_N, \phi_{01}, \ldots, \phi_{0N} \mid \mathrm{SCR}) \tag{5.8}$$

$$= \arg\max_{\mathrm{SCR}} \frac{2\pi}{(\pi\sigma^2)^{N+1}|\mathbf{\Gamma}(\mathrm{SCR}, \mathbf{B}, \mathbf{T})|} \left(\prod_{i=0}^{N} r_i\right) \exp\left[-\frac{1}{\sigma^2}\sum_{i=0}^{N}\sum_{j=0}^{N}[\mathbf{\Gamma}^{-1}(\mathrm{SCR}, \mathbf{B}, \mathbf{T})]_{ij}\alpha_{ij}r_i r_j\right], \tag{5.9}$$

where

$$\alpha_{ij} = \begin{cases} 1, & i = j = 0 \\ \cos(\phi_{0j}), & i = 0, j \neq 0 \\ \cos(\phi_{0i}), & i \neq 0, j = 0 \\ \cos(\phi_{0j} - \phi_{0i}), & i \neq 0, j \neq 0. \end{cases} \tag{5.10}$$

The entries of the covariance matrix $\mathbf{\Gamma}(\mathrm{SCR}, \mathbf{B}, \mathbf{T})$ are given by the analytical decorrelation between each pair of SAR images,

$$\mathbf{\Gamma}_{ij}(\mathrm{SCR}, \mathbf{B}, \mathbf{T}) = \rho(B_{ij}, T_{ij}, \mathrm{SCR}) \qquad = \rho_{\mathrm{spatial}}(B_{ij}, \mathrm{SCR}) \cdot \rho_{\mathrm{temporal}}(T_{ij}, \mathrm{SCR}). \tag{5.11}$$

The SCR estimate specified by Equation 5.9 is the first PS characterization technique that utilizes physically-based statistical derivations to simultaneously combine the entire stack of amplitude and phase observations. PCPS pixels may then be selected by imposing a threshold on the estimated SCR values.

In contrast to previous PS selection techniques that have considered only amplitude (e.g. [Ferretti et al., 2001]) or phase (e.g. [Shanker and Zebker, 2007]), this maximum likelihood PS selection method uses both sets of observations simultaneously. Because the distribution $f(r_0, \ldots, r_N, \phi_{01}, \ldots, \phi_{0N})$ depends on spatial and temporal baselines, this PS selection method also quantitively incorporates information about the spatiotemporal baselines of the stack. Instead of assuming that observations are independent and identically distributed, the joint distribution accounts for correlation between every pair of SAR scenes, modeled by the covariance matrix $\mathbf{\Gamma}$.

Below, we discuss some of the algorithmic details and considerations for implementation.

Total backscatter power

The phase-amplitude PDF $f(r_0, \ldots, r_N, \phi_{01}, \ldots, \phi_{0N})$ is a function of the average total pixel backscatter power σ^2. In order to remove this dependency, we treat σ^2 as an unknown parameter to be estimated. The maximum likelihood estimate is given by

$$\sigma^2_{\mathrm{ML}} = \arg\max_{\sigma^2} f(r_0, \ldots, r_N, \phi_{01}, \ldots, \phi_{0N} \mid \mathrm{SCR}, \sigma^2) \tag{5.12}$$

$$= \arg\max_{\sigma^2} \log f(r_0, \ldots, r_N, \phi_{01}, \ldots, \phi_{0N} \mid \mathrm{SCR}, \sigma^2). \tag{5.13}$$

A closed form expression for σ^2_{ML} may be found by calculating the zeros of the derivative of the

log likelihood function (Equation 5.13) with respect to σ^2:

$$\frac{d}{d\sigma^2} \log f(r_0, \ldots, r_N, \phi_{01}, \ldots, \phi_{0N} \mid \mathrm{SCR}, \sigma^2)\Big|_{\sigma^2=\sigma^2_{\mathrm{ML}}} = 0 \tag{5.14}$$

$$\frac{d}{d\sigma^2} \log \left(\frac{2\pi}{(\pi\sigma^2)^{N+1}|\mathbf{\Gamma}|} \left(\prod_{i=0}^{N} r_i \right) \exp \left[-\frac{1}{\sigma^2} \sum_{i=0}^{N} \sum_{j=0}^{N} [\mathbf{\Gamma}^{-1}]_{ij} \alpha_{ij} r_i r_j \right] \right) \Bigg|_{\sigma^2=\sigma^2_{\mathrm{ML}}} = 0 \tag{5.15}$$

$$-\frac{N+1}{\sigma^2} + \frac{\sum_{i=0}^{N} \sum_{j=0}^{N} \alpha_{ij} r_i r_j}{\sigma^4} \Bigg|_{\sigma^2=\sigma^2_{\mathrm{ML}}} = 0 \tag{5.16}$$

Solving Equation 5.14 for σ^2 gives

$$\sigma^2_{\mathrm{ML}} = \frac{1}{N+1} \sum_{i=0}^{N} \sum_{j=0}^{N} [\mathbf{\Gamma}^{-1}]_{ij} \alpha_{ij} r_i r_j. \tag{5.17}$$

By substituting Equation 5.17 into 5.9, we obtain the expression

$$\mathrm{SCR}_{\mathrm{ML}} = \arg\max_{\mathrm{SCR}} \frac{2\pi}{|\mathbf{\Gamma}(\mathrm{SCR}, \mathbf{B}, \mathbf{T})|} \left(\prod_{i=0}^{N} r_i \right) \left(\frac{N+1}{\pi e \sum_{i=0}^{N} \sum_{j=0}^{N} [\mathbf{\Gamma}^{-1}(\mathrm{SCR}, \mathbf{B}, \mathbf{T})]_{ij} \alpha_{ij} r_i r_j} \right)^{N+1} \tag{5.18}$$

where

$$\alpha_{ij} = \begin{cases} 1, & i = j = 0 \\ \cos(\phi_{0j}), & i = 0, j \neq 0 \\ \cos(\phi_{0i}), & i \neq 0, j = 0 \\ \cos(\phi_{0j} - \phi_{0i}), & i \neq 0, j \neq 0. \end{cases} \tag{5.19}$$

Temporal decorrelation model parameters

If the parameters of the temporal decorrelation model are not known a priori, they may be concurrently estimated during the maximum likelihood SCR process. For the base linear model described in Section 3.4.2, for example, the critical temporal baseline T_{crit} may be estimated as

$$\begin{bmatrix} \mathrm{SCR}_{ML} \\ T_{\mathrm{crit,ML}} \end{bmatrix} = \arg \max_{\mathrm{SCR}, T_{\mathrm{crit}}} f(r_0, \ldots, r_N, \phi_{01}, \ldots, \phi_{0N} \mid \mathrm{SCR}, T_{\mathrm{crit}}). \tag{5.20}$$

Discussion of multidimensional optimization methods is beyond the scope of this thesis.

5.3.3 Covariance matrix stability

The covariance matrix $\mathbf{\Gamma}$ can become unstable or overly constrained for very small baseline pairs due to small theoretical decorrelation. Hence, in practice, it is useful to include an empirical noise decorrelation factor ρ_{noise} to the entries of the covariance matrix, i.e.

$$\mathbf{\Gamma}_{ij}(\text{SCR}, \mathbf{B}, \mathbf{T}) = \rho(B_{ij}, T_{ij}, \text{SCR}) \cdot \rho_{\text{noise}} \tag{5.21}$$

to ensure that the analytical PDF does not become ill-conditioned.

5.3.4 Software implementation

In the software implementation, the computational complexity of the maximum likelihood estimation may be decreased by maximizing the log likelihood rather than the original distribution. In addition, for a given set of multipass interferometric data, the covariance matrix $\mathbf{\Gamma}(\text{SCR}, \mathbf{B}, \mathbf{T})$ can be precomputed in a lookup table for each value of SCR in the optimization search space.

5.3.5 Selection criteria

After characterizing each pixel by its maximum likelihood SCR, we perform PCPS selection by thresholding the SCR_{ML} value, as illustrated in Figure 5.1.

The statistical PS characterizations presented in Chapters 3-4 provide an analytical justification for using SCR as a PS selection criteria, as well as a framework with which to determine the SCR threshold value. Below we provide a qualitative outline of this justification and framework, leaving the full theoretical analysis for future work.

PS techniques are fundamentally founded on the concept of a network of pixels where the deformation phase can be accurately extracted from other nuisance phase terms. The decorrelation phase term is the greatest limiting factor in this deformation extraction, due to noise-like characteristics. Hence the accuracy of unwrapping and deformation estimation in these techniques is fundamentally limited by the distribution of the decorrelation phase noise; the greater the variance of the decorrelation phase term, the less accurate the extraction of the deformation phase signal. Because we showed that the distribution of the decorrelation phase component is an analytical function of SCR, the fundamental limits of PS deformation estimation accuracy may be quantitatively related to SCR.

Therefore we can set the SCR threshold based on the PS deformation estimation accuracy requirements, as determined by the tolerable variance of the decorrelation phase term. That is, if we determine an acceptable level of decorrelation phase variance, we can use the analytical phase

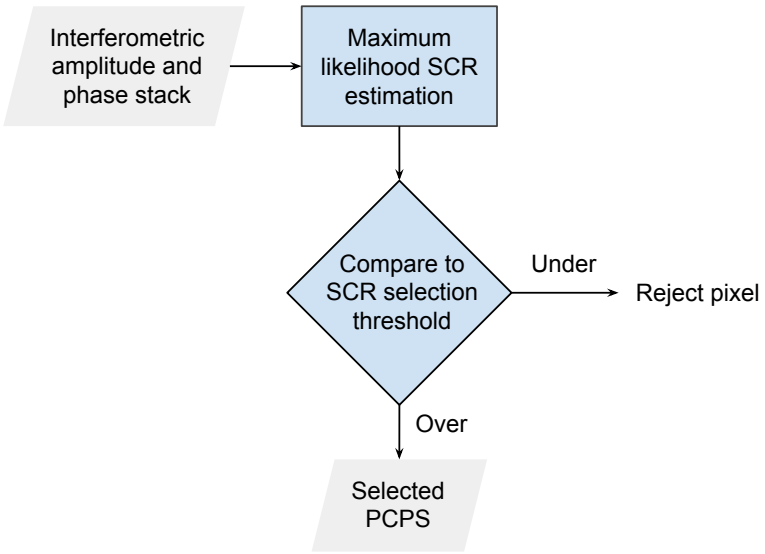

Figure 5.1: PCPS selection flow diagram

distribution to compute the associated minimum SCR necessary for the given imaging baselines. This value then sets the SCR threshold for PS selection.

We may extend the criteria for PS selection beyond just SCR by also thresholding the concurrently estimated value of T_{crit}, as described in Section 5.3.2. This threshold imposes a limit on the expected temporal decorrelation for each selected PS pixel.

5.4 Comparison of selection techniques

We evaluate the PCPS selection technique against two standard existing PS methods: PS-InSAR [Ferretti et al., 2001] and StaMPS [Hooper et al., 2004] with the maximum likelihood PS selection technique devleoped by [Shanker and Zebker, 2007].

Table 5.1 summarizes the fundamental differences between the PS-InSAR, MLPS StaMPS, and PCPS slelection techniques. Compared to the other two methods, the PCPS technique utilizes the full stack of multipass interferometric phases and amplitudes, combining them in a quantitative framework that accounts for both correlation between interferograms and the imaging spatiotemporal baselines.

5.5 Simulation

To compare the performance of PS identification algorithms, we simulate a series of PS pixels with varying SCR and Gaussian noise. Each simulated resolution element contains 1000 randomly placed

Technique	Selection criteria	Accounts for correlation between IFGs?	Accounts for spatiotemporal baselines?	Observations used
PSInSar	Amplitude dispersion	No	No	Amplitude
MLPS StaMPS	ML SCR with marginal phase PDF	No	No	Phase
PCPS	ML SCR with joint multipass PDF	Yes	Yes	Phase, amplitude

Table 5.1: Compared to PS-InSAR and MLPS StaMPS, the PCPS technique utilizes the full stack of multipass interferometric phases and amplitudes, combining them in a quantitative framework that accounts for both correlation between interferograms and the imaging spatiotemporal baselines.

scatterers with uncorrelated complex reflectivity and total average power $\frac{1}{1+\mathrm{SCR}}$, plus a centered dominant scatterer with average power $\frac{\mathrm{SCR}}{1+\mathrm{SCR}}$. The multipass SAR pixel values for each resolution element is computed using the interferometric stack imaging system model described in Section 4.4.1. Finally, complex white Gaussian noise with varying standard deviation is added to the SAR pixel values.

For each multipass pixel stack, we evaluate the selection criteria for three PS techniques:

- PS-InSAR [Ferretti et al., 2001]: amplitude dispersion
- MLPS StaMPS [Shanker and Zebker, 2007]: maximum likelihood SCR using the Just-Bamler marginal phase distribution [Just and Bamler, 1994]
- PCPS: maximum likelihood SCR using the joint multipass stack phase-amplitude distribution

Figure 5.2 shows the results of these PS selection criteria as a function of SCR and noise standard deviation. Each column of subplots corresponds to one PS technique, with the selection metric indicated on the y-axis. The subplot rows correspond to decreasing SCR from top to bottom.

Within each subplot, the selection metric value data points are plotted for increasing values of Gaussian noise standard deviation, with the standard deviation of the selection metric indicated by vertical bars. Increasing the Gaussian noise standard deviation causes the plotted points to move right along the phase standard deviation axis. As SCR decreases, the phase standard deviations increases for each Gaussian noise level, as expected and as indicated by the rightward-moving trend of data points moving down each subplot column. Typical threshold values are indicated for each PS technique by the dashed red lines.

The PS-InSAR amplitude distribution technique identifies pixels with very high SCR, but fails to find many pixels when the SCR decreases below 10. The low density of identified pixels in low SCR environments is a PS-InSAR weakness that has been identified by previous researchers [Hooper et al., 2004].

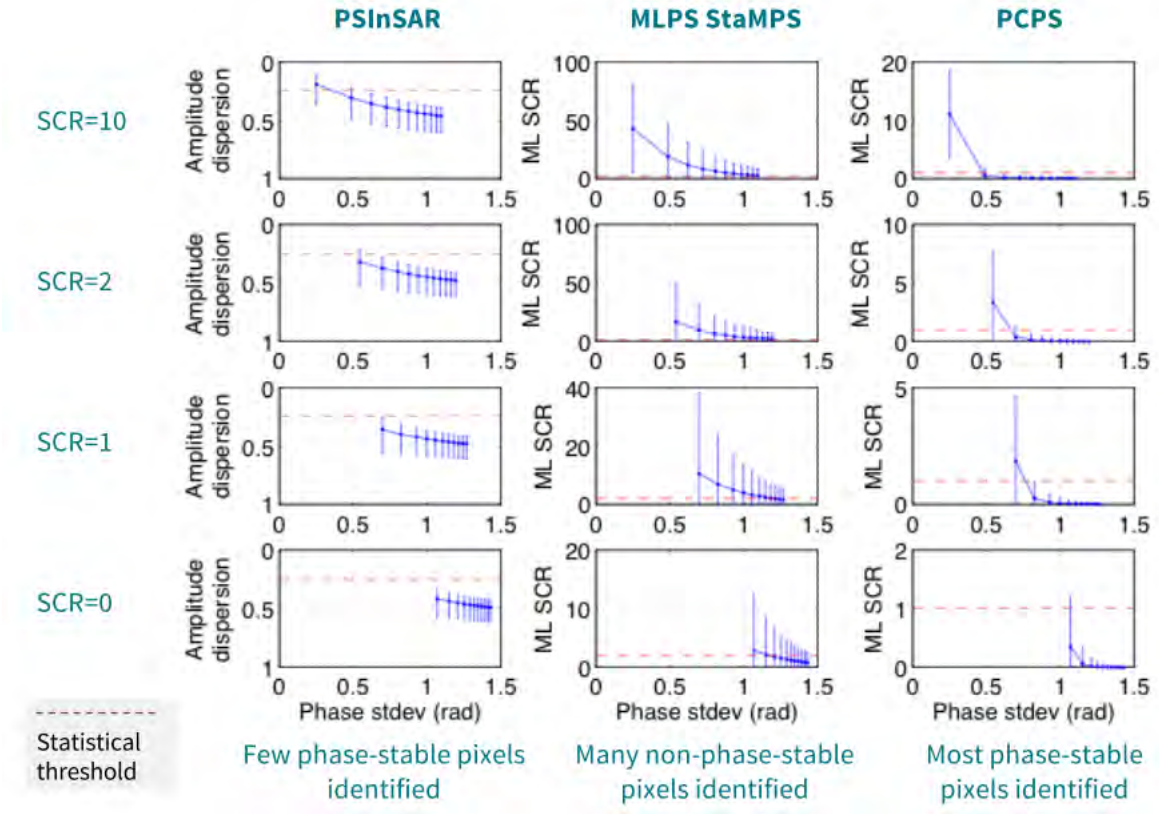

Figure 5.2: PCPS attains the best performance at identifying only pixels with low additive Gaussian noise for each level of SCR.

Using only phase information and ignoring the correlations due to small baselines, the MLPS StaMPS method identifies many pixels, including many false detections. The ML SCR estimate is also highly biased since correlations due to small baselines are essentially attributed to high SCR.

We see that the PCPS method attains the best performance at identifying only the pixels with low additive Gaussian noise for each level of SCR. The PCPS plots show a well-defined peak of maximum likelihood SCR when the phase standard deviation is low, then very low estimated SCR as phase standard deviation increases. This is because the PCPS algorithm uses both phase and amplitude information, taking into account the correlation between the SAR scenes by incorporating their spatiotemporal baselines. The steep slope in the plotted data points as phase standard deviation increases allows a well-defined SCR threshold that easily distinguishes phase-stable pixels from phase instable-pixels.

Parameter		Value
Wavelength	λ	0.0566 m
Look angle	θ	23.3°
Azimuth resolution	R_x	6.5 m
Ground range resolution	R_y	24.3 m
Critical baseline	B_{crit}	1052 m
Number of interferograms	N_{ifg}	37

Table 5.2: InSAR system parameters for ERS case study

5.6 ERS case study

To investigate the performance of the PCPS selection technique on real data, we examine a case study of ERS data in the San Francisco South Bay region. Our data set consists of 38 descending SAR acquisitions collected by the European Remote Sensing (ERS-1/2) radar satellites between May 1995 and December 2000 (Track 70, Frame 2853). Parameters of the ERS system are listed in Table 5.2. We form a stack of $N_{\text{ifg}} = 37$ single look interferograms using an acquisition from December 1997 as the common master. An example interferogram from the stack is shown in Figure 5.3.

We focus on three subareas of the interferogram, highlighted in Figure 5.4:

- Urban scene: This area of the city of Fremont consists of urban infrastructure such as roads and buildings. We expect to find the highest density of PS in this area due to many strong corner reflectors and temporally stable scatterers.
- Natural scene: This scene consists of mountainous natural terrain and vegetation, where we expect fewer PS due to few bright scatterers and faster temporal decorrelation.
- Water scene: In this area of the bay, we expect to find virtually no persistent scatterers. This area is meant to provide an estimate of the false positive PS detection rate for each of the algorithms.

We perform PS characterization and selection on the scene using the three techniques described above:

- PS-InSAR [Ferretti et al., 2001]: amplitude dispersion
- MLPS StaMPS [Shanker and Zebker, 2007]: maximum likelihood SCR using the Just-Bamler marginal phase distribution [Just and Bamler, 1994]
- PCPS: maximum likelihood SCR using the joint multipass stack phase-amplitude distribution

We first set the selection thresholds for each of the techniques according to values in the literature, shown in Table 5.3. Figure 5.5 shows the resulting selected PS mask across the whole scene using

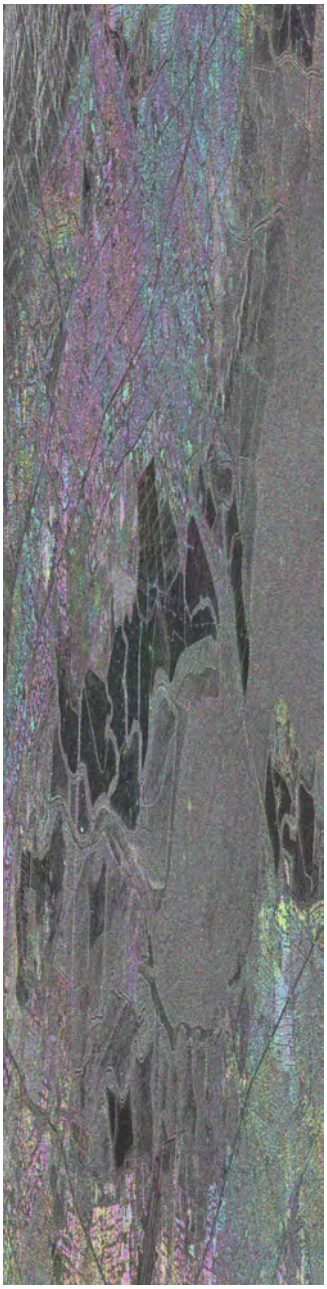

Figure 5.3: Our case study uses ERS data imaging the San Francisco Bay Area between May 1995 and December 2000 (Track 70, Frame 2853). An example interferogram formed between acquisitions from October 1997 and December 1997 is shown above.

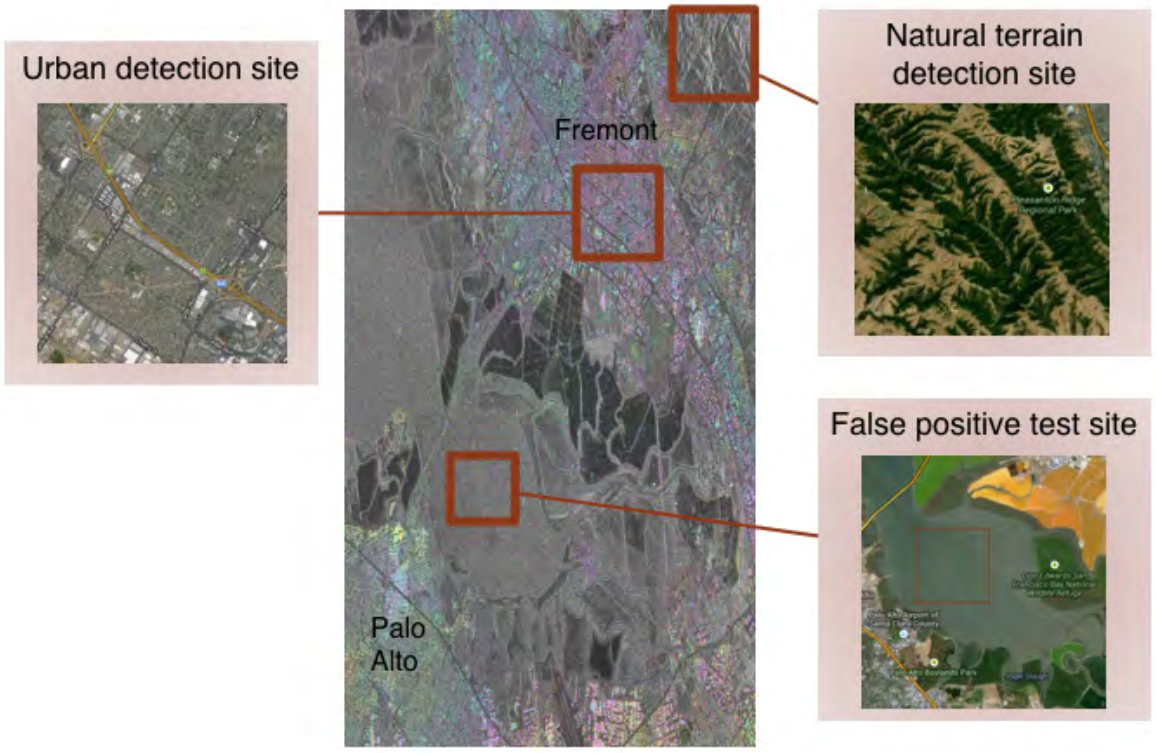

Figure 5.4: The PS selection case study focuses on three sites within the ERS interferometric scene: an urban site where a high PS density is expected; a natural terrain site where lower PS density is expected; and a water site where no PS are expected. (Map imagery: Google)

Algorithm	Initial selection threshold	PS detection rate for 1% false positive Urban	Natural
PSInSar [Ferretti et al., 2004]	$\mathcal{D}_A = 0.2$	1.25%	0.64%
MLPS StaMPS [Shanker and Zebker, 2007]	$\text{SCR}_{ML} = 2$	5.30%	1.82%
PCPS	$\text{SCR}_{ML} = 1$	6.69%	2.43%

Table 5.3: Case study results comparison

PS-InSAR, MLPS StaMPS, and PCPS, as well as the zoomed urban and natural terrain subareas. We see that amplitude dispersion detects significantly lower PS compared to either MLPS StaMPS and PCPS.

Clearly the density of selected PS depends on the selection threshold. As the selection threshold is raised, the density of selected PS pixels increases, as does the false detection rate. Because of this, the density measure alone does not provide a good measure of performance. Instead, we examine both the PS selection density as well as the estimated false detection rate, as determined by the number of selected PS in the water subarea. Figure 5.6 shows the percentage of selected PS in the urban and natural terrain areas as a function of the false positive detection rate. Ideally we would like this graph to increase as steeply as possible. PS-InSAR is capped at a threshold of $\mathcal{D}_A = 0.2$since it has been shown that it does not correlate well with phase dispersion after that point. We see that PCPS achieves a higher detection rate for any given false detection rate compared to MLPS StaMPS in both urban and natural terrain. The improvement is especially pronounced at low false positive detection rates.

Table 5.3 summarizes the PS detection rates in urban and natural terrain for 1% false positive detection rate in the water subarea. Both techniques using phase stability, MLPS StaMPS and PCPS, clearly outperform PS-InSAR. Again, we see that amplitude distribution identifies pixels with very high SCR in urban areas, but fails to find many pixels in natural terrain. In fact the performance improvement of 4-5% by PCPS aligns well with a PS-InSAR assessment made by Ferretti in 2004 [Ferretti et al., 2004]:

> Using even more advanced algorithms, it should be possible to find about five times more PS that have reliable coherence in the target frame.

5.7 StaMPS framework

We evaluate the PCPS pixel selection method in the context of a full PS pipeline. We utilize StaMPS (Stanford Method for Persistent Scatterers) [Hooper, 2006] as a framework for using PS to extract deformation measurements. StaMPS provides a processing chain for performing spatial and temporal filtering to estimate and extract various phase components from the observed interferometric pixels. A high level block diagram for the StaMPS processing chain is shown in Figure 5.7, consisting of

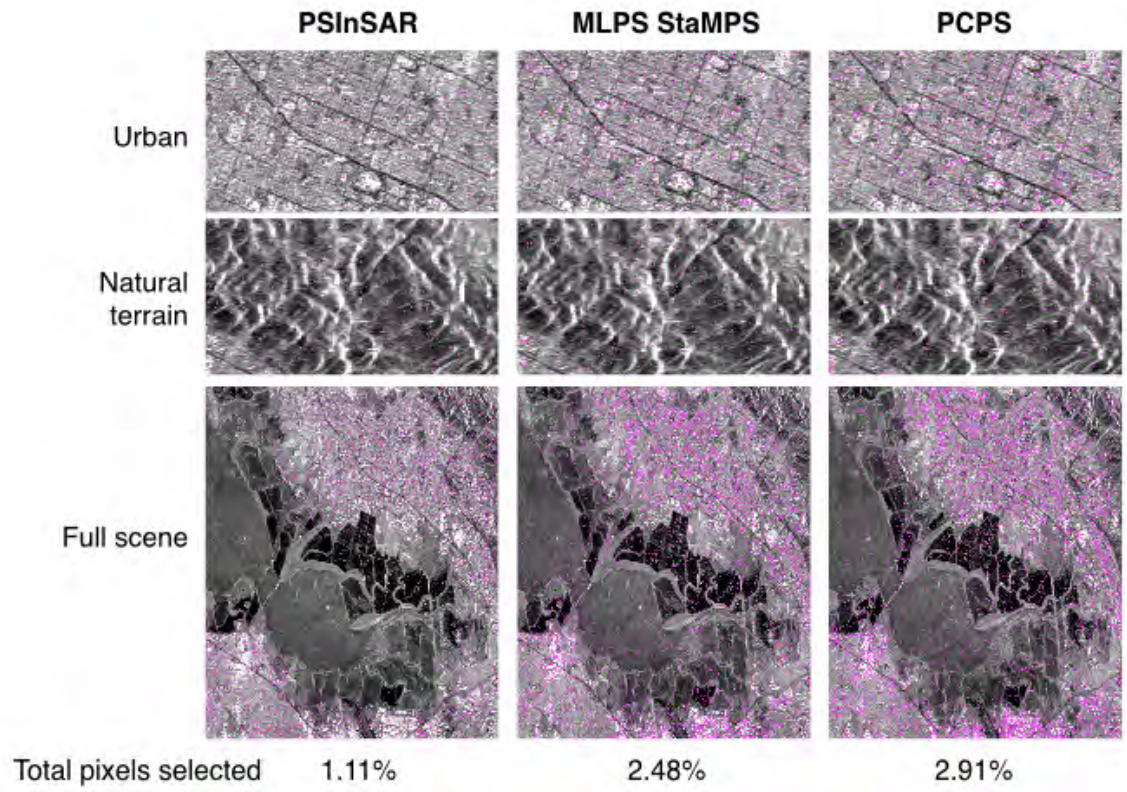

Figure 5.5: The selected PS pixels are superimposed on the SAR amplitude image. To normalize for the effect of the PS selection threshold on PS density, we set the threshold for each algorithm to attain 1% false detection rate, as determined by the number of identified PS within the water scene where no PS are expected. Compared to PS-InSAR and MLPS StaMPS, PCPS increases the density of selected PS by more than a factor of two.

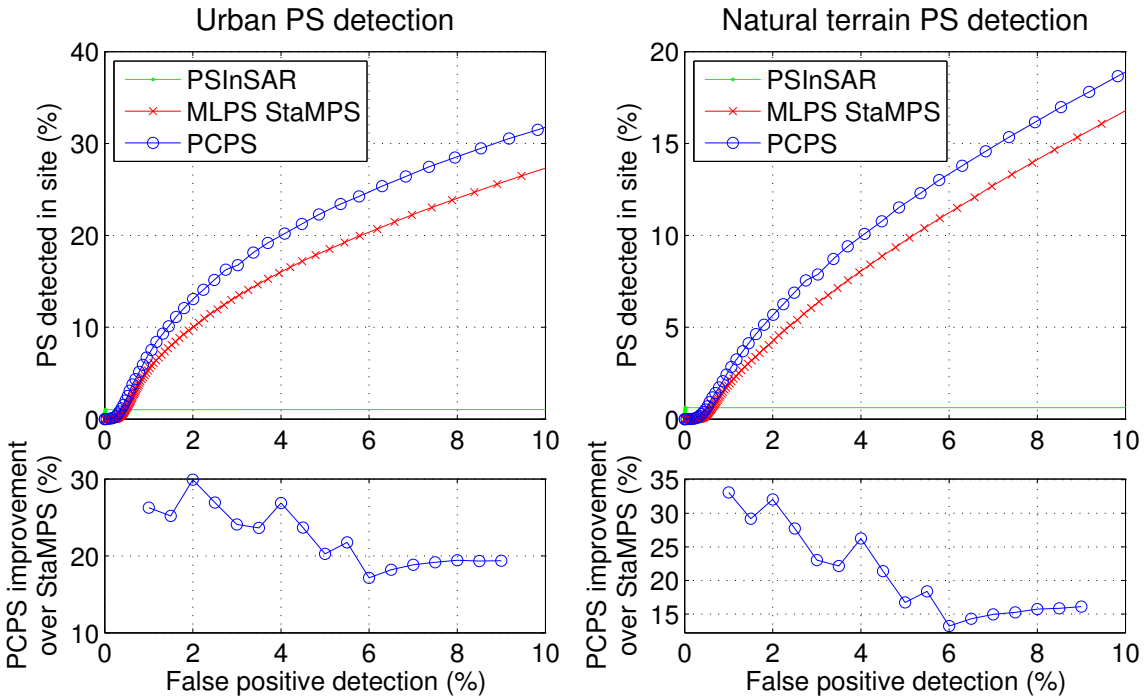

Figure 5.6: Detection versus false alarm case study results. PCPS achieves a higher detection rate for any given false detection rate compared to MLPS StaMPS in both urban and natural terrain. The improvement is especially pronounced at low false positive detection rates.

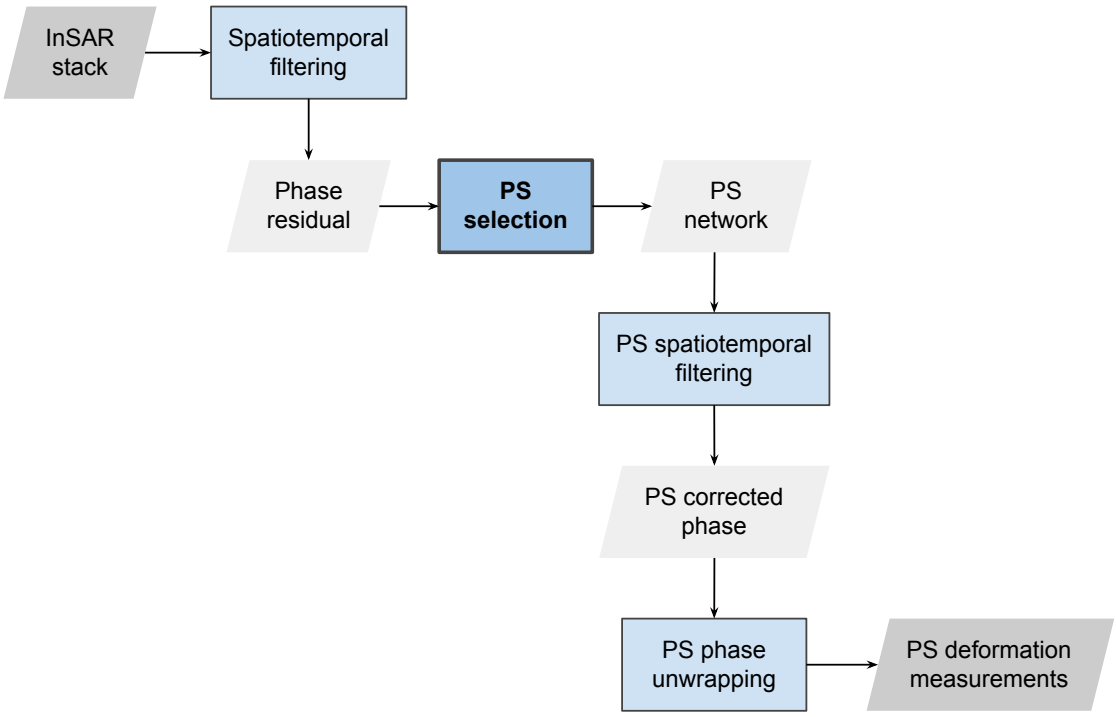

Figure 5.7: StaMPS processing chain

three general stages:

1. Spatially correlated phase terms are estimated and removed from the interferometric phase.
2. Using the residual interferometric phase due to decorrelation and thermal noise, PS pixels are selected.
3. The deformation signal is extracted from the PS network.

These stages are explained in the following subsections.

5.7.1 Phase components

The StaMPS filtering procedures are designed to estimate and extract the various phase components from the wrapped interferometric phases based on their spatial and temporal characteristics. We express the observed wrapped interferometric phase as

$$\phi_{\text{ifg},\mathbf{x},i} = (\phi_{\text{def},\mathbf{x},i} + \phi_{\text{atm},\mathbf{x},i} + \phi_{\text{err},\mathbf{x},i} + \phi_{\text{decorr},\mathbf{x},i} + \phi_{\text{noise},\mathbf{x},i}) \mod 2\pi \tag{5.22}$$

where $\mathbf{x}$ represents the pixel coordinates in interferogram i. The component phase terms and their spatiotemporal properties are described below.

Deformation ϕ_{def}

The primary signal of interest to be estimated is the phase term produced by ground deformation Δz in the radar line-of-sight:

$$\phi_{\text{def}} = -\frac{4\pi}{\lambda}\Delta z. \tag{5.23}$$

The deformation signature tends to be spatially and temporally correlated. When available, spatiotemporal deformation models may be used to constrain the estimate [Farina et al., 2006, Colesanti et al., 2003b, Colesanti et al., 2003a, Lyons and Sandwell, 2003, Vilardo et al., 2009]. However spatiotemporal frequency content is often unknown a priori, especially for high frequency deformation changes due to episodic geophysical phenomena such as earthquakes and landslides [Hooper, 2006].

Atmosphere ϕ_{atm}

Variations in signal propagation delay through the atmosphere occurs due to differences in tropospheric water vapor and total electron content [Massonnet et al., 1994]. Its contribution to the interferometric phase is typically on the order of one-tenth of a wavelength [Tarayre and Massonnet, 1996]. Tropospheric phase tends to be correlated spatially and with topography [Hanssen, 2001], but essentially temporally uncorrelated after a period of about 30 days. Its effects can be compensated using terrain data, existing weather models, or atmospheric data from other sensing modalities [Bonforte et al., 2001, Li et al., 2005].

Orbital error ϕ_{orb}

The error associated with imprecise knowledge of the satellite orbit path produces a spatially correlated phase term. The orbital error phase terms are spatially correlated and can therefore be compensated or filtered with some knowledge of the orbital geometry from other sensors or ground control points [Scharroo and Visser, 1998, Agram, 2010, Shimada, 2000].

DEM error ϕ_{err}

The phase contribution due to topography may be removed using a digital delevation map (DEM). Errors in the DEM lead to a residual phase which is correlated with the spatial baseline:

$$\phi_{\text{err}} = \frac{4\pi}{\lambda r}B(\theta)\delta h \sin(\theta) \tag{5.24}$$

Phase component	Spatial properties	Temporal properties
Deformation	Low frequency	Low frequency
Atmosphere	Low frequency	High frequency
Orbital errors	Low frequency	High frequency
DEM error	High frequency	Correlated with baseline
Noise	High frequency	High frequency
Decorrelation noise (new)	High frequency	Dependent on baseline

Table 5.4: Spectral characteristics of PS pixel phase components [Hooper, 2006]

Noise ϕ_{noise}

The original StaMPS framework lumps all noise due to scatterer decorrelation, thermal effects, phase center uncertainty, and coregistration errors under one phase term, assuming all noise is white, Gaussian, and therefore uncorrelated in space and time.

In our application of StaMPS, we separate the phase term due to decorrelation, modeling this term using the analytically derived probabilistic distributions derived in the previous chapters.

Decorrelation ϕ_{decorr}

In Chapters 3-4, we showed that the characteristics of decorrelation noise, unlike thermal noise and phase center uncertainty, are dependent on spatial and temporal baselines. In this chapter, we show how these analytical results can be applied to extend the StaMPS framework by separating out the decorrelation phase term ϕ_{decorr} from the other noise sources described above.

The phase component spectral characteristics are summarized in Table 5.4.

5.7.2 Processing steps

The steps of the StaMPS framework are described in more detail below.

1. PS candidate selection: An initial superset of PS pixels is selected using a theoretically suboptimal but computationally efficient method. This step is theoretically unnecessary but improves computational speed by narrowing the number of pixels that need to be processed.

2. Iterative estimation of spatially correlated phase terms until coherence change is below threshold.

   - Weighted spatial filtering
   - Estimate DEM error and atmospheric phase

3. PS selection: Selection of the PS pixel network is a critical step in the PS processing chain. The selected pixel network must be sufficiently dense for phase unwrapping. At the same time, the pixels must be accurately selected so that the deformation signal can be extracted

Parameter	Value
Wavelength	3.12 cm
Date range	Aug. 2010 - Sept. 2013
Number of interferograms	128
Master acquisition	10 Feb 2012
Spatial resolution	3 m × 3 m

Table 5.5: Parameters of the COSMO-SkyMed interferometric data set imaging Kilauea

and well-estimated from their phase. Hence both rates of missed detection and false positive must be sufficiently low for the PS technique to succeed. The objective of PS selection is to maximize density of selected pixels with sufficiently reliable coherence for unwrapping.

PS selection is challenging due to the other terms in the interferometric phase. Spatiotemporal filtering in the first stage of StaMPS is imperfect since the exact characteristics of the atmospheric phase and deformation signal are generally unknown a priori. The focus of this chapter is improved PS characterization and selection algorithms based on the analytical results of previous chapters.

4. Estimate and correct spatially correlated phase terms in PS network: Analytical models or other data sources are used to estimate ϕ_{err}, ϕ_{orb}, ϕ_{atm}. These terms are then removed from the observed total phase, leaving the deformation signal ϕ_{def}.

5. Phase unwrapping: Finally, the PS network phase is unwrapped to estimate the deformation signal. Phase unwrapping of the sparse network is a challenging problem that has been examined by [Costantini and Rosen, 1999].

5.8 PS deformation results

We now examine the performance of PCPS in the context of the full StaMPS processing chain. We demonstrate deformation signal measurement for a variety of radar wavelengths.

5.8.1 COSMO-SkyMed, Kilauea

Radar system

The Constellation of Small Satellites for Mediterranean basin Observation-SkyMed (COSMO-SkyMed) system consists of four satellites phased 90° apart in sun-synchronous orbit [Covello et al., 2010]. The X-band radar operated in stripmap imaging mode achieves spatial resolution of 3 m x 3 m. Due to the constellation geometry, COSMO-SkyMed can achieve a one day temporal interferometric baseline, which is able to capture quick episodic deformation events.

Table 5.5 summarizes the parameters of the COSMO-SkyMed radar system.

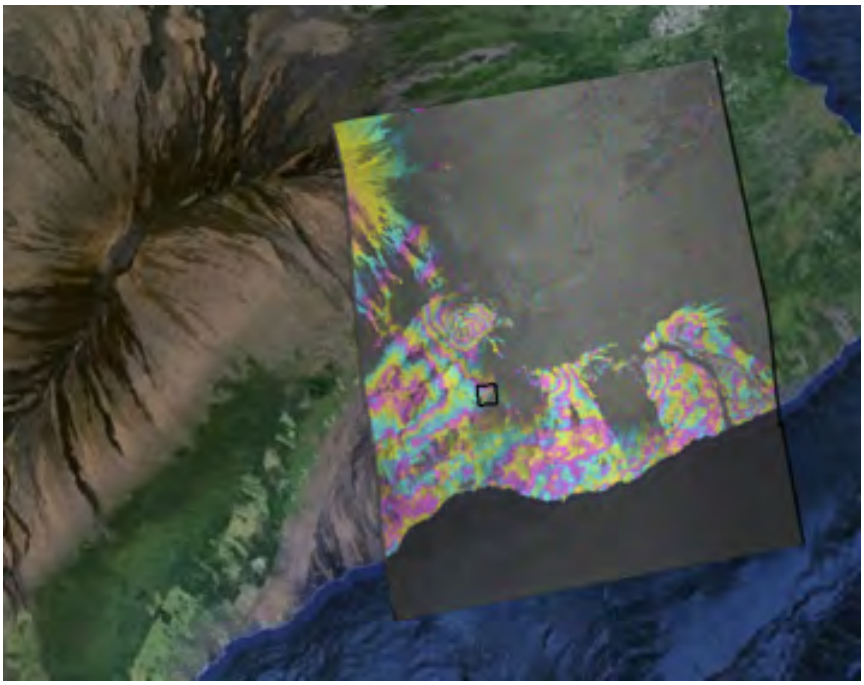

Figure 5.8: Geocoded COSMO-SkyMed interferogram imaging the southern flank of Kilauea, Hawaii. The area of PS analysis is indicated by the black rectangle.

Geophysical process

Kilauea is a shield volcano on the island of Hawai'i with two active rift zones. The south flank is characterized by seaward displacement of about 8 centimeters per year [Owen et al., 2000], with a slip-rate of approximately 21 centimeters per year [Montgomery-Brown et al., 2009]. Frequent slow slip events and earthquake swarms are evidenced by sudden crustal deformation events.

Results

We process a stack of 128 interferograms using a master acquisition from 10 Feb 2012. Figure 5.8 shows an example geocoded interferogram. For our deformation analysis, we zoom in on a 2.1 km x 2.4 km region showing evidence of a sudden deformation event in March 2011. This region is characterized by dry natural terrain and vegetation. The lack of bright scatterers results in decorrelation of much of the scene.

Figure 5.9 shows a comparison of the selected PS using PS-InSAR amplitude dispersion, MLPS StaMPS ML SCR based on the marginal phase PDF, and PCPS ML SCR based on the joint phase-amplitude PDF. As expected in natural terrain, the PS density obtained using amplitude dispersion is much lower compared to that obtained using phase statistics. The PCPS algorithm identifies 61,413 pixels compared to 42,790 for MLPS StaMPS and 2,695 for PS-InSAR.

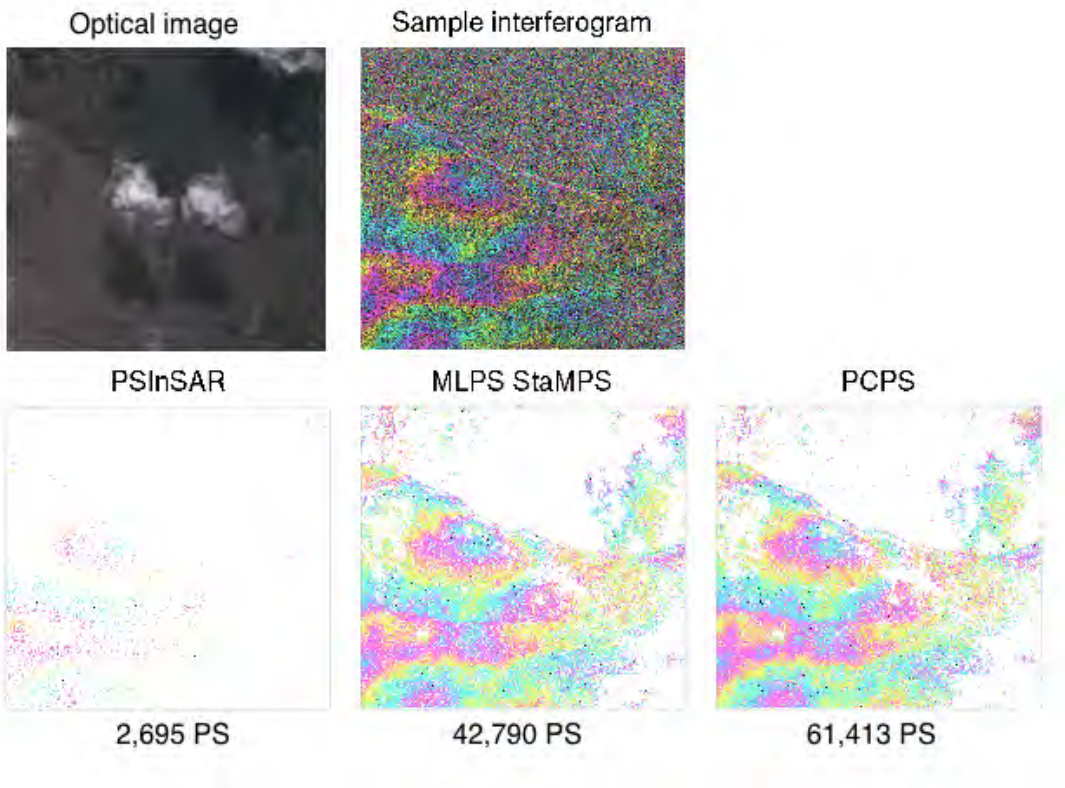

Figure 5.9: The area under analysis region is characterized by dry natural terrain and vegetation, resulting in decorrelation of much of the scene. As expected, the PS density obtained using amplitude dispersion is much lower compared to that obtained using phase statistics.

In Figure 5.10, we show the PS network wrapped phase in a time series first spanning and then excluding the event of interest. Figure 5.11 then shows the deformation times series obtained by unwrapping the phase. The deformation signature of the event is evident for the interferograms spanning March 2011. We estimate a deformation of about 2 centimeters in these scenes.

Finally, in Figure 5.12, we plot the deformation time series for a point inside the region versus a point outside. Here the 2 centimeter relative deformation is evident inside the region. The fluctuations of the deformation lie within the range likely due to variations in atmospheric delay between acquisitions.

5.8.2 ALOS, Central Valley

Radar system

The Advanced Land Observing Satellite (ALOS), operated by Japan Aerospace Exploration Agency (JAXA), carried a Phased Array L-band Synthetic Aperture Radar (PALSAR) [Kimura and Ito,

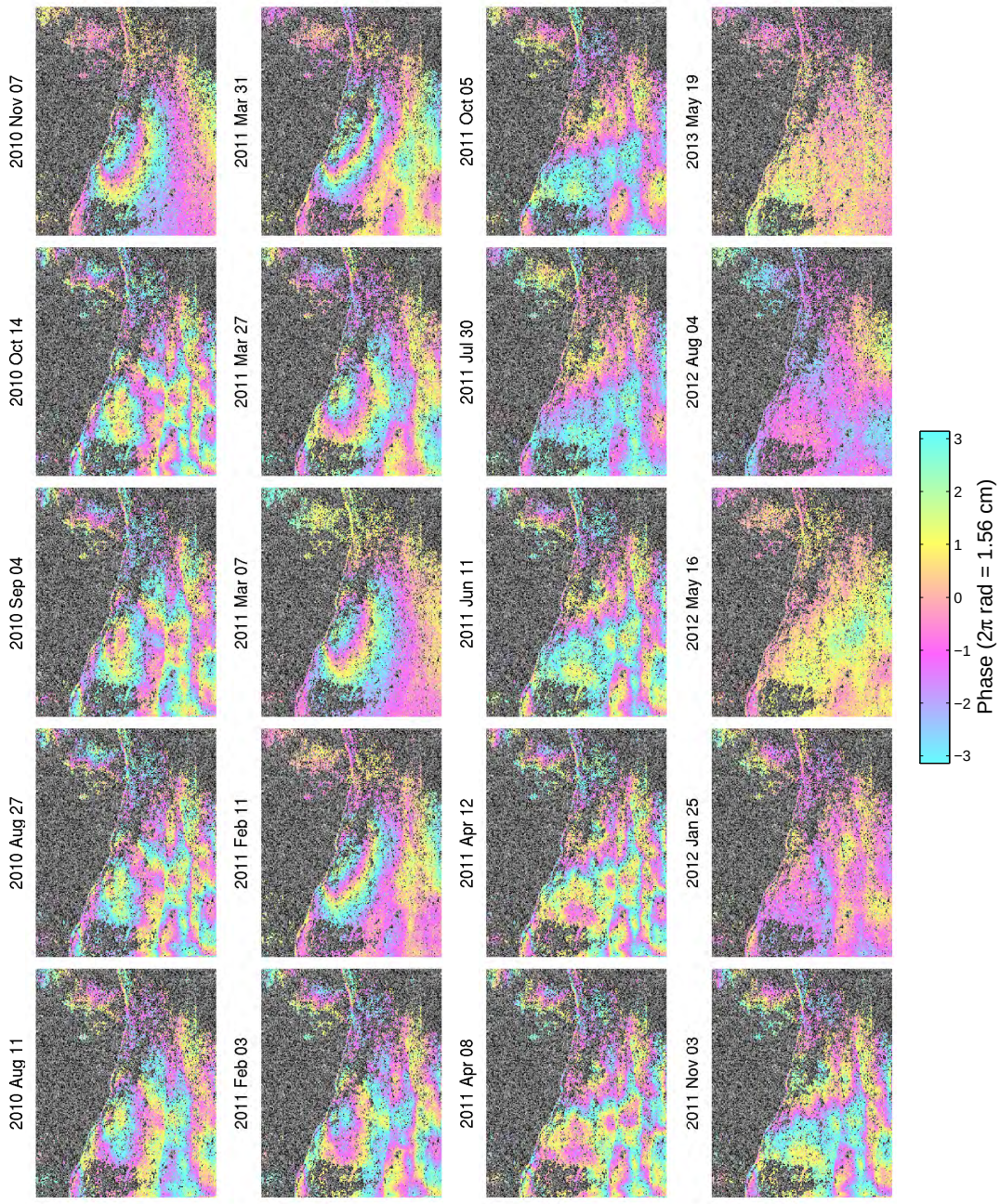

Figure 5.10: Wrapped phase time series from August 2010 to September 2013.

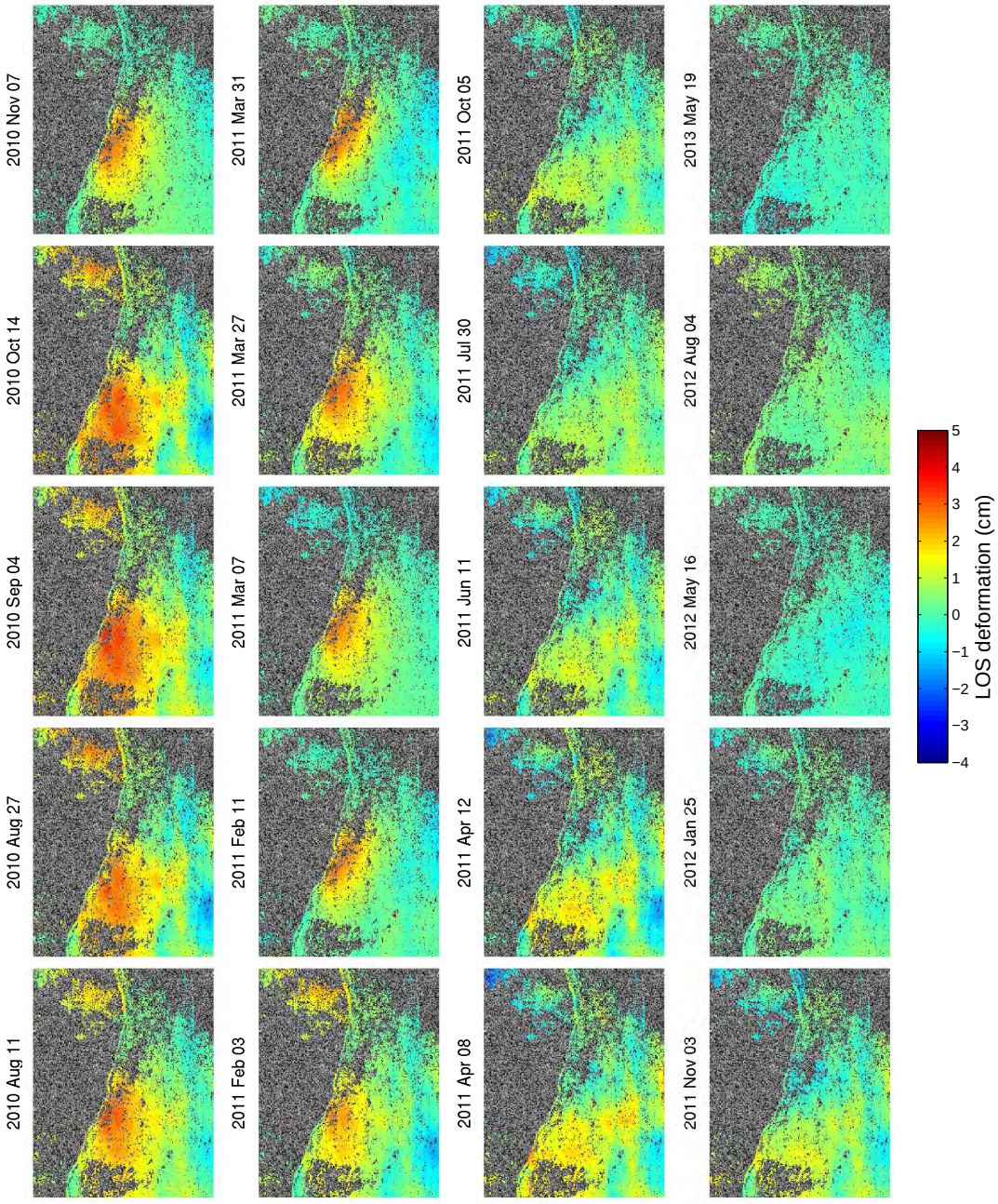

Figure 5.11: Unwrapped phase times series from August 2010 to September 2013, showing the deformation signature of a geophysical event in March 2011.

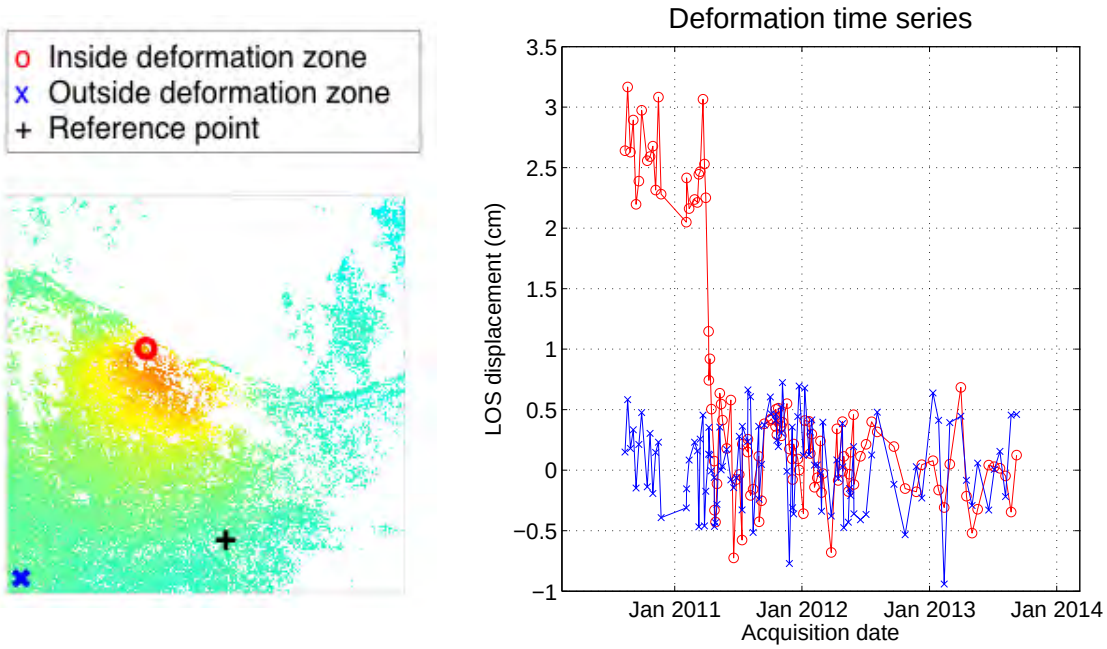

Figure 5.12: The point indicated by the red marker inside the deformation zone shows displacement in the radar line of sight of approximately 2.5 centimeters in March 2011, compared to the point outside the deformation zone, indicated by the blue marker.

2000]. The 20 centimeter wavelength gives ALOS greater immunity to temporal decorrelation effects compared to shorter wavelength InSAR systems [Zebker and Villasenor, 1992].

Parameter	Value
Wavelength	23.6 cm
Date range	June 2007 - Dec. 2010
Number of interferograms	12
Spatial resolution	20 m $\times$ 5 m

Table 5.6: ALOS parameters

Geophysical process

The Central Valley of California has been undergoing sustained land subsidence over the last two decades due to excessive groundwater pumping [Famiglietti et al., 2011, Reeves et al., 2011].

Results

The ALOS stack consists of 12 interferograms formed from a master acqusition at 23 Mar 2008. Figure 5.13 shows an example geocoded interferogram from the stack, with the area of analysis indicated by the square and magnified in Figure 5.14. The area of analysis is largely vegetated, with agricultural plot outlines visible in optical map imagery, but also includes populated infrastructure within the towns of Hanford and Kingsburg.

Figure 5.15 shows a comparison of the selected PS using PS-InSAR, MLPS StaMPS, and PCPS. PS-InSAR identifies 169,289 PS, compared to MLPS StaMPS, which identifies 360,883 PS. PCPS selects 420,355 PS. Again, the PS-InSAR method identifies many fewer PS in natural terrain due to lack of bright scatterers with high SCR.

In Figure 5.16, we show the wrapped phase. Figure 5.17 shows the results of the phase unwrapping, with the deformation signal due to subsidence. Finally, Figure 5.18 plots the deformation time series, with clearly visible deformation trend in the area of subsidence compared to outside.

5.9 Conclusion

In this chapter, we presented an improved method for maximum likelihood PS selection, based on the analysis of partially correlated persistent scatterers (PCPS) presented in Chapters 3-4. Compared to standard existing PS selection techniques such as PS-InSAR [Ferretti et al., 2004] and MLPS StaMPS [Shanker and Zebker, 2007], the new PCPS selection method presents several advantages:

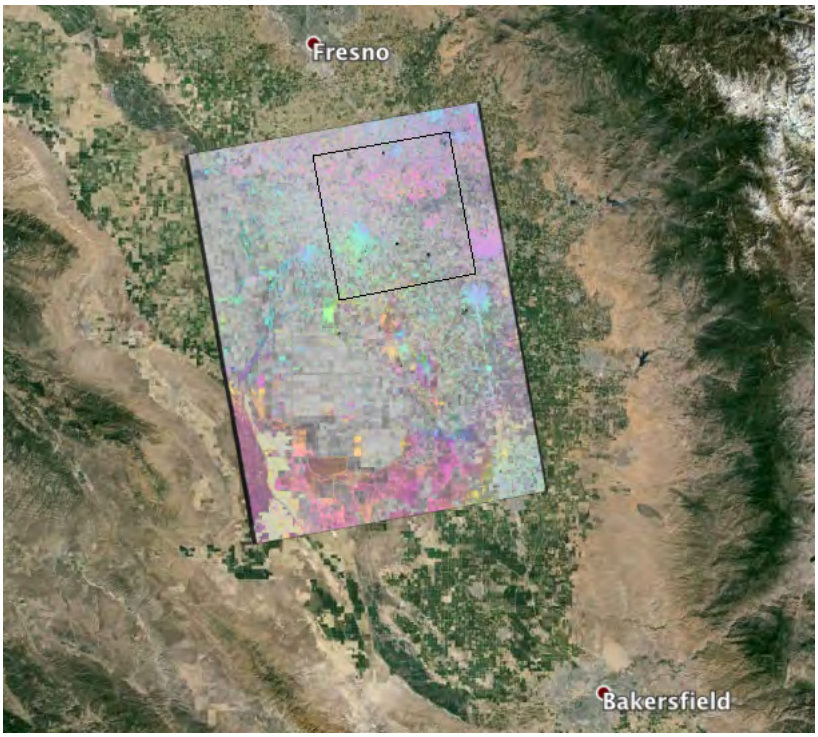

Figure 5.13: Geocoded ALOS interferogram imaging the Central Valley, California. The area of analysis, indicated by the black rectangle, is shown in detail in Figure 5.14.

Figure 5.14: Zoom in on study area. The region is largely composed of agricultural vegetation, but also includes manmade infrastructure in the towns of Hanford and Kingsburg. (Map imagery: Google)

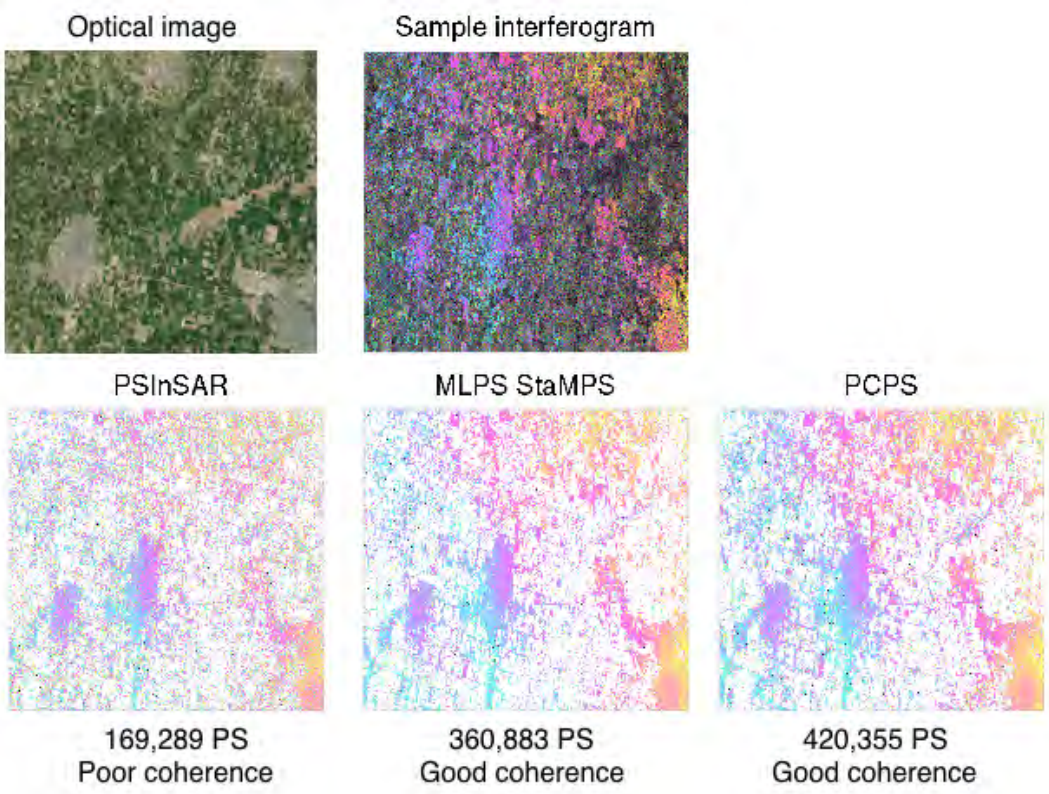

Figure 5.15: While the three PS selection techniques produce similar density of identified pixels in urban areas, the methods utilizing phase statistics (MLPS StaMPS and PCPS) identify a larger density of pixels in vegetated and agricultural areas compared to the amplitude-based PS-InSAR technique. Of the three PS algorithms, the PCPS method obtains the largest number of identified pixels overall.

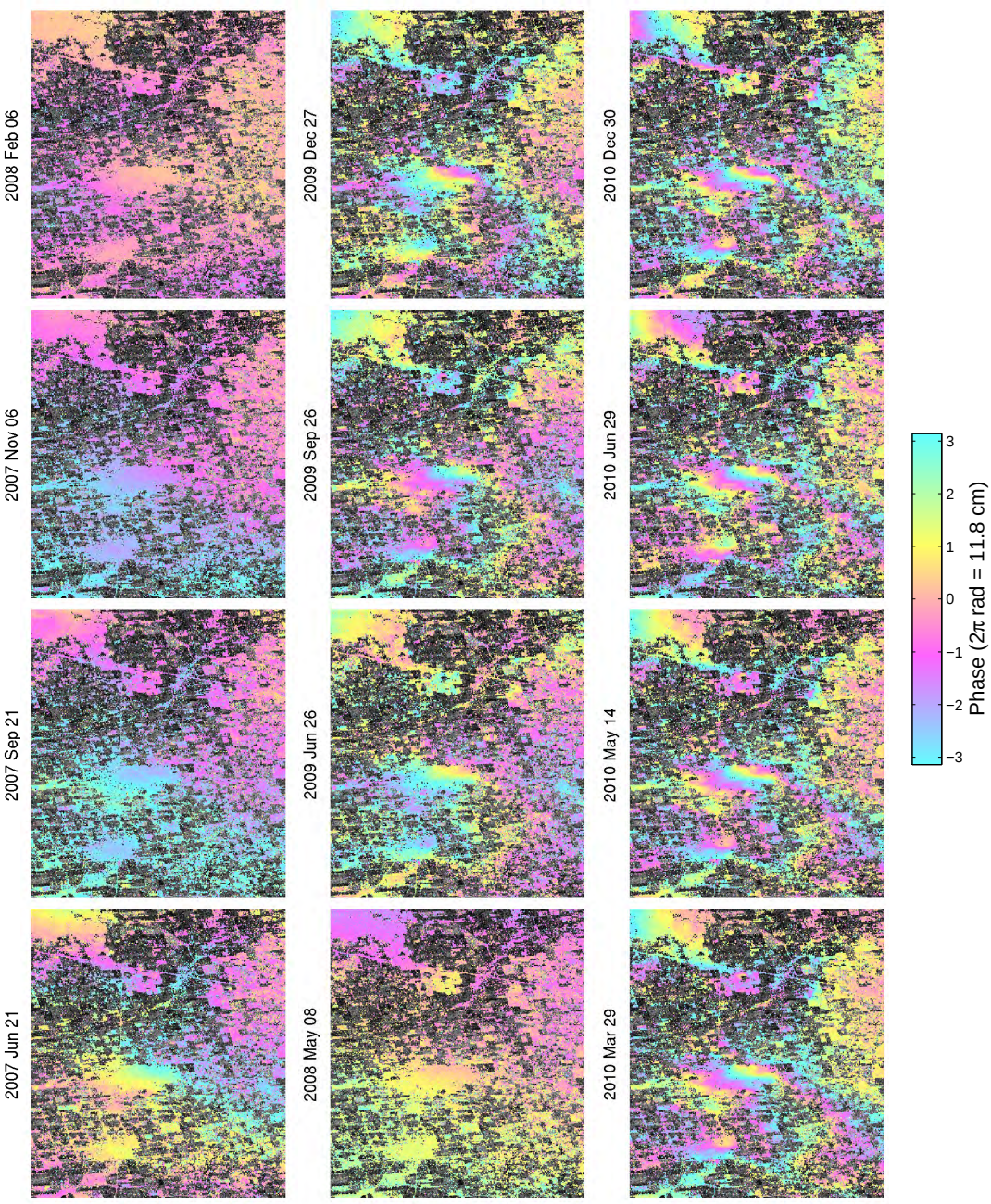

Figure 5.16: Wrapped phase time series from June 2007 to December 2010.

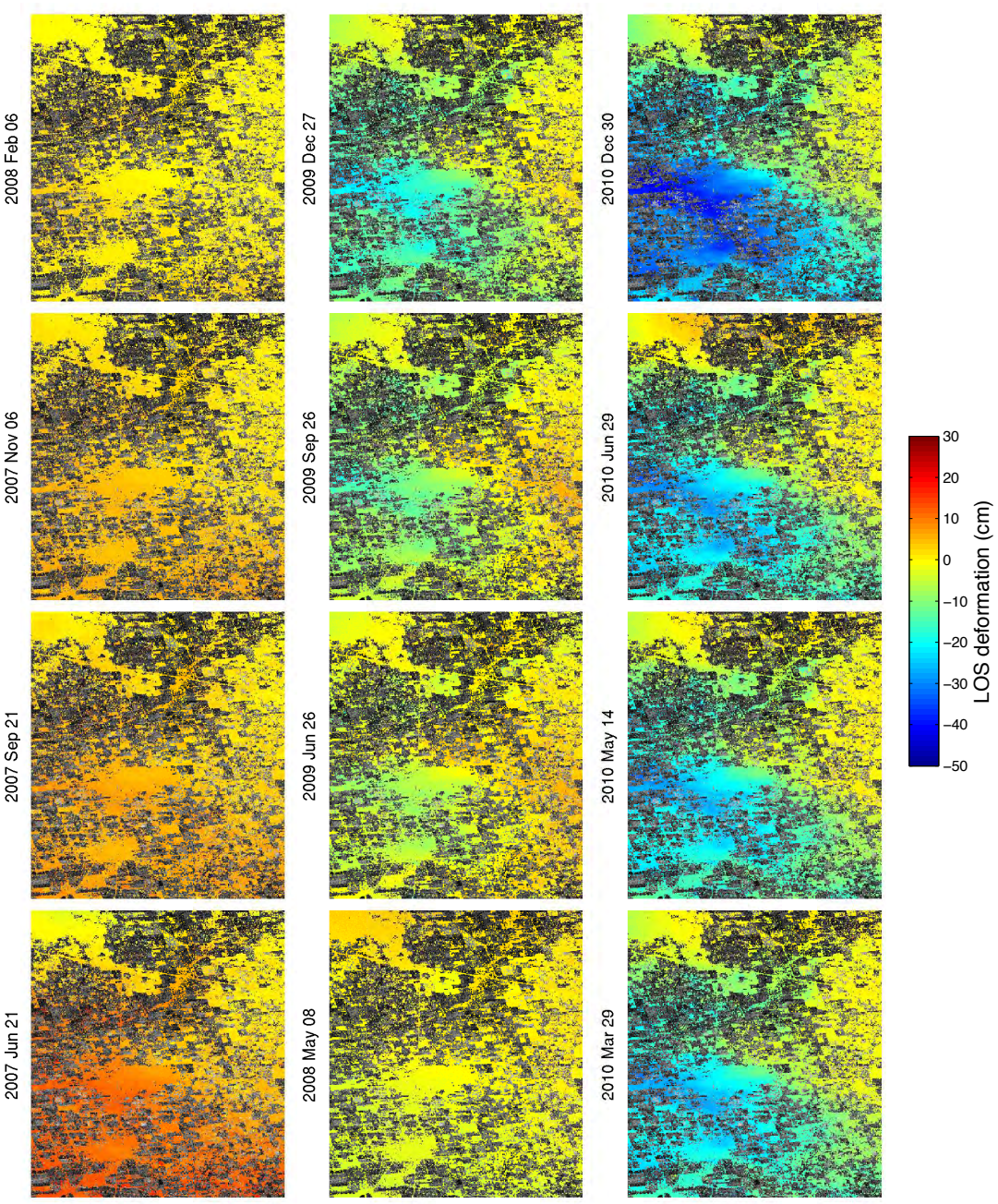

Figure 5.17: Unwrapped phase time series from June 2007 to December 2010, showing evidence of land subsidence over the timespan.

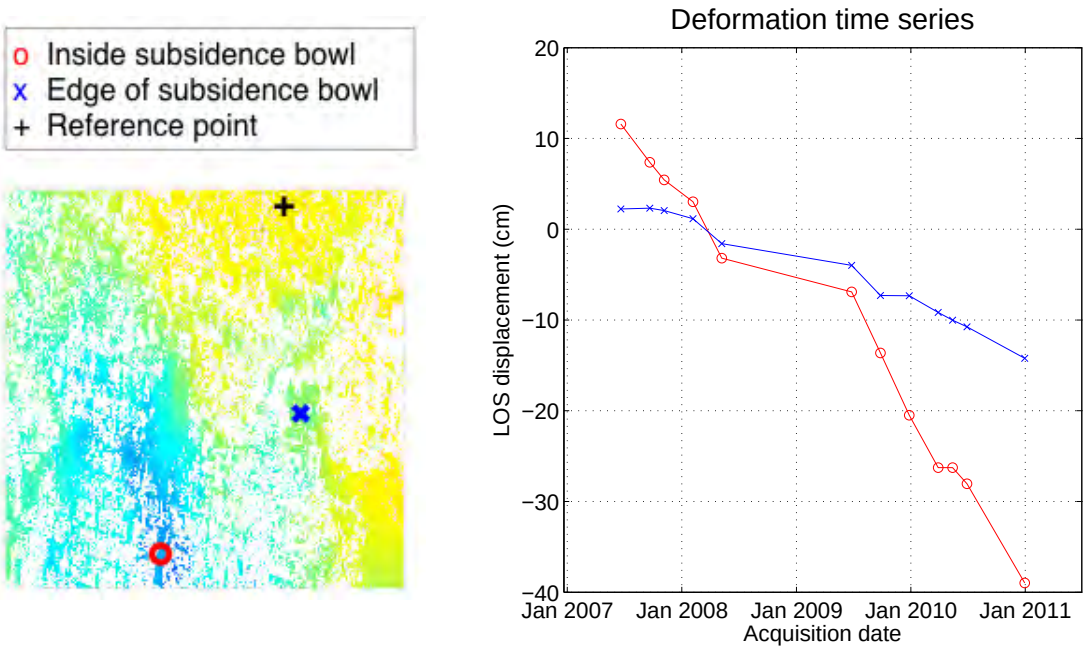

Figure 5.18: The point inside the subsidence bowl, indicated by the red marker, displays approximately 50 cm of displacement in the radar line of sight over 3.5 years, relative to the reference point indicated by the black marker. In comparison, a point on the edge of the subsidence bowl, indicated by the blue marker, displays only 16 cm of LOS displacement.

- PCPS selection accounts for correlation in the interferometric phase residual due to spatiotemporal decorrelation between passes, while existing techniques assume that the interferometric phase residual is uncorrelated between passes.
- PCPS accounts for the effect of spatiotemporal baselines on the distribution of the interferometric phase residual, while existing techniques assume that the interferometric phase residual is independent of baseline.
- PCPS combines both amplitude and phase observations, while existing techniques utilize only amplitude or only phase.

We evaluated the performance of the PCPS technique against that of PS-InSAR and MLPS StaMPS using simulated interferometric data as well as real ERS data. In order to normalize for the effect of selection threshold on the resulting PS network density, we developed a new performance evaluation methodology that sets the selection threshold for each algorithm in order to attain the same PS false detection rate. Using this methodology, we showed that PCPS identifies approximately five times as many PS pixels as PS-InSAR in urban and natural terrain, an improvement predicted in the original PS-InSAR paper [Ferretti et al., 2004].

We demonstrated that the PCPS selection technique can be applied as a modular stage within existing PS frameworks, using StaMPS [Hooper, 2006] as an example. Our results with StaMPS showed that the PCPS selection algorithm is able to extract deformation signatures across a variety of geophysical phenomena, terrains, radar wavelengths, imaging geometries, and time scales.

There are several directions to further research the design and evaluation of algorithms to select and utilize partially correlated persistent scatterers for deformation measurements. First, the fundamental performance of the PCPS selection technique requires deeper analysis. In future work, we would like to quantify the effect of selection threshold on the accuracy of PS detection and resulting deformation measurement, as well as the effect of decorrelation model mismatch on ML parameter estimation. The performance of PCPS compared to non-PS methods such as the small-baseline subset (SBAS) technique [Berardino et al., 2002] also remains to be investigated.

The integration of the PS selection stage into the broader PS algorithmic framework is another area with large potential for fundamental improvements. By utilizing information extracted from other stages of the pipeline prior to PCPS selection, and by passing on parameters estimated as a byproduct of PCPS selection, we can improve each stage of the PS framework. For example, the maximum likelihood estimates of each pixel's SCR and temporal decorrelation rate may be combined into confidence metrics for use in PS network phase unwrapping.

Finally, the studies presented in this chapter demonstrate the feasibility of the PCPS technique for deformation measurements. However we have only begun to explore the application and performance of the PCPS algorithm for real InSAR data. In future work, we plan to more thoroughly and systematically quantify the results of PCPS deformation estimation on real data against ground

truth measurements obtained through other sensing algorithms and modalities.

Chapter 6

Conclusion

6.1 Summary

Deformation measurements obtained by interferometric synthetic aperture radar play an important role in understanding the Earth's crustal processes. However conventional InSAR techniques are limited in their ability to recover a coherent deformation signal when the radar imaging geometry or surface scattering properties change significantly between radar passes. The decorrelation phenomenon leads to a loss in image spatial coherence and can render large areas of the image unsuitable for deformation measurements.

Persistent scatterer (PS) techniques can overcome these limitations by exploiting a subset of intrinsically phase-stable pixels. Identifying such pixels is a crucial component of this analysis, since phase unwrapping and subsequent deformation estimation on the spatially sparse PS network depends on both pixel selection accuracy and the network density. PS techniques have been shown to work well in urban areas with many strong, stable reflectors, but identifying an appropriate network of pixels in natural or vegetated terrain remains a challenge due to other spatiotemporally varying phase terms.

This thesis proposes an analytical and algorithmic approach to PS characterization and selection in highly decorrelated areas. There are three main focuses of this work. First, we develop the theory of partially correlated persistent scatterers, including parameterized scattering models and derived statistical characterizations. Second, we apply this theoretical analysis in order to develop an improved technique to identify and select PS pixels. Finally, we utilize the PCPS selection technique with the StaMPS (Stanford Method for Persistent Scatterers) framework in order to measure crustal deformation from a variety of InSAR data sets.

In Chapter 3, we presented a new radar scattering model that relates the PCPS signal moments to physical properties of the surface. From this scattering model, we derived a new analytic model

for the spatiotemporal decorrelation of persistent scatterers as a function of baseline and signal-to-clutter ratio (SCR). This model quantifies the partial correlation of persistent scatterer pixels over large baselines, providing a means to characterize and compare the phase stability of PS, non-PS, and ideal point scatterer pixels.

In Chapter 4, we presented a more complete statistical characterization of the PS decorrelation phase statistics, derived from PS scattering principles. We used the PCPS backscattering model and interferometric stack system model in Chapter 3 to derive the joint phase-amplitude distribution for the entire stack of pixels as a function of SCR and spatial baseline. We show that the new PS backscatter model and resulting distribution fit simulated data better than previous analysis.

In Chapter 5, we presented an algorithm for improved PS selection based on the analysis of the previous chapters. This method optimally combines the full stack of phase and amplitude observations, as well as information about the spatiotemporal baselines. We performed a case study demonstrating the improved performance in terms of PS identification and false detection compared other PS selection methods. Using the general StaMPS framework for PS deformation measurement, we demonstrated that the PCPS selection algorithm can obtain deformation measurements for a variety of radar data sets.

6.2 Future work

This thesis opens several directions for future exploration and improvement in all areas of PCPS research: analysis and theory, algorithm development, and application. A few of these directions are summarized below.

6.2.1 Analytic

The material presented here assumed one master SAR image with N slave images; i.e. the interferometric stack was formed as $\mathbf{z} = u_0\overline{\mathbf{u}}$. We can extend the analysis to every possible master-slave pair by forming the interferometric stack as

$$\mathbf{Z} = \mathbf{u}\overline{\mathbf{u}^T}. \tag{6.1}$$

We also simplified our analysis by first assuming a time-invariant backscatter function $f(x, y, t) = f(x, y)$ and deriving the corresponding PDFs for spatial decorrelation. Temporal decorrelation was then incorporated directly into the entries of the covariance matrix $\mathbf{\Gamma}$. We can remove this simplifying assumption in the future by modeling the temporal change in the backscatter function $f(x, y, t)$.

6.2.2 Algorithmic

The fundamental performance of the PCPS selection technique requires deeper analysis. In future work, we would like to quantify the effect of selection threshold on the accuracy of PS detection and resulting deformation measurement, as well as the effect of decorrelation model mismatch on ML parameter estimation. The performance of PCPS compared to non-PS methods such as the small-baseline subset (SBAS) technique [Berardino et al., 2002] also remains to be investigated.

The integration of the PS selection stage into the broader PS algorithmic framework is another area with large potential for fundamental improvements. By utilizing information extracted from other stages of the pipeline prior to PCPS selection, and by passing on parameters estimated as a byproduct of PCPS selection, we can improve each stage of the PS framework. For example, the maximum likelihood estimates of each pixel's SCR and temporal decorrelation rate may be combined into confidence metrics for use in PS network phase unwrapping.

6.2.3 Application

We have only begun to explore the application and performance of the PCPS algorithm for real InSAR data. In future work, we plan to more thoroughly and systematically quantify the results of PCPS deformation estimation on real data against ground truth measurements obtained through other sensing algorithms and modalities.

Beyond deformation measurement, PCPS analysis can also be used for applications such as change detection. The details of extending this analysis to such applications are to be developed.

6.3 Closing remarks

In this thesis, we presented new theory and techniques for generalized PS analysis based on partially correlated persistent scatterers (PCPS): those that are non-ideal but stable enough for deformation time series measurement in largely decorrelated areas. We derived a new physically-based method for modeling spatiotemporal decorrelation, as well as a comprehensive statistical characterization of the resulting interferometric pixels. We showed that these analytical results lay a theoretical foundation for PCPS algorithm development.

Based on this analysis, we designed a more reliable PS selection technique that combines the full set of interferometric observations as a function of their acquisition intervals. The PCPS technique achieves a better trade-off between pixel selection accuracy and network density compared to other PS identification methods. Finally, we presented examples of deformation measurements obtained using PCPS analysis. These results demonstrate that through improved statistical characterization, the PCPS technique attains reliable deformation measurements for a variety of wavelengths, terrain, and geophysical processes.

The main contributions of this thesis thus lie in the analysis, algorithms, and application of PCPS techniques. We hope that this work opens the door to future research on PCPS and improvement in InSAR deformation measurement technology.

Bibliography

[Abramowitz and Stegun, 1972] Abramowitz, M. and Stegun, I. A. (1972). *Handbook of Mathematical Functions with Formulas, Graphs and Mathematical Tables*. Dover Publications, Inc., 2 edition.

[Adam et al., 2003] Adam, N., Kampes, B., Eineder, M., Worawattanamateekul, J., and Kircher, M. (2003). The development of a scientific permanent scatterer system. In *ISPRS Workshop High Resolution Mapping from Space, Hannover, Germany*, volume 2003, page 6.

[Agram, 2010] Agram, P. S. (2010). *Persistent scatterer interferometry in natural terrain*. PhD thesis, Stanford University.

[Ahmed et al., 2008] Ahmed, R., Siqueira, P., Hensley, S., Chapman, B., and Bergen, K. (2008). Temporal decorrelation studies for vegetation parameter estimation with space-borne radars. In *IEEE International Geoscience and Remote Sensing Symposium (IGARSS) 2008*, volume 2, pages II–481–II–484.

[Ahmed et al., 2011] Ahmed, R., Siqueira, P., Hensley, S., Chapman, B., and Bergen, K. (2011). A survey of temporal decorrelation from spaceborne L-band repeat-pass InSAR. *Remote Sensing of Environment*, 115(11):2887–2896.

[Amelung et al., 1999] Amelung, F., Galloway, D. L., Bell, J. W., Zebker, H. A., and Laczniak, R. J. (1999). Sensing the ups and downs of Las Vegas: InSAR reveals structural control of land subsidence and aquifer-system deformation. *Geology*, 27(6):483–486.

[Amelung et al., 2000] Amelung, F., Jónsson, S., Zebker, H., and Segall, P. (2000). Widespread uplift and 'trapdoor' faulting on Galápagos volcanoes observed with radar interferometry. *Nature*, 407(6807):993–996.

[Askne and Smith, 1997] Askne, J. and Smith, G. (1997). Forest InSAR decorrelation and classification properties. In Guyenne, T. D. and Danesy, D., editors, *ERS SAR Interferometry*, volume 406 of *ESA Special Publication*, page 95.

[Ausherman et al., 1984] Ausherman, D. A., Kozma, A., Walker, J. L., Jones, H. M., and Poggio, E. C. (1984). Developments in radar imaging. *IEEE Transactions on Aerospace and Electronic Systems*, 4(AES-20):363–400.

[Bamler and Hartl, 1998] Bamler, R. and Hartl, P. (1998). Synthetic aperture radar interferometry. *Inverse Problems*, 14(4).

[Berardino et al., 2002] Berardino, P., Fornaro, G., Lanari, R., and Sansosti, E. (2002). A new algorithm for surface deformation monitoring based on small baseline differential SAR interferograms. *IEEE Transactions on Geoscience and Remote Sensing*, 40(11):2375–2383.

[Bonforte et al., 2001] Bonforte, A., Ferretti, A., Prati, C., Puglisi, G., and Rocca, F. (2001). Calibration of atmospheric effects on SAR interferograms by GPS and local atmosphere models: first results. *Journal of Atmospheric and Solar-Terrestrial Physics*, 63(12):1343 – 1357.

[Brown, 1999] Brown, L. (1999). *Technical and Military Imperatives: A Radar History of World War 2*. CRC Press.

[Champenois et al., 2012] Champenois, J., Fruneau, B., Pathier, E., Deffontaines, B., Lin, K.-C., and Hu, J.-C. (2012). Monitoring of active tectonic deformations in the Longitudinal Valley (Eastern Taiwan) using persistent scatterer InSAR method with ALOS PALSAR data. *Earth and Planetary Science Letters*, 337:144–155.

[Chen and Zebker, 2002] Chen, C. and Zebker, H. (2002). Phase unwrapping for large SAR interferograms: statistical segmentation and generalized network models. *Geoscience and Remote Sensing, IEEE Transactions on*, 40(8):1709–1719.

[Colesanti et al., 2003a] Colesanti, C., Ferretti, A., Novali, F., Prati, C., and Rocca, F. (2003a). SAR monitoring of progressive and seasonal ground deformation using the permanent scatterers technique. *IEEE Transactions on Geoscience and Remote Sensing*, 41(7):1685–1701.

[Colesanti et al., 2003b] Colesanti, C., Ferretti, A., Prati, C., and Rocca, F. (2003b). Monitoring landslides and tectonic motions with the permanent scatterers technique. *Engineering Geology*, 68(1):3–14.

[Costantini, 1998] Costantini, M. (1998). A novel phase unwrapping method based on network programming. *Geoscience and Remote Sensing, IEEE Transactions on*, 36(3):813–821.

[Costantini et al., 2008] Costantini, M., Falco, S., Malvarosa, F., and Minati, F. (2008). A new method for identification and analysis of persistent scatterers in series of SAR images. In *Geoscience and Remote Sensing Symposium, 2008. IGARSS 2008. IEEE International*, volume 2, pages II–449. IEEE.

[Costantini and Rosen, 1999] Costantini, M. and Rosen, P. A. (1999). A generalized phase unwrapping approach for sparse data. In *Geoscience and Remote Sensing Symposium, 1999. IGARSS'99 Proceedings. IEEE 1999 International*, volume 1, pages 267–269. IEEE.

[Covello et al., 2010] Covello, F., Battazza, F., Coletta, A., Lopinto, E., Fiorentino, C., Pietranera, L., Valentini, G., and Zoffoli, S. (2010). COSMO-SkyMed an existing opportunity for observing the Earth. *Journal of Geodynamics*, 49(3):171–180.

[Crosetto et al., 2015] Crosetto, M., Monserrat, O., Cuevas-González, M., Devanthéry, N., and Crippa, B. (2015). Persistent scatterer interferometry: A review. *ISPRS Journal of Photogrammetry and Remote Sensing*.

[Crosetto et al., 2009] Crosetto, M., Monserrat, O., Jungner, A., and Crippa, B. (2009). Persistent scatterer interferometry: Potential and limits. In *Proceedings of the 2009 ISPRS Workshop on High-Resolution Earth Imaging for Geospatial Information, Hannover, Germany*, volume 25.

[Daniels, 2004] Daniels, D. J. (2004). *Ground penetrating radar*, volume 1. Iet.

[Droitcour et al., 2001] Droitcour, A., Lubecke, V., Lin, J., and Boric-Lubecke, O. (2001). A microwave radio for Doppler radar sensing of vital signs. In *Microwave Symposium Digest, 2001 IEEE MTT-S International*, volume 1, pages 175–178. IEEE.

[Elachi et al., 1990] Elachi, C., Kuga, Y., McDonald, K., Sarabandi, K., Ulaby, F., Whitt, M., Zebker, H., and van Zyl, J. (1990). *Radar polarimetry for geoscience applications*. Norwood, MA (USA); Artech House Inc.

[Emardson et al., 2003] Emardson, T., Simons, M., and Webb, F. (2003). Neutral atmospheric delay in interferometric synthetic aperture radar applications: Statistical description and mitigation. *Journal of Geophysical Research*, 108(B5):2231.

[Famiglietti et al., 2011] Famiglietti, J. S., Lo, M., Ho, S. L., Bethune, J., Anderson, K. J., Syed, T. H., Swenson, S. C., de Linage, C. R., and Rodell, M. (2011). Satellites measure recent rates of groundwater depletion in California's Central Valley. *Geophysical Research Letters*, 38(3).

[Farina et al., 2006] Farina, P., Colombo, D., Fumagalli, A., Marks, F., and Moretti, S. (2006). Permanent scatterers for landslide investigations: outcomes from the ESA-SLAM project. *Engineering Geology*, 88(3):200–217.

[Ferretti et al., 2005] Ferretti, A., Bianchi, M., Prati, C., and Rocca, F. (2005). Higher-order permanent scatterers analysis. *EURASIP Journal on Applied Signal Processing*, 20:3231–3242.

[Ferretti et al., 2011] Ferretti, A., Fumagalli, A., Novali, F., Prati, C., Rocca, F., and Rucci, A. (2011). A new algorithm for processing interferometric data-stacks: SqueeSAR. *Geoscience and Remote Sensing, IEEE Transactions on*, 49(9):3460–3470.

[Ferretti et al., 2004] Ferretti, A., Novali, F., Bürgmann, R., Hilley, G., and Prati, C. (2004). InSAR permanent scatterer analysis reveals ups and downs in San Francisco Bay area. *Eos, Transactions American Geophysical Union*, 85(34):317.

[Ferretti et al., 2001] Ferretti, A., Prati, C., and Rocca, F. (2001). Permanent scatterers in SAR interferometry. *IEEE Transactions on Geoscience and Remote Sensing*, 39(1):8–20.

[Gabriel et al., 1989] Gabriel, A., Goldstein, R., and Zebker, H. (1989). Mapping small elevation changes over large areas: Differential radar interferometry. *Journal of Geophysical Research*, 94(B7):9183–9191.

[Hanssen, 2001] Hanssen, R. F. (2001). *Radar interferometry: data interpretation and error analysis*, volume 2. Springer Science & Business Media.

[Hoen et al., 2000] Hoen, E. W., Zebker, H., et al. (2000). Penetration depths inferred from interferometric volume decorrelation observed over the Greenland ice sheet. *Geoscience and Remote Sensing, IEEE Transactions on*, 38(6):2571–2583.

[Hoffmann et al., 2001] Hoffmann, J., Zebker, H. A., Galloway, D. L., and Amelung, F. (2001). Seasonal subsidence and rebound in Las Vegas Valley, Nevada, observed by synthetic aperture radar interferometry. *Water Resources Research*, 37(6):1551–1566.

[Hooper, 2006] Hooper, A. (2006). *Persistent scatter radar interferometry for crustal deformation studies and modeling of volcanic deformation*. PhD thesis, Stanford University.

[Hooper et al., 2007] Hooper, A., Segall, P., and Zebker, H. (2007). Persistent scatterer interferometric synthetic aperture radar for crustal deformation analysis, with application to Volcán Alcedo, Galápagos. *Journal of Geophysical Research: Solid Earth*, 112(B7).

[Hooper et al., 2004] Hooper, A., Zebker, H., Segall, P., and Kampes, B. (2004). A new method for measuring deformation on volcanoes and other natural terrains using InSAR persistent scatterers. *Geophysical Research Letters*, 31(23):L23611.

[Jol, 2008] Jol, H. M. (2008). *Ground penetrating radar theory and applications*. Elsevier.

[Jónsson et al., 2002] Jónsson, S., Zebker, H., Segall, P., and Amelung, F. (2002). Fault slip distribution of the 1999 Mw 7.1 Hector Mine, California, earthquake, estimated from satellite radar and GPS measurements. *Bulletin of the Seismological Society of America*, 92(4):1377–1389.

[Just and Bamler, 1994] Just, D. and Bamler, R. (1994). Phase statistics of interferograms with applications to synthetic aperture radar. *Applied Optics*, 33(20):4361–4368.

[Kampes, 2005] Kampes, B. M. (2005). *Displacement parameter estimation using permanent scatterer interferometry*. PhD thesis, Delft University of Technology.

[Kampes and Adam, 2006] Kampes, B. M. and Adam, N. (2006). The STUN algorithm for persistent scatterer interferometry. In *Fringe 2005 Workshop*, volume 610, page 16.

[Kim et al., 2002] Kim, K.-T., Seo, D.-K., and Kim, H.-T. (2002). Efficient radar target recognition using the MUSIC algorithm and invariant features. *Antennas and Propagation, IEEE Transactions on*, 50(3):325–337.

[Kim and Ling, 2009] Kim, Y. and Ling, H. (2009). Human activity classification based on micro-Doppler signatures using a support vector machine. *Geoscience and Remote Sensing, IEEE Transactions on*, 47(5):1328–1337.

[Kimura and Ito, 2000] Kimura, H. and Ito, N. (2000). ALOS/PALSAR: The Japanese second-generation spaceborne SAR and its applications. In *Proc. SPIE*, volume 4152, pages 110–119.

[K.Li and Goldstein, 1990] K.Li, F. and Goldstein, R. (1990). Studies of multibaseline spaceborne interferometric synthetic aperture radars. *Geoscience and Remote Sensing, IEEE Transactions on*, 28(1):88–97.

[Lauknes et al., 2010] Lauknes, T., Shanker, A. P., Dehls, J., Zebker, H., Henderson, I., and Larsen, Y. (2010). Detailed rockslide mapping in northern Norway with small baseline and persistent scatterer interferometric SAR time series methods. *Remote Sensing of Environment*, 114(9):2097–2109.

[Lavalle et al., 2012] Lavalle, M., Simard, M., and Hensley, S. (2012). A temporal decorrelation model for polarimetric radar interferometers. *IEEE Transactions on Geoscience and Remote Sensing*, 50(7):2880–2888.

[Lee, 1981] Lee, J.-S. (1981). Speckle analysis and smoothing of synthetic aperture radar images. *Computer Graphics and Image Processing*, 17(1):24–32.

[Lee et al., 2013] Lee, S.-K., Kugler, F., Papathanassiou, K., and Hajnsek, I. (2013). Quantification of temporal decorrelation effects at L-band for polarimetric SAR interferometry applications. *Selected Topics in Applied Earth Observations and Remote Sensing, IEEE Journal of*, 6(3):1351–1367.

[Li et al., 2009] Li, C., Cummings, J., Lam, J., Graves, E., and Wu, W. (2009). Radar remote monitoring of vital signs. *Microwave Magazine, IEEE*, 10(1):47–56.

[Li et al., 2005] Li, Z., Muller, J.-P., Cross, P., and Fielding, E. J. (2005). Interferometric synthetic aperture radar (InSAR) atmospheric correction: GPS, moderate resolution imaging spectroradiometer (MODIS), and InSAR integration. *Journal of Geophysical Research: Solid Earth*, 110(B3).

[Lien et al., 2016] Lien, J., Gillian, N., Karagozler, M. E., Amihood, P., Schwesig, C., Olson, E., Raja, H., and Poupyrev, I. (2016). Soli: ubiquitous gesture sensing with millimeter wave radar. *ACM Transactions on Graphics (TOG)*, 35(4):142.

[Liu et al., 2011] Liu, L., Popescu, M., Skubic, M., Rantz, M., Yardibi, T., and Cuddihy, P. (2011). Automatic fall detection based on Doppler radar motion signature. In *Pervasive Computing Technologies for Healthcare (PervasiveHealth), 2011 5th International Conference on*, pages 222–225. IEEE.

[Lyons and Sandwell, 2003] Lyons, S. and Sandwell, D. (2003). Fault creep along the southern San Andreas from interferometric synthetic aperture radar, permanent scatterers, and stacking. *Journal of Geophysical Research: Solid Earth (1978–2012)*, 108(B1).

[Massonnet et al., 1994] Massonnet, D., Feigl, K., Rossi, M., and Adragna, F. (1994). Radar interferometric mapping of deformation in the year after the Landers earthquake. *Nature*, 369(6477):227–230.

[Massonnet and Feigl, 1995] Massonnet, D. and Feigl, K. L. (1995). Discrimination of geophysical phenomena in satellite radar interferograms. *Geophysical research letters*, 22(12):1537–1540.

[Massonnet et al., 1997] Massonnet, D., Holzer, T., and Vadon, H. (1997). Land subsidence caused by the East Mesa geothermal field, California, observed using SAR interferometry. *Geophysical Research Letters*, 24(8):901–904.

[Massonnet et al., 1993] Massonnet, D., Rossi, M., Carmona, C., Adragna, F., Peltzer, G., Feigl, K., and Rabaute, T. (1993). The displacement field of the Landers earthquake mapped by radar interferometry. *Nature*, 364(6433):138–142.

[Meng and Sandwell, 2010] Meng, W. and Sandwell, D. (2010). Decorrelation of L-band and C-band interferometry over vegetated areas in California. *IEEE Transactions on Geoscience and Remote Sensing*, 48(7):2942–2952.

[Montgomery-Brown et al., 2009] Montgomery-Brown, E. K., Segall, P., and Miklius, A. (2009). Kilauea slow slip events: Identification, source inversions, and relation to seismicity. *Journal of Geophysical Research: Solid Earth*, 114(B6).

[Odendaal et al., 1994] Odendaal, J., Barnard, E., and Pistorius, C. (1994). Two-dimensional superresolution radar imaging using the MUSIC algorithm. *Antennas and Propagation, IEEE Transactions on*, 42(10):1386–1391.

[Owen et al., 2000] Owen, S., Segall, P., Lisowski, M., Miklius, A., Denlinger, R., and Sako, M. (2000). Rapid deformation of Kilauea Volcano: Global positioning system measurements between 1990 and 1996. *Journal of Geophysical Research*, 105(B8):18983–18998.

[Perissin and Wang, 2012] Perissin, D. and Wang, T. (2012). Repeat-pass SAR interferometry with partially coherent targets. *Geoscience and Remote Sensing, IEEE Transactions on*, 50(1):271–280.

[Prati et al., 2010] Prati, C., Ferretti, A., and Perissin, D. (2010). Recent advances on surface ground deformation measurement by means of repeated space-borne SAR observations. *Journal of Geodynamics*, 49(3):161–170.

[Reeves et al., 2011] Reeves, J. A., Knight, R., Zebker, H. A., Schreder, W. A., Shanker Agram, P., and Lauknes, T. R. (2011). High quality InSAR data linked to seasonal change in hydraulic head for an agricultural area in the San Luis Valley, Colorado. *Water Resources Research*, 47(12).

[Rodriguez and Martin, 1992] Rodriguez, E. and Martin, J. (1992). Theory and design of interferometric synthetic aperture radars. *IEE Proceedings of Radar and Signal Processing*, 139(2):147–159.

[Rosen et al., 2000] Rosen, P., Hensley, S., Joughin, I., Li, F., Madsen, S., Rodriguez, E., and Goldstein, R. (2000). Synthetic aperture radar interferometry. *Proceedings of the IEEE*, 88(3):333–382.

[Scharroo and Visser, 1998] Scharroo, R. and Visser, P. (1998). Precise orbit determination and gravity field improvement for the ERS satellites. *Journal of Geophysical Research: Oceans*, 103(C4):8113–8127.

[Shanker and Zebker, 2007] Shanker, P. and Zebker, H. (2007). Persistent scatterer selection using maximum likelihood estimation. *Geophysical Research Letters*, 34(22):L22301.

[Shimada, 2000] Shimada, M. (2000). Correction of the satellite's state vector and the atmospheric excess path delay in SAR interferometry-application to surface deformation detection. In *Geoscience and Remote Sensing Symposium, 2000. Proceedings. IGARSS 2000. IEEE 2000 International*, volume 5, pages 2236–2238. IEEE.

[Smith and Goggans, 1993] Smith, C. and Goggans, P. (1993). Radar target identification. *Antennas and Propagation Magazine, IEEE*, 35(2):27–38.

[Sousa et al., 2009] Sousa, J. J., Hooper, A., Hanssen, R. F., and Bastos, L. (2009). Comparative study of two different PS-InSAR approaches: DePSI vs. StaMPS. In *Proceedings of FRINGE 2009 Workshop, Frascati*.

[Tarayre and Massonnet, 1996] Tarayre, H. and Massonnet, D. (1996). Atmospheric propagation heterogeneities revealed by ERS-1 interferometry. *Geophysical Research Letters*, 23(9):989–992.

[Tarchi et al., 2003] Tarchi, D., Casagli, N., Fanti, R., Leva, D. D., Luzi, G., Pasuto, A., Pieraccini, M., and Silvano, S. (2003). Landslide monitoring by using ground-based SAR interferometry: an example of application to the Tessina landslide in Italy. *Engineering Geology*, 68(1):15–30.

[Vilardo et al., 2009] Vilardo, G., Ventura, G., Terranova, C., Matano, F., and Nardò, S. (2009). Ground deformation due to tectonic, hydrothermal, gravity, hydrogeological, and anthropic processes in the Campania Region (southern Italy) from permanent scatterers synthetic aperture radar interferometry. *Remote Sensing of Environment*, 113(1):197–212.

[Wang et al., 2008] Wang, T., Perissin, D., Liao, M., and Rocca, F. (2008). Deformation monitoring by long term D-InSAR analysis in Three Gorges Area, China. In *IGARSS 2008 - 2008 IEEE International Geoscience and Remote Sensing Symposium*, volume 4, pages IV – 5–IV – 8.

[Werner et al., 2003] Werner, C., Wegmüller, U., Strozzi, T., and Wiesmann, A. (2003). Interferometric point target analysis for deformation mapping. In *Geoscience and Remote Sensing Symposium, 2003. IGARSS'03. Proceedings. 2003 IEEE International*, volume 7, pages 4362–4364. IEEE.

[Yun et al., 2006] Yun, S., Segall, P., and Zebker, H. (2006). Constraints on magma chamber geometry at Sierra Negra Volcano, Galápagos Islands, based on InSAR observations. *Journal of Volcanology and Geothermal Research*, 150(1):232–243.

[Zebker, 2000] Zebker, H. (2000). Studying the Earth with interferometric radar. *Computing in Science & Engineering*, 2(3):52–60.

[Zebker and Rosen, 1994] Zebker, H. and Rosen, P. (1994). On the derivation of coseismic displacement fields using differential radar interferometry: The Landers earthquake. In *International Geoscience and Remote Sensing Symposium. Surface and Atmospheric Remote Sensing: Technologies, Data Analysis and Interpretation*, volume 1, pages 286–288. IEEE.

[Zebker and Villasenor, 1992] Zebker, H. and Villasenor, J. (1992). Decorrelation in interferometric radar echoes. *IEEE Transactions on Geoscience and Remote Sensing*, 30(5):950–959.

[Zebker and Goldstein, 1986] Zebker, H. A. and Goldstein, R. M. (1986). Topographic mapping from interferometric synthetic aperture radar observations. *Journal of Geophysical Research: Solid Earth*, 91(B5):4993–4999.

[Zebker and Lu, 1998] Zebker, H. A. and Lu, Y. (1998). Phase unwrapping algorithms for radar interferometry: residue-cut, least-squares, and synthesis algorithms. *J. Opt. Soc. Am. A*, 15(3):586–598.